Drag reduction of bluff bodies in tandem

Size and spacing effects on cylinders and cyclists

Reiny Brown

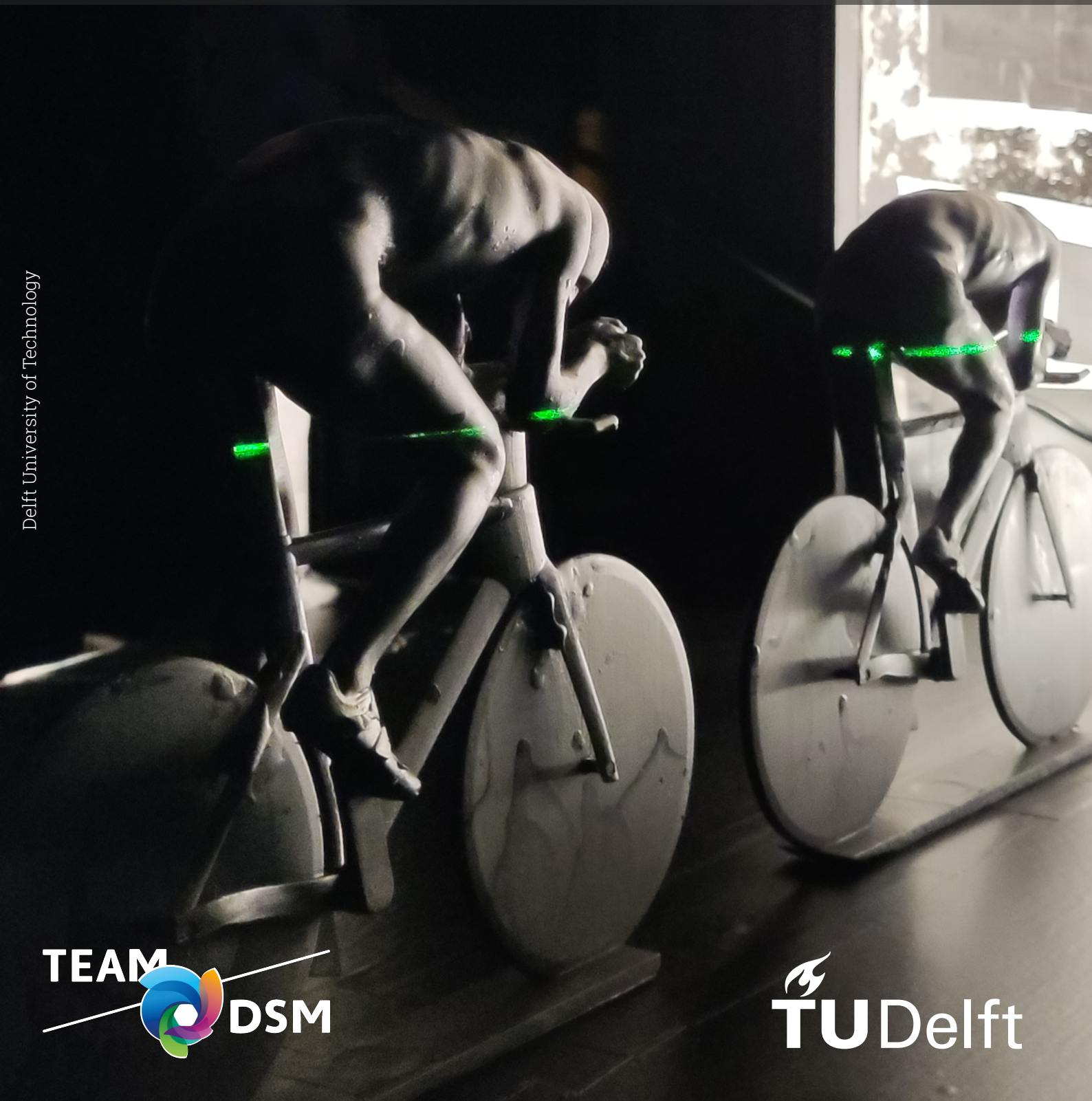

Delft University of Technology

TEAM DSM

TU Delft

Drag reduction of bluff bodies in tandem

Size and spacing effects on cylinders and cyclists

by

Reiny Brown

to obtain the degree of Master of Science,
at the Delft University of Technology,
to be defended publicly on Friday the 21st July 2023, at 09:30

Student number:	4674049	
Project duration:	September 2022 - July 2023	
Thesis committee:		
Dr.ir. B.W. van Oudheusden	Chair	TU Delft - Aerodynamics
Dr. A. Sciacchitano	Supervisor	TU Delft - Aerodynamics
Dr. D. Ragni	Examiner	TU Delft - Wind Energy
Dr. W. Terra	Supervisor	NOC*NSF - Embdedded Scientist Aerodynamics
H. Ubbens	Supervisor	Team DSM - Aerodynamic and innovation expert

TU Delft

Preface

I have never been a fan of a long preface, so I will try my best to keep this short and sweet...unlike what my thesis has turned into. Certainly after 10 months of devoting my efforts towards this single goal, it is a relief and sense of achievement to finally have something, in my mind, meaningful to present and helpful to the world of cycling. And on the flip side, if all things go under, and I am proven wrong with all my results being disputed, at least my one attainment I can attest to is completing the TU Delft Aerospace Engineering Master's degree within the advertised two year period.

The help from my supervisors, Dr. Sciacchitano, Dr. Terra and Ir. Ubbens, has not gone unnoticed, despite your opinions and advice not always aligning. But then again, whenever can you get three people to always agree on everything any time? Nonetheless, your aerodynamic guidance, PIV expertise and professional cycling knowledge has truly been helpful towards the completion of this project and the results collected would have been nowhere near as accurate or valuable without it.

To the friends I have made along the way as well, in particular the members of the exclusive club, Room 2.42, it has been a true pleasure working, and mostly drinking unhealthy amounts of coffee, alongside you. I wish you all the best with the remainder of your thesis and in the future daunting world of adulthood. And to the gang of IHB 2 (and others), thank you very much for making this experience of mine in Delft one worth remembering and treasuring.

In fear of disownment, I must not forget to express my gratitude to my parents in having supported me every step of the way. This achievement would unquestionably not have been possible without your contributions and encouragements.

And finally, to Anneloes, your unwavering support throughout this journey has not only made myself a better engineer, but also a better person in general, and I cannot thank you enough for being there by my side through thick and thin.

Reiny Brown
Delft, July 2023

Abstract

In professional cycling, the aerodynamics around a cyclist has continued to be the key area of research and innovation, all with the aim of obtaining a competitive advantage in competitions. Due to more than 70% of the resistive forces on a cyclist originating from aerodynamic drag at speeds above $40km/h$, it quickly becomes apparent that marginal 1-2% reductions in drag forces can reap considerable time savings and speed increases. This is particularly the case in team time trial competitions or sprint finishes where mere seconds or millimetres split positions between different competitors. In cycling, the presence of drafting, when multiple cyclists ride in tandem, can cause up to 53% drag reductions to be experienced, and is a considerable area of performance enhancement for a cycling team. Professional cycling team rosters typically include cyclists of various size and stature that must ride tandem together in unison, and customisation of this tandem group has the potential of maximising the drag reduction for the entire group or a specific cyclist.

The flow interactions between two tandem bluff body objects is complex and incorporates several fluctuating variations in flow phenomena which have considerable effect on the drag forces experienced. In order to observe these flow interactions effects, an experimental campaign for tandem objects is undertaken, including both a quantitative drag force analysis and a qualitative flow visualisation analysis using a quasi-3D multi planar Particle Image Velocimetry (PIV) technique. Due to the complex nature of the tandem flow interactions, the aerodynamic features around both two tandem finite cylinders and two drafting scaled model cyclist is tested, with the aim of obtaining an improved understanding of the complex flow interactions around tandem bluff bodies and relate that to drafting cyclists. The effect that the spacing and size ratio has on the drag reduction and flow interaction is additionally investigated, whereby tandem objects of varying sizes are placed in tandem with various distances between them.

It is observed that that for both cylinder and cyclist models, a drag reduction of differing magnitude is observed for both the upstream and downstream models, which is however, caused by similar variations in flow structures. The size ratio and spacing ratio are found to affect the tandem object's drag forces in equivalent manners and interact significantly for cylinder cases due to flow regime switches occurring.

Notably for the downstream cylinder and cyclist, an alteration to both the upstream and downstream flow conditions is measured, both of which result in considerable variations in drag reductions. Furthermore, the size ratio and spacing is found to have a significant effect on the sheltering effect and other flow interactions, however affects the cylinder and cyclist models in differing manners. From these results, recommendations for the composition of drafting cyclists in competitions are made, and an empirically based equation for estimating the drag reduction of a drafting cyclist is generated.

Contents

List of Tables

List of Figures

List of Symbols

Latin Letters

Symbol	Unit	Property
A	$[m^2]$	Frontal Area
AR	$[-]$	Aspect ratio
B_t	$[-]$	Model Blockage Ratio
C_d	$[-]$	Drag coefficient
$C_{d,c}$	$[-]$	Corrected drag coefficient
$C_{d,up}$	$[-]$	Upstream drag coefficient
$C_{d,down}$	$[-]$	Downstream drag coefficient
C_p	$[-]$	Pressure coefficient
$C_{p,b}$	$[-]$	Base Pressure coefficient
d	$[mm]$	Upstream cylinder diameter
D	$[mm]$	Downstream cylinder diameter
d/D	$[mm]$	Model size ratio
d_{diff}	$[m]$	Diffraction limit spot
d_i	$[m]$	Distance lens to imagery
d_o	$[m]$	Distance lens to object
DR	$[\%]$	Drag reduction
d_τ	$[m]$	Particle diameter on imagery
d_v	$[m]$	Particle diameter
f	$[m]$	Focal length
F_D	$[N]$	Drag force
$f_\#$	$[-]$	Camera F-stop
G	$[-]$	Glauert empirical factor
H	$[mm]$	Baseline model height
L	$[mm]$	Model Spacing
L/D	$[-]$	Cylinder model spacing ratio
L/W	$[-]$	Cyclist model spacing ratio
M	$[-]$	Magnification distance
n	$[-]$	Number of samples
n_{pixels}	$[-]$	Number of pixels
p	$[N/m^2]$	Pressure
SE	$[-]$	Standard error
T	$[s]$	Time

Symbol	Unit	Property
t	$[mm]$	Zigzap strip thickness
U_∞	$[m/s]$	Streamwise freestream velocity
$\bar{U}$	$[m/s]$	Streamwise mean velocity
u	$[m/s]$	x-component velocity
v	$[m/s]$	y-component velocity
w	$[m/s]$	z-component velocity
w	$[mm]$	Upstream cyclist shoulder width
W	$[mm]$	Downstream cyclist shoulder width
w/W	$[mm]$	Cyclist model size ratio
$[X, Y, Z]$	$[-]$	System coordinate system

Greek Letters

Symbol	Unit	Property
Δt	$[s]$	Time difference
δt	$[mm]$	Boundary layer thickness
δt	$[s]$	Image pair separation time
Δx	$[m]$	Spatial difference
Δu	$[m]$	Velocity difference
λ	$[m]$	Wavelength of light
ρ	$[kg/m^3]$	Density
σ	$[-]$	Standard deviation
θ	$[^\circ]$	Cylinder angular position
θ_R	$[^\circ]$	Re-attachment angle
θ_p	$[^\circ]$	Cyclist pedal stroke angle

1

Introduction

In the high performance industry of professional cycling, aerodynamics plays a key role in determining the outcome from each event. With speeds of up to 60 km/h being reached at certain stages, such as a team time trial or sprint train finale, drag forces are the overwhelmingly predominant resistance phenomena on a cyclist. Optimisation of a cyclist's aerodynamics is therefore a large area of research in sports engineering. Considering the 2016 Cycling World Championships Team Trial event in Doha, over a 40 km course, a mere 12 seconds separated the top two teams, equivalent to a velocity difference of $0.27km/h$. This example highlights the relevancy of this study, where due to the extremely tight performance differences in professional cycling, even small performance optimisations can result in substantial competition improvements. In a team time trial, the aerodynamics of a single rider is not as consequential as that for the entire group, whereby the group's overall mean drag forces are to be minimised. Meanwhile, in a sprint train, the drag reduction for a specific main rider is of importance. Typically, a professional cycling team will have a large range of body geometry between their riders, especially large ranges in relative size and the order in which they are placed is highly customisable. This allows for the drag reduction of the entire group or individual cyclist in a group to be maximised resulting in performance improvements in the arena of competition. However, with the presence of complex flow/wake interference for drafting cyclists and the shape of one cyclist not being directly similar to that of another, comparison between different experimental studies and relating this to size interaction effects is difficult. In order to address these issues, a fundamental understanding of the size and spacing interaction effects between bluff body drafting objects and their impact on individual and overall group drag is required. Therefore, the case study of tandem truncated cylinders in crossflow is additionally covered in this study with the aim of relating to drafting cycling conditions.

The structure of this report begins with a detailed description of the surrounding theory and literature. This includes, Chapter 2 explaining the simple cross flow case of cylinders in tandem, where key flow phenomena and regimes that exist will be covered. From this, a detailed understanding of the aerodynamics of drafting objects is derived. This leads to Chapter 3, which covers the topic of drafting cyclists. Having covered the basic flow physics from the previous chapter, its relation to cyclists will

be discussed. At the end of Chapter 2 and Chapter 3, a gap in the literature will be evident and the importance of researching this area shall be clear. In Chapter 4, research questions that undermine the pathway and end goal for this thesis shall be outlined. In Chapter 5, the methodology to address this gap will be covered, with the aim of answering the research questions. This will largely include experimental testing and cover the various methods that could be deployed to investigate aerodynamic drag of drafting cyclists. In Chapter 6, post-processing techniques and limitations of this experimental method shall be discussed. In Chapter 7 and 8 the results from the tandem finite cylinders and drafting cyclists shall be outlined and analysed in detail respectively. Lastly, in Chapter 9, conclusions from the results shall be drawn, answering the research questions and also future research and work to further address the aims of this thesis are outlined.

Figure 1.1: Team time trial configuration of drafting cyclists (Vereecken 2023)

Figure 1.2: Cyclists drafting in a sprint train lead out format (Cramp 2010)

2

Cylinders in tandem

In this chapter, the aerodynamic theory for flow around both infinite and finite cylinders is covered and the differences are investigated. Furthermore, previous literature investigating the variation in aerodynamic flow that occurs for tandem cylinder configurations of various size ratios and spacings is discussed.

A cylinder in crossflow is one of the most widely researched case study in the domain of aerodynamics. This is because the simplified flow physics around a cylinder is heavily connected with other bluff bodies and can be related to more complex geometries (Zhou and Alam 2016). This, in turn helps predict and explain the flow phenomena for these situations. The same applies to two cylinders in crossflow, which is one of the most fundamental aerodynamics example of two objects aligned in tandem. Since the 1970's, a considerable amount of research has been undertaken focusing on this case study. In particular, with the use of novel numerical methods, namely Computational Fluid Dynamics (CFD), the beginning of the millennium saw a surge in research in the field, while experimental research methods, including force data and flow visualisation, have remained high for the last 50 years (Zhou and Alam 2016).

2.1. Flow structures and regimes

Despite being the simplest configuration, the wake interaction that exists between two tandem cylinders quickly creates a complex fluid dynamics situation. This includes boundary layer separation, vortex shedding and interaction, shear layer development and re-attachment and flow regime switches. Studying the flow around two cylinders provides an excellent baseline to understand the fundamental physics and coherent structures that exist. In modern practical engineering circumstances, the noise, resonance and structural vibrations caused by the bistable vortex shedding and the large force fluctuations is of large importance, as it heavily relates to the causes of structural failure. It is for this reason that the majority of research into tandem cylinders focuses on the force frequencies exerted on the cylinders and the strength of these fluctuations and not on time-averaged forces, such as drag. Regardless, a plethora of configurations of full-span cylinders have been tested, at various position combinations, Reynolds

numbers and flow conditions, creating a large database to source through.

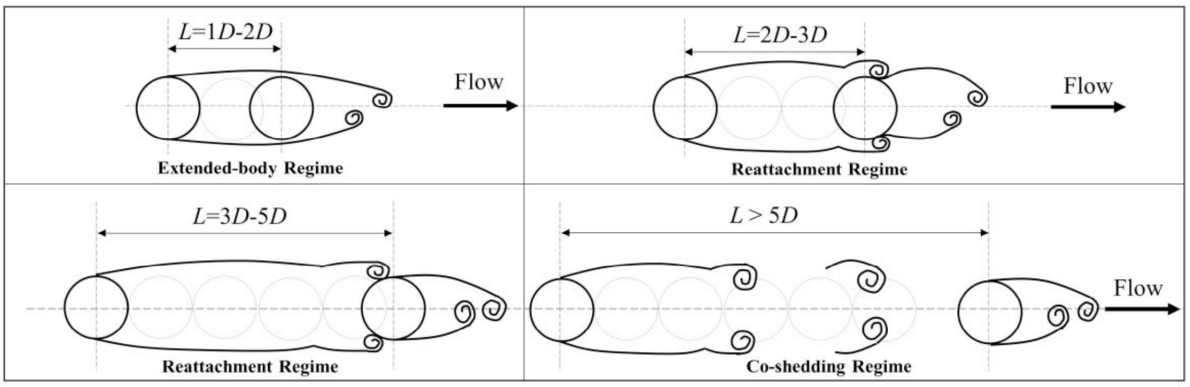

Figure 2.1: Simple schematic of the various flow regimes for two equally sized cylinders in tandem (Shao et al. 2020)

For cylinders in tandem, there are three main flow regimes that significantly change the flow structures and aerodynamic forces on the cylinders, as described by Zhou and Yiu 2006. When the spacing between the two cylinders is small, they act as if they are a single elongated obstruction in the flow, with stagnant flow in the gap between them and hence, is called the *Extended-body regime*. In this regime, the upstream cylinder's shear layers roll up rearwards of the trailing cylinder, never re-attaching. Therefore, the vortex street is primarily created by the upstream cylinder as observed by Igarashi 1981. It is further noted that in the extended body regime, the drag coefficient of the upstream cylinder $C_{d,up}$ is slightly lower compared to a single cylinder case, while the drag coefficient of the downstream cylinder $C_{d,down}$, is near zero or even negative, resulting in a thrust force being exerted.

With an increasing spacing, the flow regime changes to the *Re-attachment regime*, where the shear layers shed from the upstream cylinder may now re-attach onto the downstream cylinder, in several different manners. A schematic diagram of the various instantaneous flow structures that may exist in this regime are shown in Figure 2.2, while the time averaged flow structures are shown in Figure 2.1. With alternate re-attachment, the re-attachment of the shear layer alternately attaches on the front face of the trailing cylinder and is in phase with its vortex shedding (Pattern B in Figure 2.2). For slightly larger spacings, near continuous re-attachment of the shear layer results in quasi-stationary eddies developing in the gap and is called *quasi-steady re-attachment* (Pattern C in Figure 2.2). Increasing the spacing further, intermittent re-attachment flow occurs, where the gap vortices are discontinuously shed as the shear layers experience more oscillatory characteristics (Pattern D in Figure 2.2). Shao et al. 2020 found that the re-attachment point of the shear layer begins at the trailing edge of the downstream cylinder, before moving upstream towards the leading edge with increasing spacing ratio. At a critical spacing, L^*, the re-attachment point at the leading edge will disappear and two vortex sheets will be shed from both cylinders. This is called the *Co-shedding regime*, and both cylinders will have continuous vortex shedding (Pattern E and F in Figure 2.2).

2.2. Reynolds number sensitivity

It must be noted, however, that the formation of the flow structures and re-attachment of these shear layers at specific spacings are very sensitive to Reynolds number and certain flow characteristics may occur or disappear with certain Reynolds numbers. Considering this, the spacings given for each flow

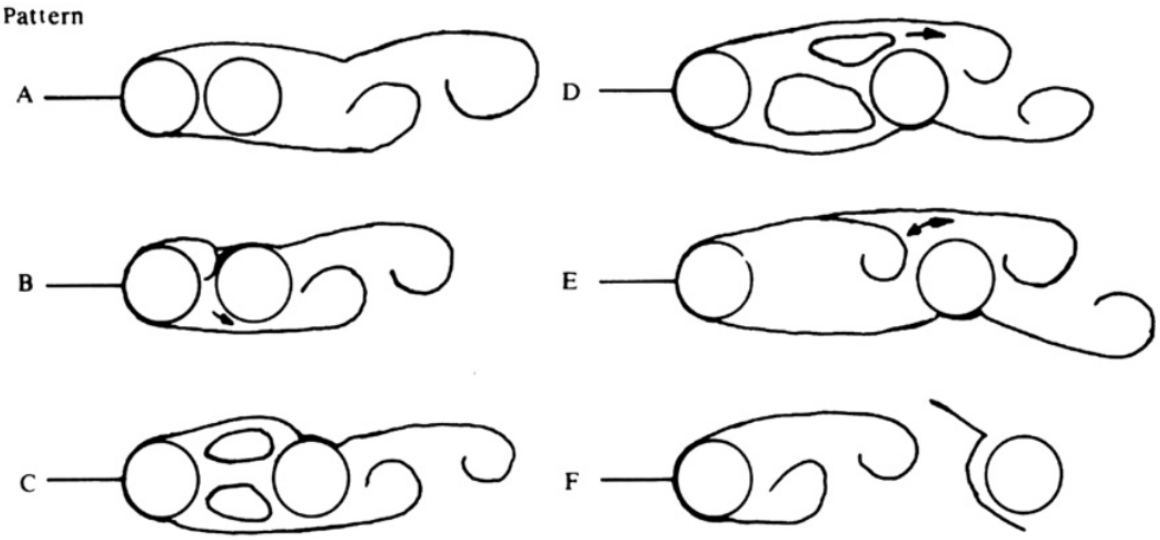

Figure 2.2: Additional schematic of the various flow regimes for two equally sized cylinders in tandem, including several configurations in the re-attachment regime(Ljungkrona et al. 1991)

regime in Figure 2.1 are only rough estimates ranges for infinite cylinders tested at reasonable Reynolds numbers ($10^3 < Re < 10^4$). The critical spacing ratio, $L*$, is found to be very sensitive to the Reynolds number, with Igarashi 1981 noting a pattern of a reduction in $L*$ occurring with an increase in Reynolds number. Additionally, Wang et al. 2018 notes a phenomena of the upstream cylinder's shear layer re-attaching downstream on the alternate side of the downstream cylinder. This creates multiple $C_{d,down}$ peaks which only occur above a certain Reynolds number.

To understand Reynolds number effects on tandem cylinder configurations, one must first familiarise themselves with the variation in flow structure and drag coefficient for an isolated cylinder. Wind tunnel testing by Schewe 2001 investigated the Reynolds sensitivity of cylinders and describes three main Reynolds number regimes that exist, which are visualised in Figure 2.3. In the sub-critical regime, laminar separation occurs and transition takes place off body in the wake, creating a large wake behind the cylinder. In the super-critical regime, separation bubbles occur with transition close to the body. This bubble converts the boundary layer to turbulent, and the flow can follow the surface and remain attached, in turn reducing the wake size. In the trans-critical regime, transition takes place before separation and the thickest point of the cylinder ($\theta = 90°$) is the separation point. This increases the width of the wake again to an intermediate size between the sub critical and supercritical regime.

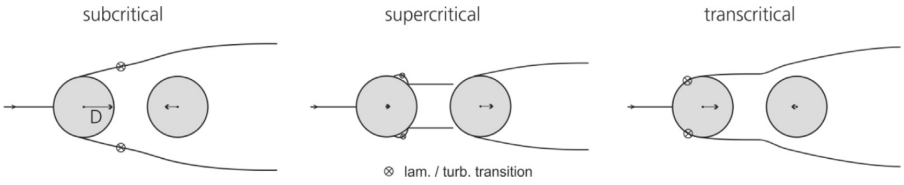

Figure 2.3: Schematic diagram of the flow structures sensitivity to Reynolds number regimes) (Schewe and Jacobs 2019)

Applying this flow physics to tandem cylinder configurations, it is obvious to note that at lower sub critical Reynolds numbers, the large wake will result in the drag coefficient of the downstream cylinder, $C_{d,down}$, to be very small (or negative), as observed by Schewe and Jacobs 2019, with a minimum

$C_{d,down} = -0.4$ measured (for $L/D = 1.56$). This large wake will, however, cause the upstream cylinder's drag coefficient, $C_{d,up}$, to be large. At a critical Reynolds number, the regime changes to the supercritical regime, where a large jump to $C_{d,down} = 0.4$ is observed due to the upstream shear layers being shed nearer to the downstream cylinder's stagnation point. Simultaneously, $C_{d,up}$, were measured to also decrease, partly due to the smaller wake size and partly due to the larger high pressure region occurring on the trailing cylinder's leading edge. Increasing the Reynolds number further to the trans-critical regime, $C_{d,down}$ is found to decrease again and $C_{d,up}$ increases.

2.3. Finite length cylinders

As has been discussed, the steady crossflow configuration of two tandem infinite cylinders has been comprehensively researched and the two dimensional flow effects allows for a fundamental understanding of the basic flow structures. However, to make this case study more relatable to cycling purposes, the usage of finite (or truncated) cylinders and an understanding of their flow physics is essential. Despite still being a simplistic representation of a cyclist model, a finite cylinder incorporates several of the dominant flow structures that exist on a cyclist and aids in the understanding of size and spacing interaction effects on drag forces.

The largest divergence from the infinite cylinder case is the existence of supplementary vortex structures, namely streamwise shed vortex pairs formed at the free end tip and ground plane base and the presence of down wash in the wake. These can be viewed in Figure 2.4, where the left and right tip vortices are paired with the left and right counter-rotating components of the horseshoe vortex. These vortex structures will extend the wake formation length, which in turn will decrease the drag coefficient of a finite cylinder relative to its infinite counterpart, as observed by Sumner and Reitenbach 2019.

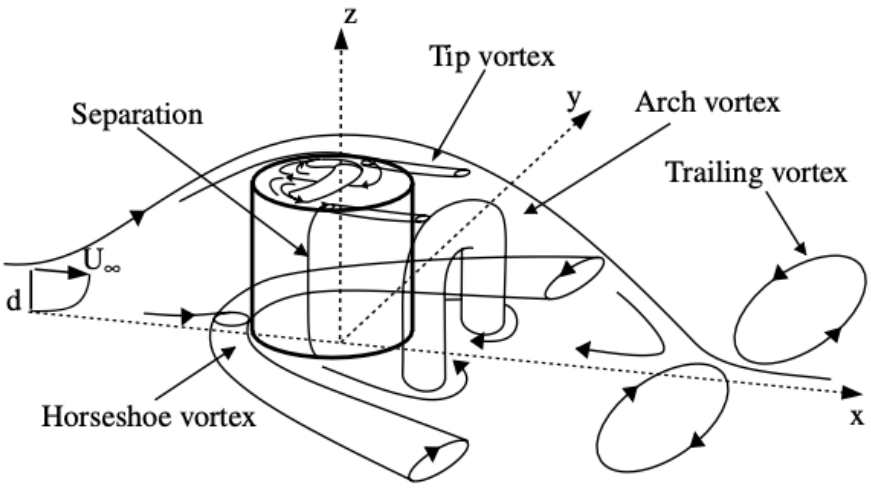

Figure 2.4: Schematic diagram of the dominant time averaged flow structures over an individual truncated cylinder (Pattenden et al. 2005)

The main flow regimes that have been discussed in Section 2.1, namely the *extended body regime*, *re-attachment regime* and *co-shedding regime* are still able to be observed for tandem finite cylinders, even at aspect ratios as low as $AR = 1.33$ and $AR = 2.37$ (both tested at $Re = 2 - 3 \times 10^3$) by Kim and Christensen 2018. The wake interaction effects between two tandem cylinders is heavily influenced by

the wake formation length of the leading cylinder and determines which flow regime is present. For a finite cylinder, this formation length is non-uniform along the cylinder span and is typically longer than that observed with infinite cylinders (Igbalajobi et al. 2013). It is possible in fact, that cylinders with large enough aspect ratios have two flow regimes co-exist along the span. Research by Luo et al. 1996 found that for cylinders of $AR = 4$, a re-attachment regime existed on the lower half of the cylinder span, which implies a large wake formation length, while a co-shedding regime existed on the upper spanwise region, suggesting a short formation length.

Experimental testing by Sumner and Reitenbach 2019 concluded that the ability of the upstream cylinder to shield the downstream one is weaker for finite length cylinders compared with infinite cylinders. This can clearly be observed from the graph in Figure 2.5, where for all spacing ratios the downstream finite cylinder has a larger drag coefficient than the infinite one. This is despite in individual cases the finite cylinder typically has a lower C_d. This is evident with the upstream finite cylinder, which has a smaller drag coefficient than its infinite counterpart for all spacing configurations. Sumner and Reitenbach 2019 hypothesises that the increase in drag coefficient is due to the flow downwash impinging itself onto the trailing cylinder. Additionally, it may be observed that there is no critical spacing for both truncated cylinders, which typically signals a change in flow regime from re-attachment to co-shedding. Sumner and Reitenbach 2019 provides several possible explanations for this phenomena. This includes the critical spacing being delayed for finite cylinders and is beyond the tested spacing range. Another more feasible possibility, is that the jump discontinuity in drag coefficient is smoothed out by the 3D flow effects (e.g. downwash and trailing vortex structures) and the non-uniform wake formation length along the cylinder span. Lastly, shear layer re-attachment at the trailing cylinder free-end and ground plane base may not occur, resulting in a weak co-shedding regime existing at these areas, while shear layer attachment occurs at the mid-height. However, it must be noted that Sumner and Reitenbach 2019 stresses that none of these conclusions are certainties and rely upon further flow visualisation research.

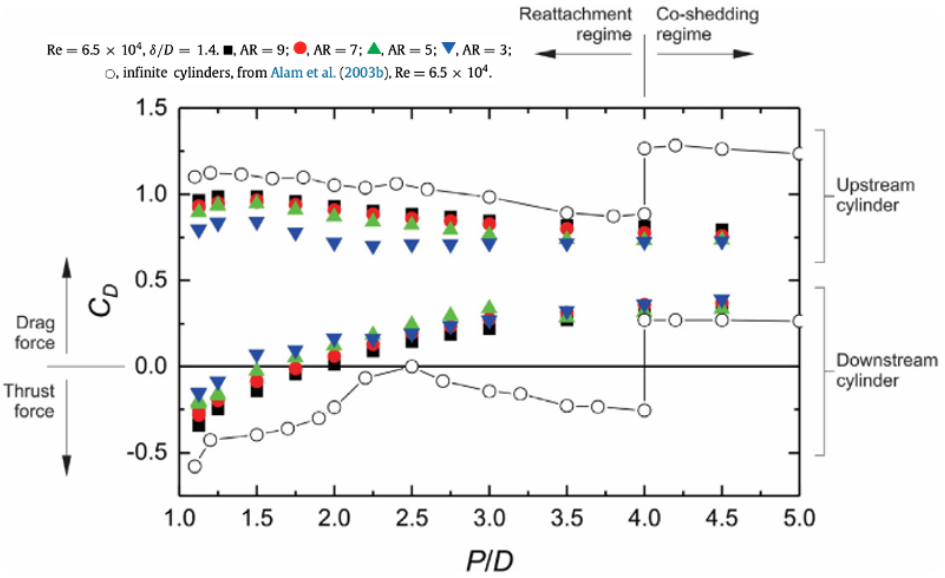

Figure 2.5: Mean drag coefficient for two tandem finite cylinders at differing spacing ratios (or pitch ratio P/D) from Sumner and Reitenbach 2019. The critical spacing at $P/D = 4$ was observed by Alam et al. 2003a for infinite cylinders

2.4. Longitudinal spacing effects

As observed in Figure 2.5, not only for infinite cylinders but also for truncated cylinders, increasing the longitudinal spacing ratio, L/D, generally results in an increase in drag coefficient for both the upstream and downstream cylinders. This can generally be explained by an increase in spacing allowing for a larger region for the wake to mix with the freestream, re-energising the low velocity region. This will increase the incoming velocity for the trailing cylinder, increasing the stagnation area's C_p and the cylinder's overall drag coefficient. Additionally, for a constant Reynolds number, an increase in spacing ratio can also result in a change in flow regime from extended body to re-attachment to co-shedding. At very small spacings, typically below $L/D = 2$, for infinite cylinders, the entire region between the two cylinders is stagnate, with very low pressure (Shao et al. 2020). This results in a thrust force for the trailing cylinder, however for the upstream cylinder, it's base pressure coefficient is so low that the drag coefficient is only slightly smaller than that of an individual cylinder, as found by Zdravkovich 1977. Increasing the spacing to the re-attachment regime, more pressure recovery behind leading cylinder occurs, decreasing the drag coefficient $C_{d,up}$ by up to 20% (Sumner 2010). It must be noted, that at a certain spacing, the $C_{d,up}$ of the upstream cylinder increases again, as the high pressure stagnation point of the trailing cylinder no longer strongly interacts with the upstream cylinder's wake.

The trailing cylinder's drag coefficient typically increases predictably with increasing spacing without any presence of "drag kinks", especially for truncated cylinders, as shown in Figure 2.5. This is most likely due to the 3D flow characteristics of finite cylinders dampening out flow phenomena that occur on infinite cylinders. This includes the shear layer attachment switching to the alternate side which caused multiple $C_{d,down}$ peaks to be observed by Alam et al. 2003a, and is not seen with truncated cylinders. The increase in $C_{d,down}$ with spacing can be explained by the shear layer attachment point (and associated pressure coefficient peak) for the re-attachment regime typically hovering around $30° < \theta < 70°$, with lower re-attachment angles existing at larger spacings (Wang et al. 2018). In the co-shedding regime, the time-averaged point of re-attachment is at the center line. This change in pressure peak location will naturally increase the drag coefficient of the trailing cylinder. It must be re-iterated that for truncated cylinders, it is possible for two distinct flow regimes to co-exist along the span of the cylinder, each with their own respective flow characteristics and aerodynamic forces. Therefore, changes in drag forces are not due to variation in just one flow structure, but several variations along the span.

Particle Image Velocimetry (PIV) testing of truncated cylinders by Kim and Christensen 2018 are shown in Figure 2.6, where it was observed that at small spacings the wake from the upstream cylinder was impeded from reaching the ground plane by the downstream cylinder. This resulted in the downstream cylinder having a weaker and smaller recirculation region behind it, with a weaker and lesser angled down wash from the free-end (compared with an individual finite cylinder case). This effect was explained due a reduction in turbulence levels and vortex strength forming at the top of the down stream cylinder. When the spacing was increased, the upstream cylinder's wake would re-attach to the ground plane, resulting a stronger (and larger) re-circulation region behind the down stream cylinder. Additionally, the size of these vortices formed at the free end was observed to increase, resulting in a stronger and more angled down wash to be present, similar in characteristics to that of an isolated case.

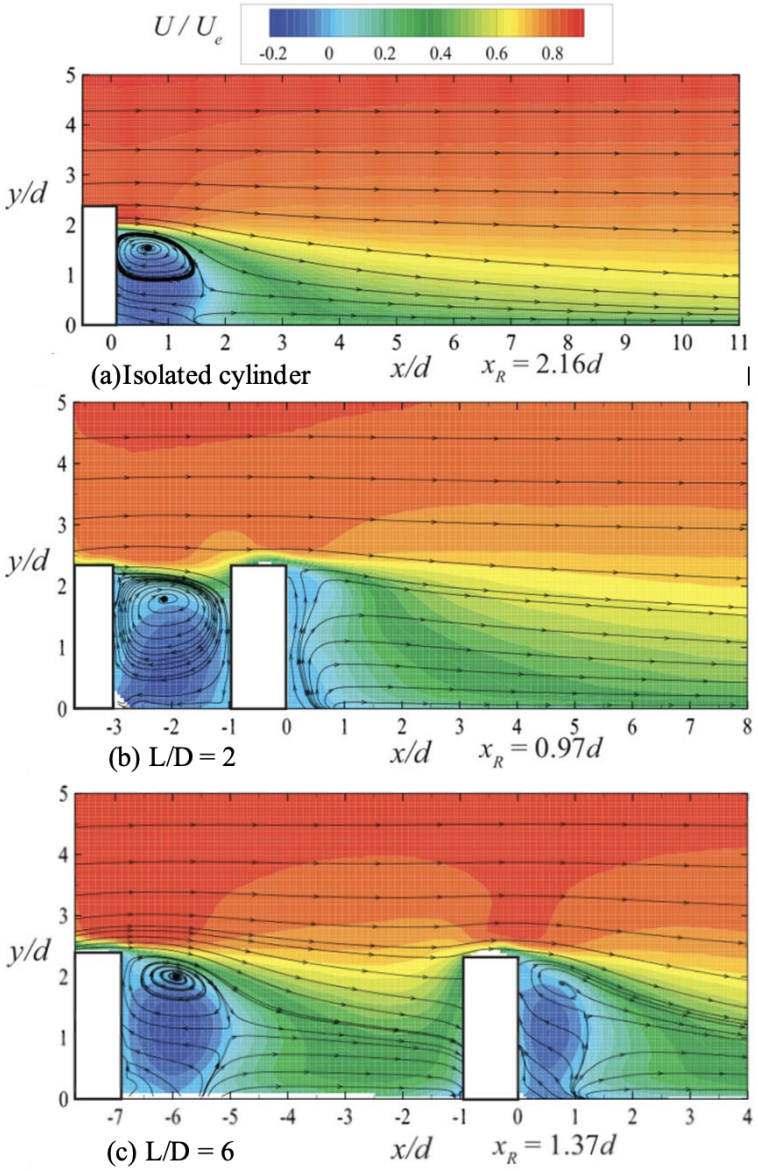

Figure 2.6: Ensemble average streamwise velocity for truncated cylinders in an isolated and tandem configuration. The streamwise ground plane re-attachment point, x_R, is shown for the downstream cylinder under each plot. (Kim and Christensen 2018)

2.5. Diameter ratio effects

As noted by Sumner and Reitenbach 2019, discretion must be undertaken when extrapolating infinite cylinder data to finite cylinder configurations. This is particularly the situation for this case study, where finite cylinders of small aspect ratios are to be used to mimic a cyclist body. However, apart from introductory flow visualisation research by Kim and Christensen 2018, no known previous literature involving aerodynamic testing with finite cylinders of differing diameter ratios in tandem has been performed before. Therefore, extrapolation of research from infinite cylinder studies must be performed.

Larger diameter ratios should in theory result in a lower $C_{d,down}$ for the downstream cylinder, as it experiences an ever greater sheltering effect from the upstream cylinder, due to the low pressure region

in between the two objects. A larger diameter ratio will increase the upstream cylinder's wake relative to the downstream cylinder. The reduction in gap velocity between the two cylinders, weakens the stagnation point C_p at the front of the trailing cylinder, reducing $C_{d,down}$. Several studies have observed this result, including Zhou and Yiu 2006 and Wang et al. 2018. However, another complementing effect is the shear layer re-attachment on the downstream cylinder. When comparing flow cases of $d/D = 0.8$ and $d/D = 1.0$ in the re-attachment regime, despite the equal spacing distances between two cylinders, the re-attachment point for the larger diameter ratio case is further downstream. Zhou and Yiu 2006 reasons that this causes reduced boundary layer development on the trailing cylinder, hence a delayed separation point, smaller wake section and lower measured $C_{d,down}$. This effect can clearly be observed in Figure 2.7, where flow visualisation shows a wider gap between shear layers forming for the larger diameter ratio case, with re-attachment occurring further downstream. This change in re-attachment point has large effects on the drag coefficient for the trailing cylinder. Zhou and Yiu 2006 further notes a more downstream re-attachment point (and hence larger re-attachment angle, θ_R), will increase the base pressure coefficient behind the trailing cylinder causing a reduced wake size. These two effects will drastically reduce the drag coefficient of the downstream cylinder and one can hypothesize that a larger object upstream, resulting in a higher diameter ratio should decrease $C_{d,down}$.

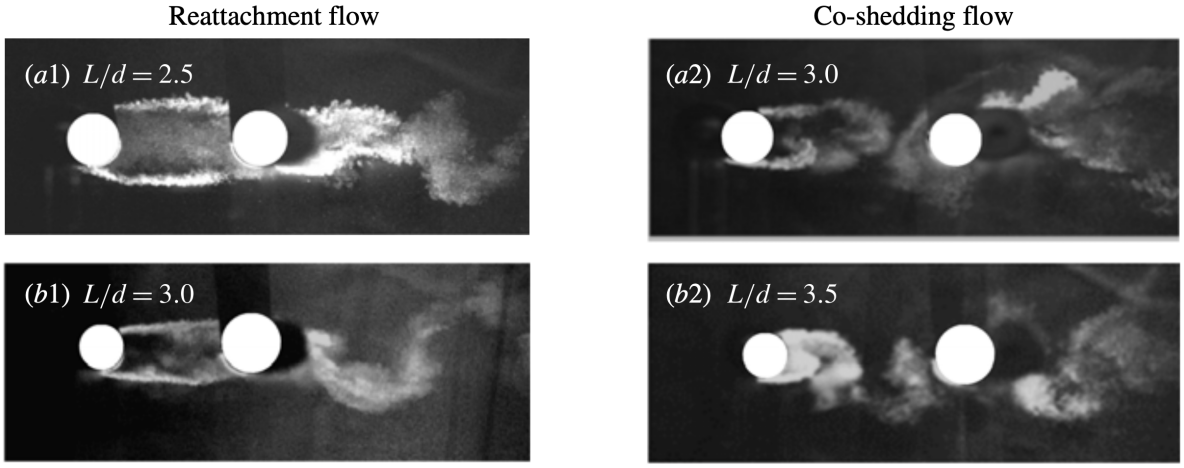

Figure 2.7: Flow visualisation of two tandem infinite cylinders in differing flow regimes with varying diameter and spacing ratio. Figures (*a*) shows a size ratio of d/D = 1, while Figures (*b*) shows a size ratio of d/D = 0.8 (Wang et al. 2018)

However, an increase in diameter ratio is detrimental for the upstream cylinder, which experiences an increase in drag, as observed by Igarashi 1982. This is because the relative size of the trailing cylinder's stagnation area (and associated high pressure region) is smaller for the upstream cylinder, resulting in a smaller upstream interaction effect. The base pressure coefficient for the upstream cylinder does not increase as much when a relatively smaller object is behind it, and since the leading edge pressure coefficient remains largely unaffected, $C_{d,up}$ is found to increase. Therefore, in order to obtain the minimum drag point for the group of cylinders, a balance between the drag reduction for the downstream cylinder and upstream cylinder must be found. It must be reminded that the interaction effects between the two cylinders are heavily dependent on the spacing ratio and Reynolds number and these parameters are required to be considered when finding the minimum drag point.

Pressure distribution studies performed by Wang et al. 2006 and Wang et al. 2018 agreed with earlier observations by Zhou and Yiu 2006, where a large increase in surface pressure coefficient of the trailing cylinder occurs when the shear layer re-attaches. Wang et al. 2006 notes that at the re-attachment point,

this results in a increase in local drag at that specific point compared with a single cylinder case. This can clearly be viewed in the drag reduction distribution plotted in Figure 2.8, with an increase in drag being measured in Section B, where the shear layer re-attaches. For the isolated cylinder case measured, Section B is an area of low pressure due to the surface curvature, with negative pressure coefficients being present on the leading edge from $35° < \theta < 90°$, creating a thrust force on the cylinder. However, when the shear-layer of an upstream cylinder re-attaches in this region, the pressure coefficient was found to increase and even be positive around $\theta = 40°$, hence removing a thrust force and decreasing the leading edge drag reduction. It must be noted, however, that this reduction in front face thrust force is compensated with drag reductions at the stagnation region, Section A and trailing edge region, Section D being observed. It is hypothesised that for a given L/D and Reynolds number, there is an ideal diameter ratio that optimises the combination of these two phenomena, which maximises the drag reduction for the trailing cylinder.

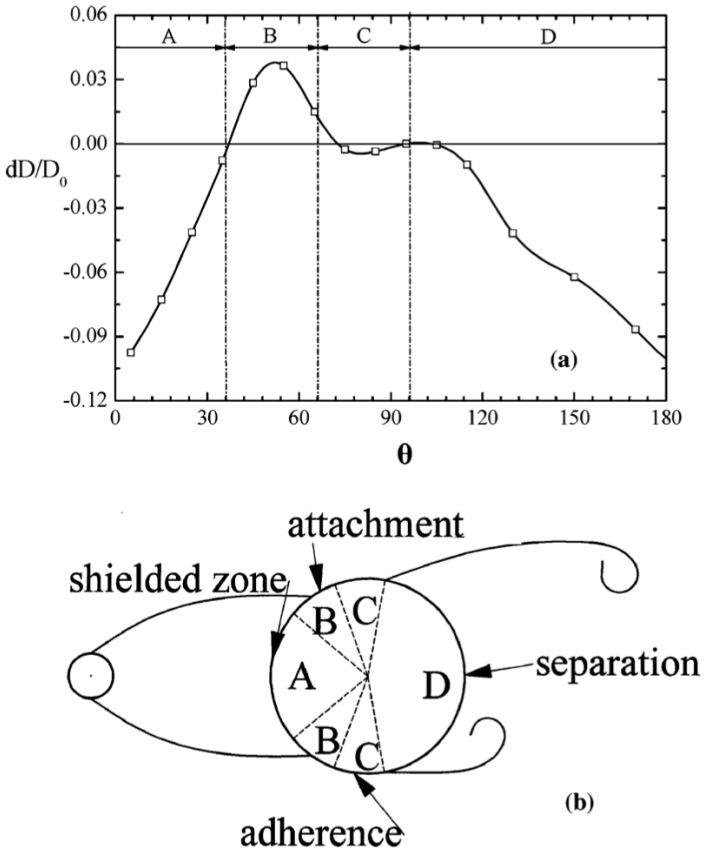

Figure 2.8: A cylinder surface is split into four regions and the drag reduction distribution dD/D_0 is plotted for each region. D_0 is the drag of an isolated cylinder and dD the local drag change due to the local pressure distribution. Hence $dD/D_0 < 1$ indicates local drag reduction. (Wang et al. 2006)

The majority of research into tandem cylinder configuration typically results in the $0 < d/D \leq 1$ range, meaning the smaller cylinder is always the upstream object. Despite limited studies involving diameter ratios above 1 existing, such as Igarashi 1982 testing with a size ratio of $d/D = 1.47$ and Novák 1975 with $d/D = 1.50$, to the author's knowledge, no published experimental testing has investigated the flow patterns or aerodynamic forces for diameter ratios between $1.0 < d/D < 1.47$. Additionally, the interaction effects between cylinder spacings and diameter ratios and their effect on both the individual and overall drag forces for $d/D > 1$ are yet to be understood.

2.6. Flow visualisation techniques

PIV measurement of cylinders in tandem has been used extensively to analyse flow structure interaction and explain variation in aerodynamic forces (Jeon 1996, Alam and Zhou 2007, Alam and Zhou 2008, Wang et al. 2018). For infinite cylinders, the aspect ratio is typically high enough that using West and Apelt 1993 definition of 'long cylinder condition', the flow can be assumed to be independent of the cylinder's spanwise location, therefore implying two dimensional flow. This results in the majority of PIV studies utilising simple 2D PIV in the X-Y plane centred at the spanwise centre, where minimal wall interference effects are present. This plane location will capture the dominant flow structured, namely shear layer re-attachment and wake interaction between the two cylinders, aiding in detailing the spacing and size effects on drag forces.

However, as the flow around truncated cylinders is 3D with the inclusion of trailing vortices, measuring the variation of velocity in the Z-axis is also necessary. It must be noted, that although a meaningful amount of flow visualisation research has been applied to individual finite cylinders (Pattenden et al. 2005, Hain et al. 2008, Schneiders et al. 2016), limited flow visualisation of two finite cylinder in tandem has been performed.

A simplistic, yet effective method of capturing the streamwise cross sectional velocity components (Y-Z plane) is to perform a stepwise change in the Z-height of the X-Y PIV plane and capture velocity data at each height. Through interpolation, Y-Z plane momentum deficit behind each cylinder can be captured without the necessity of stereoscopic or volumetric PIV. A similar method of quasi-3D PIV flow visualisation using multiple 2D planes, capturing 2 velocity component has been successfully implemented by Barry et al. 2016a, where the flow interaction between two drafting cyclists at close spacing was analysed. These more complex forms of PIV have their own complications, especially with experimental configurations of two tandem objects with minimal spacing, as will be discussed below with cyclist models that suffer from similar issues.

3

Cyclists drafting in tandem

In this chapter, a review of literature regarding aerodynamic flow around an individual cyclist and drafting cyclists is covered, including the dominant flow structures that are present and how these have been observed to vary in drafting circumstances. Furthermore, the various possible techniques that can be used to obtain aerodynamic load and flow data is covered.

Drafting in cycling is a key parameter that affects all aspects of the sport and has a large weighting on deciding the victor of any competition. The reasoning behind this was made clear by initial, simple coast-down test research conducted by Kyle 1979, where it was found that at typical attainable race speeds, ranging from $24km/h$ to $56km/h$, aerodynamic drag compromised over 70% of total resistance. With modern day professional cyclists achieving new record high average speeds, due to advancements in technology, body conditioning, nutrition and aerodynamic research, unit improvements in aerodynamic resistance provide ever greater performance enhancements.

Most interestingly, professional cycling teams in certain circumstances have the capability of fully controlling the drafting performance of their entire group of riders. These situations include sprint trains in race finales and team time trials, where in both conditions several riders are positioned in tandem drafting each other. In a team time trial, the overall drag for all cyclists in a group is to be minimised and in a sprint train the drag reduction for one specific cyclist (the sprinter) is maximised. In both situations, the teams are able to determine the positioning order of their cyclists. Typical rhetoric in cycling is that the largest cyclist should be at the front of the group and the size of each cyclist in the group decreases downstream. Despite this approach seeming intuitive with aerodynamic theory, there is minimal experimental evidence and research available to support this method. Additionally, the optimisation of the drag reduction for a group of cyclists is unknown with limited testing having been conducted analysing the aerodynamic drag effect of cyclists of different sizes and positions drafting each other.

3.1. Aerodynamic Testing

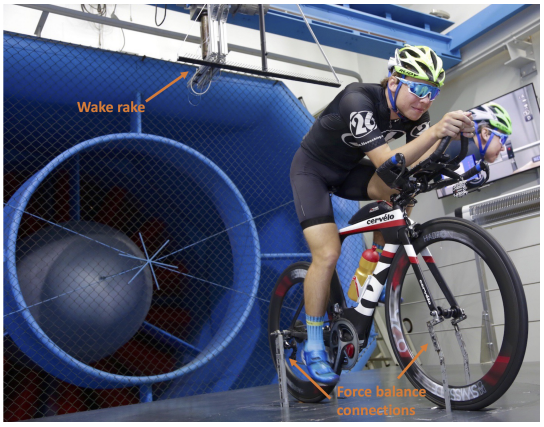

Figure 3.1: Dynamic wind tunnel testing of a pedalling cyclist, using a force balance for drag measurement and pressure probe rake for wake characterisation

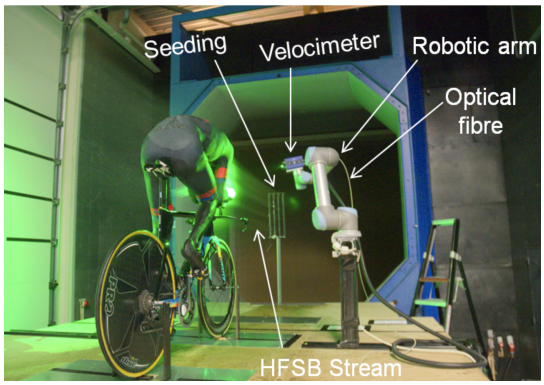

Figure 3.2: Particle Tracking Velocimetry (PTV) flow visualisation and force balance measurement of static full scale cyclist model in a wind tunnel (Jux 2022)

Several studies have been conducted analysing the effect that drafting has on a cyclist, using various types of methods. The first known aerodynamic testing of cyclists drafting was conducted by Kawamura 1953, who looked at wind tunnel measurements for quarter scale cyclist models in a racing position. The use of scaled models is enticing and has been used in numerous experimental studies (Kawamura 1953,Barry et al. 2016a, Blocken et al. 2018), due to its non-necessity for large wind tunnels as well avoiding high blockage ratios. Zdravkovich et al. 1996 performed wind tunnel measurements for several human pedalling cyclists, similar to that seen in Figure 3.1, including various longitudinal and lateral spacings configurations, however in an upright position. Both full scale and model methods found considerable drag reductions for the trailing cyclist. Additionally, up until recently, PIV flow visualisation techniques were not able to provide sufficient spatial resolution at the full scale models, therefore scaled models were used instead. Barry et al. 2016a analysed the flow structures between two 10% sized cycling models and due to the relatively small field of view, adequate capturing of the dominant flow structures was possible. However, most importantly, models allowed for reliable repeatability and consistency as the positioning and frontal area do not vary between tests. Issues that arise with scaled models are that lower Reynolds numbers than full scale situations are experienced and must be acknowledged and accounted for either by flow tripping and/or testing at higher velocities. Recently, novel flow visualisation methods using a robotic arm to achieve volumetric flow visualisation have been performed on full scale cyclist models (Shah 2017 and Jux 2022) using Particle Tracking Velocimetry (PTV), as seen in Figure 3.2 and have been able to capture a large range in flow structure size. This new method not only describes the aerodynamic characteristics sufficiently, but also relates to real world situations more directly. However, issues still occur including large wind tunnels being required and manufacturing of models being expensive and long winded.

Access to wind tunnels is sometimes not possible, and additionally the Eulerian nature of testing is detached from the reality of cyclists moving through a medium of air. This results with the positioning of the cyclist potentially not accurately mimicking a real life position. Therefore, alternative testing methods to address these issues have been derived, including a common method of determining the aerodynamic drag on cyclist using a coast-down procedure in an indoor environment. One such study was conducted by Kyle 1979, where the reduction in wind resistance was analysed with groups of one

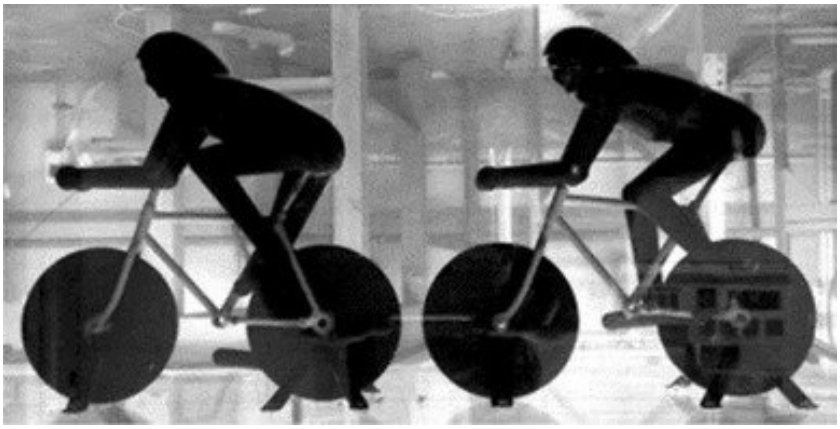

Figure 3.3: 1/10 scaled model used in a water tank for PIV testing (Barry et al. 2016a)

to four cyclists riding in a pace line coasting down in an indoor 200m long hallway. It was found that compared with Kawamura 1953, notably lower drag reductions were measured by Kyle 1979 in the racing position with a 39% reduction being recorded. However, in the upright position, the observed 48% wind resistance reduction agrees highly with the wind tunnel measurement results from Zdravkovich et al. 1996. Another method of determining aerodynamic drag performed by Edwards and Byrnes 2007 is with the conduction of outdoor experiments involving various test cyclists, where the cyclist's power output and bike speed is collected to determine the drag coefficient of the cyclist. Research by Mahalingesh 2020 and Spoelstra et al. 2021 utilised a novel large-scale time resolved stereoscopic PIV method, applied to moving pedalling cyclists, namely the *Ring Of Fire*, to analyse the flow structures and forces around full scale moving cyclists in a real world environment. Figure 3.4 illustrates the experimental method, where cyclists travelled through a tent filled with helium soap bubbles tracer particles, laser illumination and camera set ups. By analysing the velocity fields in front and behind a cyclist and applying conservation of momentum, the drag forces on a cyclist were calculated. All of these studies better mimic real world performance as the test cyclists are able to hold positions and assosciated frontal areas that would occur in competition formats and make results collected more relatable. However, the largest problem with these experimentation methods is the introduction of several new variables that are not able to be controlled, which makes comparison of results between different test runs difficult. These variables include inconsistent spacing (laterally and longitudinally) and the presence of atmospheric wind speed.

Figure 3.4: Drafting line of cyclists riding through the tent measurement zone for the Ring of Fire experimental method (Spoelstra et al. 2021)

Another alternative method for aerodynamic testing that has increased in popularity over the last two decades, is the ability to numerically solve for the fluid domain using CFD. Research by Blocken et al. 2013, Defraeye et al. 2014 and Blocken et al. 2018 have performed CFD studies on numerous cyclists drafting in tandem in various different positions. Similar to model wind tunnel testing, the consistent body shapes remove unknown variables impeding results between test runs. Furthermore, this numerical method has allowed for visualisation of flow structures in areas difficult for PIV methods to capture, due to closely spaced objects blocking optical access. One must note however, that the majority of CFD studies have relied upon RANS methods, which include their own impediments of correctly simulating the flow, with empirical solving variables being tedious to tune sufficiently. Notably, Blocken et al. 2013 mentions that a 10.5% deviation in drag area of an isolated cyclist in an upright position between the wind tunnel experiment and numerical solver method is measured.

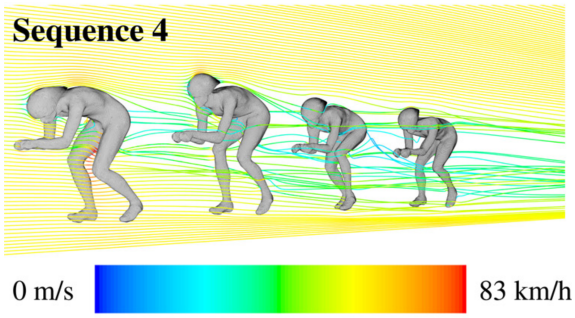

Figure 3.5: Streamlines of velocity computed using a CFD RANS method, plotted around a drafting line of cyclists (Defraeye et al. 2014)

3.2. Aerodynamic Flow Structures

Similar to other bluff bodies, including finite cylinders, the drag experienced by a cyclist is predominantly affected by fundamental flow structures and not just the frontal area, as observed in experimental testing by Crouch 2013 and Crouch et al. 2014, where they suggest that the drag coefficient plays a vital role in determining the aerodynamic drag of the cyclist. Cycling's governing body, the Union Cycliste Internationale (UCI), have drafted their competition rules in such a way as to restrict the rider's position, causing limited modifications to frontal area to be possible anyway, as stated by Crouch et al. 2014. This naturally has meant that the majority of gains in cycling performance in the last decade have originated from reduction in drag coefficient. In search of these gains, several studies have explored the most dominant flow structures around a cyclist, with the ambition of understanding and controlling them for performance benefits.

Pressure probe measurements using a wake rake and static probes of a full-scaled mannequin in a wind tunnel study by Crouch et al. 2014 captured the drag variation of a cyclist across a full pedal stroke and captured the key flow structures, and is similar to that displayed in Figure 3.1. A plot of the results measured may be observed in Figure 3.6, showing that despite both the frontal area and drag coefficient varying with pedal stroke angle, θ_p, the variation is non-linear, indicating the non-linear relationship between the two variables. A high drag condition was measured at $\theta_p = 75°$ where the left leg of the cyclist is nearly fully raised and right leg is extended. The low drag condition is measured with both legs being symmetrically level with each other, at $\theta_p = 0°$.

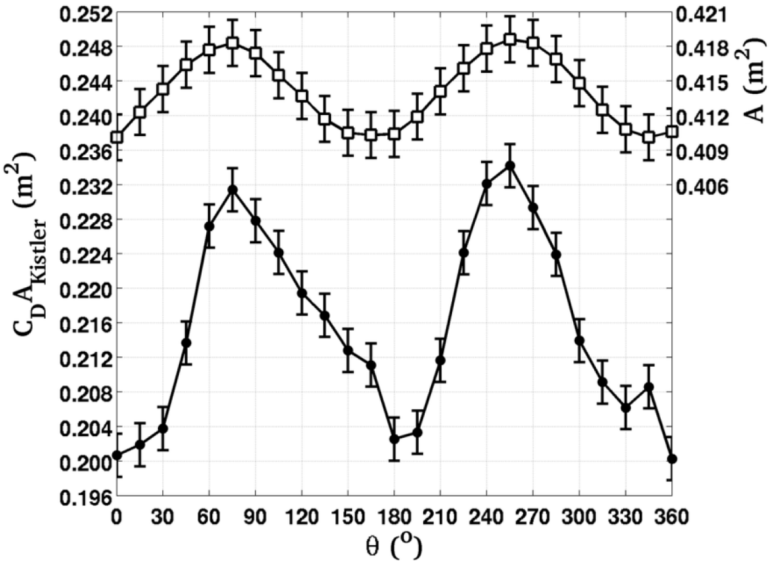

Figure 3.6: Variation in frontal area and drag area of a cyclist with the pedal stroke angle (θ_p) (Crouch et al. 2014)

In Figure 3.7 the flow structures behind the variation in drag coefficient may be visualised. Crouch et al. 2014 observes that the main cause for the variation in drag forces is due to a low velocity turbulent region developing beneath the hips. This is clearly visible in Figure 3.7, with a large momentum deficit being present in the $\theta_p = 75°$ case. The main difference between the low and high drag condition is the point at which flow separates from the hip and lower wake, which dictates the size of wake and associated drag forces. In the high drag condition, flow attachment remains on the side torso of the raised leg (left side) leading to relatively high streamwise velocity. However, considerable velocity deficits occur below the hip due to flow separation. On the extended leg (right hand side) part of the body, earlier flow separation occurs and at a higher hip position, increasing the overall size of the wake and velocity deficit. In the low drag condition, the symmetrical leg positions leads to symmetrical flow separation across the lower back. Crouch 2013 notes that although this increases the wake size and velocity deficit above the hips, the separated wake region below the hips is largely reduced, which consequently reduces the drag forces, as this is where the predominance of drag forces originate from.

The vorticity plots in Figure 3.7 show that the flow separation regions in the high drag condition are associated with areas of high vorticity, with unequal streamwise counter-rotating vortices existing. Crouch 2013 states that the formation of these vortices originates from pressure gradients between the hip region and torso underside. The strong vorticity in the high drag condition is generated from the flow separation discussed above, with a large vortex being present on the extended leg side, and two smaller pair vortices on the raised leg side. This large flow asymmetry with the counter rotating vortices being at their highest strength, promotes a large down wash effect of the wake. Meanwhile, in the low drag configuration, the strength of the vortices are found to be relatively weak and equal in magnitude, with two counter rotating pairs originating from the upper and inner thighs. The mutual interaction between the vortices reduces the size of the wake and drag forces. A summary of the primary flow structures around a cyclist are shown in Figure 3.8, showing the vortices shed in the high drag condition.

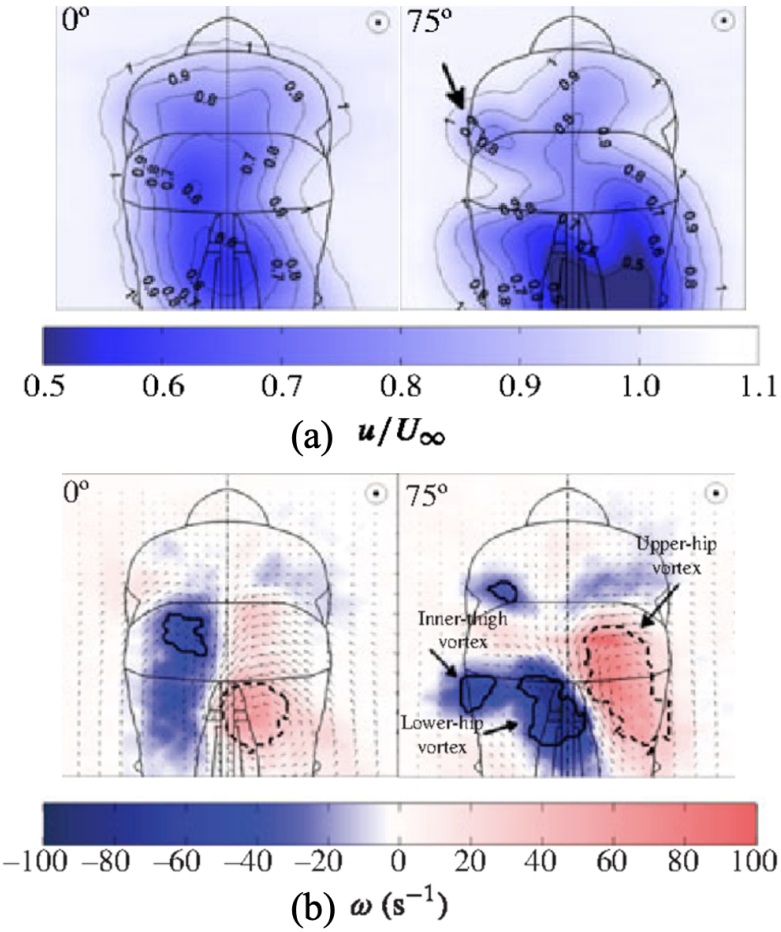

Figure 3.7: Flow comparison in the wake located one torso chord length downstream of the cyclists trailing edge. The low drag (θ_p = 0°) and high drag θ_p = 75° conditions are shown using (a) streamwise velocity component and (b) streamwise vorticity, with vortex structures defined using the swirling strength criterion (Crouch et al. 2014)

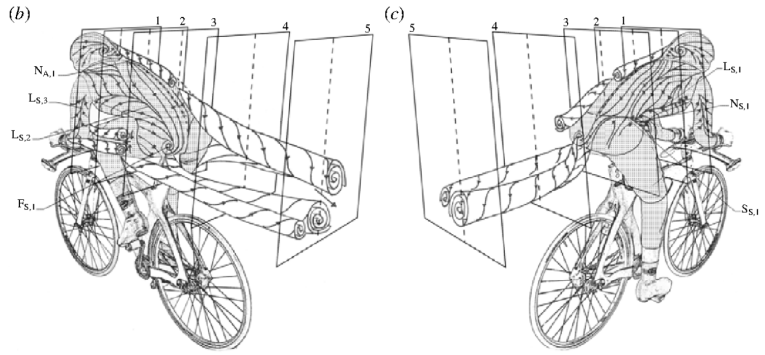

Figure 3.8: Schematic diagram of the vortex structures shed from a cyclist in the high drag condition, from both a left and right viewing point (Crouch et al. 2014)

3.3. Interaction effects between drafting cyclists

When two cyclists are moving in tandem, several interaction effects need to be considered, which have considerable impact on the drag forces of each cyclist. Limited research has been undertaken investigating the flow structures and physics in drafting and if the dominant effects behind the drag

reduction is either an upstream or downstream effect. Research by Barry et al. 2016a utilised PIV measurement in a water tunnel with two 1/10 scaled drafting cyclist models, measuring the flow structures around both the upstream and downstream cyclist. A notable result was that the wake of the trailing cyclist was observed to be similar in characteristics to that of an individual cyclist despite a considerable disturbance upstream being measured. The primary vortices shed behind the trailing cyclists were similar to individual cases, suggesting that a largely upstream effect was the cause for the measured trailing cyclist drag reduction. The dominant mechanism for this upstream effect is suggested to be a large reduction to the inflow velocity for the trailing cyclist, rather than a substantial change to the flow structures shed from the trailing cyclist. It can be seen in Figure 3.9 Plot (b), where at a close spacing the flow downstream of the lead cyclist is similar to that upstream of the trailing cyclist and a large low velocity region is present, indicating a low incoming velocity for the trailing cyclist.

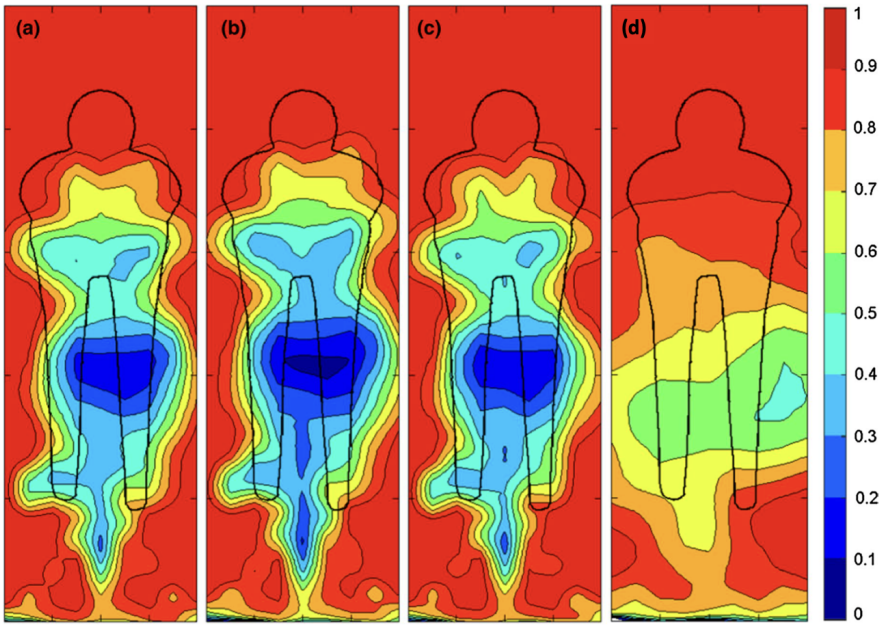

Figure 3.9: streamwise velocity contours of cyclists with symmetrical leg position at (a) Downstream of a single cyclist, (b) Downstream of the lead cyclist with a close spacing, (c) Downstream of the lead cyclist with a one bike length separated spacing, (d) Upstream of trailing cyclist with a one bike length separated spacing (Barry et al. 2016a)

This result was further clarified by Mahalingesh 2020 in the Ring of Fire technique, where the wake between the two drafting cyclists and downstream of the trailing cyclist were analysed. This research noted that the main characteristics of the flow upstream of the trailing cyclist was a region of low velocities and low pressure with reduced overall momentum relative to upstream flow for an individual cyclist. Barry et al. 2016a further notes that increasing the spacing between the two cyclists, increases flow mixing between the leading cyclist's wake and freestream occurring. This will allow energy recovery to occur, increasing the inflow velocity for the trailing cyclist, resulting in a larger drag force, which helps explain the positive correlation between drag and spacing observed in numerous studies including Kyle 1979, Zdravkovich et al. 1996, Edwards and Byrnes 2007 and Blocken et al. 2013. Of note was that as the spacing between the cyclists was increased, the low velocity wake region experienced by the trailing cyclist was smaller (or non-existent), demonstrating the downwash induced in a cyclists wake, caused by the leading cyclist's downward flow curvature and coupled trailing vortices. In Plot (d) of Figure 3.9 this is apparent with much higher relative velocities being present upstream of the trailing cyclist, including at lower Z-height locations, compared with Plot (b).

An interesting result from Mahalingesh 2020 was that, unlike with Barry et al. 2016a, when analysing the wake of the trailing cyclist, a reduction in peak absolute C_p was measured. This result was also found by Blocken et al. 2013, with a reduced under pressure measured behind both the upstream and downstream cyclist. Another interference phenomena observed by Mahalingesh 2020 was a slight variation in wake shape compared with an individual configuration. This can be observed in Figure 3.10, where the isolines of normalised streamwise wake velocity $w = 0.95$ for various different configurations are plotted. The low speed wake size for the trailing cyclist was consistently observed to be smaller than that of an individual cyclist, even when compared with that produced by the smallest sized cyclist. It was found that the leading cyclist's size indeed had a slight effect on the shape of the trailing cyclist's wake, with the most noticeable trend being that when a large size cyclist lead out a small size cyclist (L-S configuration), this resulted in a taller, yet narrower wake compared with the Medium-Small (M-S) combination. The author notes, however, that the comparison between instantaneous data for the two test configurations is not ideal for statistical analysis and that paired with the measurement uncertainty of the Ring of Fire, results in inconclusive observations, which should not be confidently compared with.

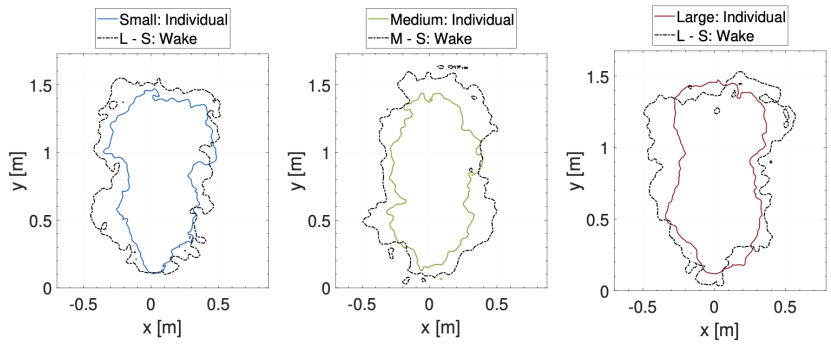

Figure 3.10: Isolines of normalised streamwise wake velocity $w = 0.95$ behind the trailing cyclist for various configurations (Mahalingesh 2020)

Meanwhile, Barry et al. 2016a also noticed drag reduction effects on the upstream cyclist in drafting configurations. At close spacings, the over pressure region in front of the trailing cyclist would interact with the wake of the leading cyclist, increasing the base pressure coefficient and reducing the drag coefficient. In Figure 3.9 this effect is evident in Plot (b), where a small region of stagnate flow is present that does not occur behind an individual cyclist in Plot (a). This upstream effect on the lead cyclist does disappear however, at larger spacings with no stagnate flow region being present in Plot (c). Interestingly, in the coast-down study by Kyle 1979, it was observed that for the drafting cyclists, the positioning in the pace line had no effect on the measured drag and the upstream cyclists found no drag reduction from having another cyclist draft behind. This contradicts several studies where around a 2-5% drag reduction has been measured for the leading cyclists. In the CFD based study performed by Blocken et al. 2013 on two drafting cyclists in a TT position, up to a 2.6% drag reduction compared with an isolated cyclist condition was found. It is noted that the main cause for the leading cyclist's drag reduction is due to the trailing cyclist's presence creating a higher minimum C_p existing in the wake, lowering the drag force. A further observation noted was that as the lead cyclist's position became more aerodynamic, the experienced drag reduction increased. This is explained with the over pressure region in front of the trailing cyclist moving closer to the upstream cyclist, increasing the wake interference effect. Wind tunnel testing of four cyclists in tandem by Barry et al. 2015 found an average 5% reduction in drag for the lead cyclist, confirming that an interactive upwash effect occurs in tandem drafting.

Interestingly, CFD testing of an entire team trial group made up of nine cyclists by Blocken et al. 2018 found that it was not always correct to state the rearwards most cyclist would experience the largest drag reduction. For groups of six cyclists or more (with a 50mm wheel spacing), a 58.3% drag reduction for the second to last cyclist was measured, compared with a 57.5% drag reduction for the last cyclist. It may also be noted, that as the number of cyclists drafting in a group increased, the average drag reduction across the entire group also increased, resulting in a lower total drag force for the entire group.

3.4. Longitudinal spacing

Similar to the tandem cylinder configuration, increasing the spacing between two cyclists, increases the drag coefficient for both the upstream and downstream cyclist. As mentioned earlier, Barry et al. 2016a noted larger levels of mixing between the upstream cyclist's wake and freestream, increasing the incoming velocity for the downstream cyclist and $C_{d,down}$. Additionally, similar to the tandem cylinder case, the trailing cyclist's over pressure region reduces the drag coefficient of the upstream cyclist. However, a dissimilar phenomena is that no fluctuation in drag coefficient at close spacings (like that noted by Alam et al. 2003a) is observed with drafting cyclists. This is evident in Figure 3.11, where Blocken et al. 2013 observed a linear variation in drag reduction for the trailing cyclist with spacing.

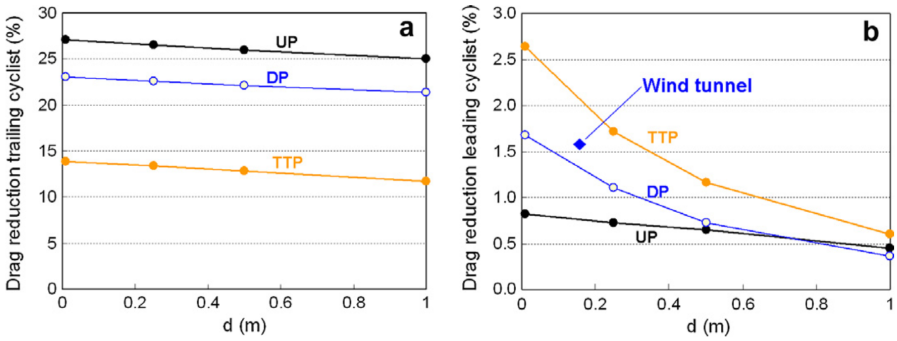

Figure 3.11: Variations in drag reduction with wheel gap spacing for (a) the trailing cyclist and (b) leading cyclist in differing positions. UP: Upright position, DP: Drop bar position, TTP: Time-trial position (Blocken et al. 2013)

Additionally, the upstream drag reduction effect on $C_{d,up}$ is significantly smaller for cyclists, maximising around 5% (Torre and Íñiguez 2009, Barry et al. 2015), while Alam et al. 2003a measured a maximum 10% drag reduction for an upstream infinite cylinder. This is firstly because the longitudinal spacing between the cyclists is different to that of cylinders, with the bicycle frame and wheels extended in front and behind the cyclist body. Therefore, typically, cyclist spacing is defined as the gap between the leading and trailing cyclists wheels. This results in close spacings for cyclists not being possible, where the majority of the drag fluctuation effects for cylinders occur. Additionally, with 70 - 80% of drag forces originating from the cyclist body (Kyle and Burke 1984, Defraeye et al. 2010), this indicates that despite the bicycle frames being close together, most flow interference effects are derived from the cyclist body, which are further apart. Observing Figure 3.11, it can be derived that with increased spacing, the drag reduction for the leading cyclist quickly reduces to near 0%, indicating similar drag forces to an isolated cyclist.

Interestingly, studies measuring the aerodynamic drag of drafting cyclists in wind tunnels typically measure larger drag reductions compared with outdoor studies. The drag reduction for the downstream

drafting cyclist was recorded to vary from around 54% with no wheel gap distance to roughly 40% at a two meter separation distance by Kawamura 1953, while Zdravkovich et al. 1996 measured a 49% drag reduction for closest tandem arrangement, with both studies conducted in the wind tunnel. Meanwhile, in a similar racing position to Kawamura 1953, the coast down test by Kyle 1979 measured a 39% drag reduction with a roughly zero meter wheel gap between the two cyclists. Analysing Figure 3.12, it can be observed that the coast down test underestimated the drag reduction at all spacings. Kyle 1979 explains this result is due to the effect of misalignment between the cyclists, with either wheel overlap or lateral spacing occurring between the cyclists. However, similar to the wind tunnel results from Kawamura 1953 and Zdravkovich et al. 1996 and CFD results from Blocken et al. 2013, a continuous loss in drag reduction with increased wheel gap spacing occurs without any fluctuations being measured.

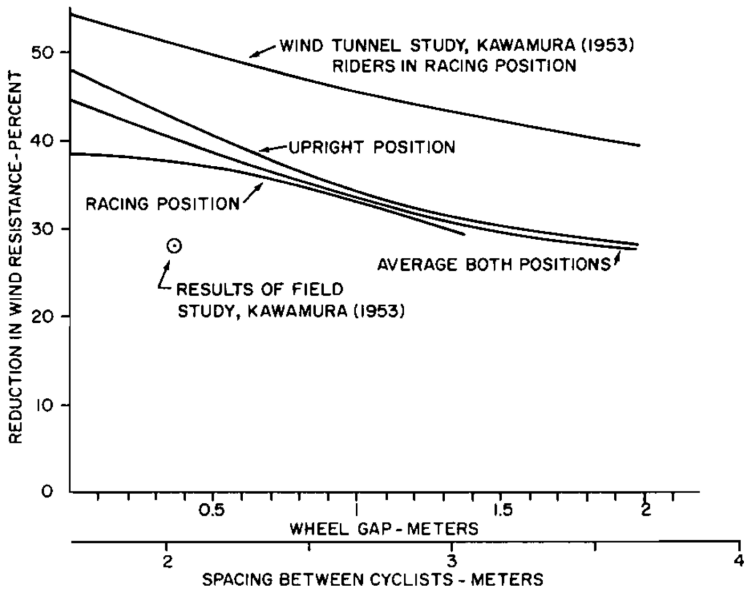

Figure 3.12: Variations in drag reduction for the trailing cyclist with wheel gap spacing (Kyle 1979)

3.5. Size effects

The aerodynamics of drafting in cycling has been studied intensely through various methods, and several studies have found that varying the position of a cyclist has wide ranging effects on the drag forces for all cyclists in a drafting line (Blocken et al. 2013, Defraeye et al. 2014, Barry et al. 2015, Shirasaki et al. 2017). As the position of a cyclist varies the frontal and drag area, this can be thought of as an indirect size effect. CFD research of 4 cyclists in tandem with differing frontal area conducted by Defraeye et al. 2014 analysed the drag area variation for each cyclist when the sequence of positioning in the draft line was changed. It was observed that when a cyclist with a relatively small drag area followed one with a large drag area, a 31% drag reduction was measured downstream, with a 2% drag reduction upstream. Meanwhile, when the same large cyclist drafted an intermediate drag area cyclist, a 24% drag reduction downstream, and a 4% drag reduction upstream was measured. Although differences in individual drag area do not fully correlate with differences in cyclist size, an observation from this study is that having a lead cyclist with a larger drag area results in higher drag reductions for the drafting cyclist. Meanwhile, when the trailing cyclist has a large drag area, this also results in increased drag

reduction for the leading cyclist, however, to a smaller extent.

Edwards and Byrnes 2007 performed a similar investigation in the drag reduction for drafting cyclists, however, with the conduction of outdoor experiments involving various test cyclists of differing size. The method depended upon cyclist power output measurements and bike speed sensors to determine the drag coefficient of the cyclist. In this comprehensive study, 15 cyclists of various frontal areas, and drag areas cycled in groups of two in various configurations. A cyclist with a small, intermediate and large drag area were selected from the pool of athletes and designated as lead cyclists, with the remaining 12 cyclists being designated drafters. It was observed that in all drafting configurations, the drag reduction for the trailing cyclist increased when the drag area of the upstream increased, however, the extent of the drag reduction varied significantly and unpredictably. The results from this may be viewed in Figure 3.13, where for each drafting cyclist a positive correlation with leading cyclist drag area is evident, but to a differing degree. This is noted by the authors with the comment that the difference in individual slope regressions is affected by large inter-individual variability.

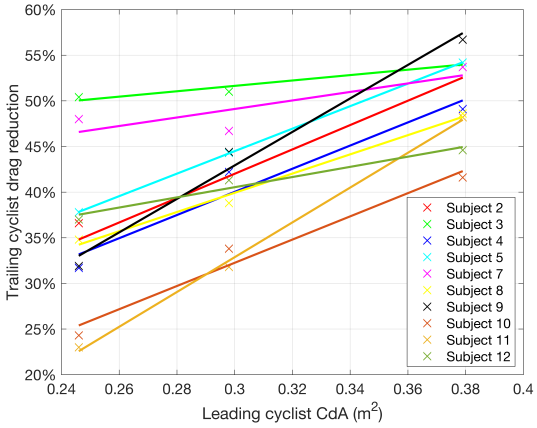

Figure 3.13: Variation in the drag reduction for the trailing cyclist when drafting lead cyclists of differing drag areas (Edwards and Byrnes 2007)

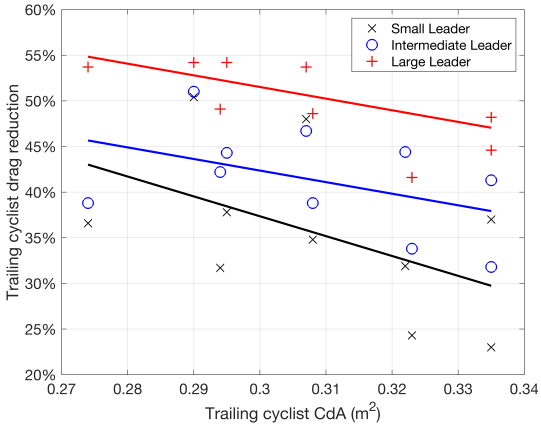

Figure 3.14: The effect the trailing cyclist's drag area has on its drag reduction when following a lead cyclist of differing drag areas (Edwards and Byrnes 2007)

When analysing the data from Edwards and Byrnes 2007 in more detail, several more anomalies appear. One can observe that when drafting the largest cyclist, a relatively intermediate sized cyclist, Subject 9, experienced a larger drag reduction than Subject 2, a relatively small sized cyclist. Additionally, when drafting the smallest lead cyclist, Subject 2 and Subject 12 experienced similar levels of drag reduction despite being on polar opposites of the sizing scale. The high statistical uncertainty and limitations of the testing method is clear in Figure 3.14, where a large scatter around the regression line is evident. With this high level of uncertainty in statistical data, it is not possible to properly analyse trends in detail and only possibly at a macro scale in terms of data averaging. Additionally, the outdoor testing method by Edwards and Byrnes 2007 is only able to derive the drag area, which does not necessarily mean that size interaction effects were directly measured.

Concluding from their study, Edwards and Byrnes 2007 state that the optimal sizing combination for two drafting cyclists for drag reduction is when the leading cyclist has a large frontal area in order to provide shelter to the trailing cyclist, while still having a low drag coefficient, such that the leader can maintain a high velocity. However, the possibility of such a phenomena is unclear and not researched. Typical aerodynamic intuition suggests that a low drag coefficient for a body is usually paired with a

relatively small wake size or a wake with a low drop in total pressure relative to the freestream. This would result in a small drag reduction for a trailing object and therefore, be counter-productive for cyclists drafting in tandem.

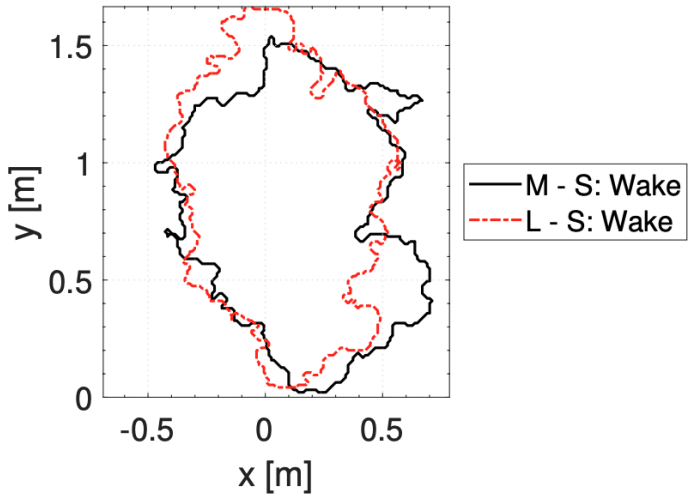

Figure 3.15: Isoline of 95% streamwise freestream velocity comparison of instantaneous velocity in the wake of a trailing cyclist for various size combinations from Mahalingesh 2020

Although studies with differing drag areas, such as Defraeye et al. 2014 and Edwards and Byrnes 2007, give insight into size effects, the direct interaction effects due to size on drag reduction have remained a relative unknown. However, recent studies using novel flow visualisation methods have begun to address this gap in knowledge. Mahalingesh 2020 analysed size effects in drafting using the novel Ring of Fire method, where the wake sizes of each cyclist was captured in detail. The subjects were three professional cyclists of differing size and categorised as Small (S), Medium (M) and Large (L) in size. The effect that cyclist size had on aerodynamic drag was studied and instantaneous results are shown in Figure 3.15 and Figure 3.16. It was found that the leading cyclist's size indeed had an effect on the shape of the trailing cyclist's wake, with the most noticeable trend being that the Large-Small (L-S) cyclist combination resulted in a taller, yet narrower wake compared with the Medium-Small (M-S) combination. A 2.8% variation in wake size between the two cyclist combinations was determined, while a roughly 3% difference in drag reduction was found. The author notes, however, that the comparison between instantaneous data for these two test configurations is not ideal for statistical analysis and paired with the measurement uncertainty of the Ring of Fire, results in inconclusive observations.

In Figure 3.16, the upstream effect that the trailing cyclist has on the lead cyclist is also apparent and was able to be captured by the Ring of Fire method. It must first be noted that a lower pressure coefficient is found behind the lead cyclist in a draft configuration, which contradicts findings by Blocken et al. 2013and Barry et al. 2016a. The authors notes this would counter-intuitively increase $C_{d,up}$, and due to the low number of datasets cannot be confirmed to be a true ensemble averaged effect. However, one can deduce from the C_p distribution that from the spatial average, higher pressure coefficient values occur behind the lead cyclist. Additionally, this effect is more significant when the relative size of the trailing cyclist is similar to that of the lead cyclist. Mahalingesh 2020 observed that a 26.4% lower peak velocity was measured in between the two cyclists for the M-S configuration compared with an individual case. Meanwhile, only a 5.7% reduction was measured for the L-S configuration.

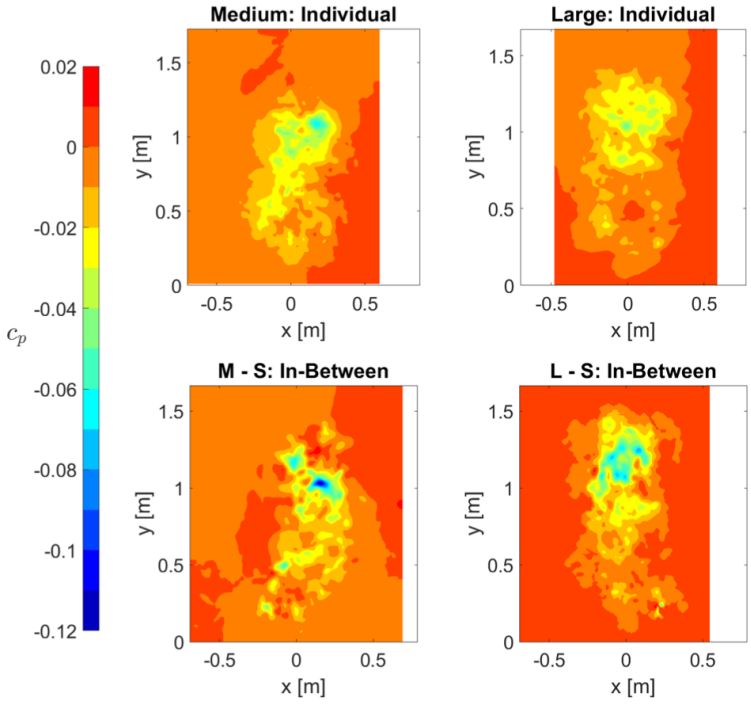

Figure 3.16: Ensemble average pressure coefficient comparison between the wake behind an individual cyclist and in between two cyclists (Mahalingesh 2020)

3.6. Lateral Spacing

Both Mahalingesh 2020 and Spoelstra et al. 2021 comment that using the Ring of Fire to measure the effect of cyclist size in drafting is hampered by the inconsistent variation in drafting distance and lateral spacing between the two cyclists. This prevented the ability to apply ensemble averaging over multiple tests and increased the uncertainty in the measured results. Similar phenomena are noted by other experimental studies involving human participants, including Kyle 1979 and Edwards and Byrnes 2007. In the research by Kyle 1979, the desire to minimise the drafting distance between the two cyclists resulted in numerous occasions where the drafting cyclist unavoidably overlapped their front wheel with the leading cyclist's rear wheel, causing an unmeasured variation in drafting position. Edwards and Byrnes 2007 commented that the difference in drag reduction correlation measured between the cyclist combinations existed due to a "difference in drafter's skill rather than their aerodynamic characteristics", suggesting that less skilled cyclists will hold, on average, larger and less consistent drafting distances when drafting a leading cyclist. Experimental wind tunnel testing by Zdravkovich et al. 1996, Barry et al. 2014 and Shirasaki et al. 2019 investigated the effect of longitudinal and lateral spacings when drafting another cyclist. With the rearward most point of the leading cyclist's rear wheel being the point of origin, both Zdravkovich et al. 1996 and Shirasaki et al. 2017 measure a roughly 12% drop in drag reduction when varying the lateral spacing from 0 metres to 0.2 - 0.25 metres, while Barry et al. 2014 measured a roughly 17% drop, due to the significantly diminished sheltering for the trailing cyclist. As these are typical lateral distances that can be experienced in typical experimental cycling conditions, these spacing effects must be seriously considered. It additionally explains the typically lower measured drag reductions in track testing experiments (Kyle 1979, Broker et al. 1999) compared with wind tunnel

experiments as shown in Figure 3.17. This is because there is an inability to control and maintain spacial positioning of the two cyclists in track testing, with the added consequence of reducing the repeatability of the data.

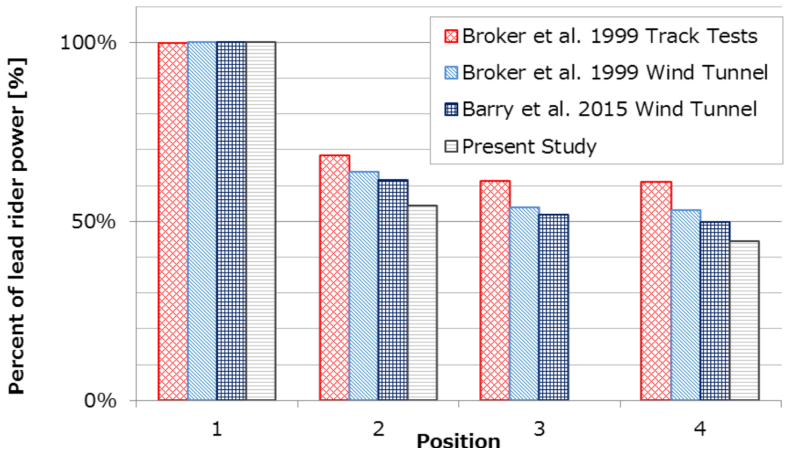

Figure 3.17: Reduction in power requirement for four cyclists drafting in tandem. The results labelled "Present Study" were captured from a wind tunnel testing method of full scale human cyclists. (Shirasaki et al. 2017)

3.7. Flow visualisation methods for cyclists

Flow visualisation using PIV for two cyclists in tandem is marred with optical access complications and difficulties in shadow and reflection regions creating insufficient image pairs for correlation calculations. As the area between the two cyclists is where the majority of drag reduction for both cyclists occurs (Blocken et al. 2013, Barry et al. 2016a, Mahalingesh 2020), it is essential to measure this region to understand how the key flow structures alter with spacing and size ratio and what impact they have on drag forces. Barry et al. 2016a notes that when two tandem cyclists are in a typical drafting position with minimal spacing, there is only a very small narrow region where a full cross section of the wake in between the two cyclists may be viewed. The usage of stereoscopic PIV in this narrow region would require large camera angles and despite this, two simultaneous views of the entire field of view plane would not be possible due to object blockage. This would result in perspective error, increasing the uncertainty associated with the data (Prasad 2000). The usage of 3D volumetric PTV using a robotic arm has the potential of sufficiently analysing the flow structure interaction between the two cyclists in the in-between wake region. However, as noted by Jux 2022, the inherent disadvantage associated with this technique is the lack of spatial resolution possible. As the dominant flow structures around the model cyclists are predicted to be only around $1 - 2cm$ in size, it is conceivable that initial measurement using the robotic arm will not sufficiently capture these vortex structures. However, if an extended number of particles are tracked in this region, the spatial resolution collected will increase and possibly capture these flow structures.

A simpler and more reliable technique to obtain 3D flow structures is to use multiple spaced planes, capturing 2D velocity components. This method has been utilised by Barry et al. 2016a to analyse the difficult region between two drafting cyclists at close spacing. The composite technique utilised multiple laterally spaced X-Z planes focused solely on the domain region between the two cyclists. By interpolating laterally (Y-direction) the captured velocity components between each of plane, a wake

cross-sectional streamwise velocity field could be created. This method is similar to that proposed for the tandem cylinder configuration, however, utilising multiple spaced X-Z planes instead of X-Y planes.

4

Research Questions

In this chapter the research questions that form the basis of this study are detailed and the answers that the experimental campaign must address is covered. The primary research aim of this master's thesis is to investigate what effect the cyclist size and spacing configuration has on the drag reduction for cyclists drafting in tandem. For this, research areas such as cycling aerodynamics and wake structures must be analysed. Furthermore, to better understand diameter ratio and spacing effects a simpler flow case involving drafting cylinders must be considered.

4.1. Section 1: Cylinders

1. To what extent does the drag reduction for both the upstream and downstream cylinder vary when the size ratio and spacing configuration change?
2. How does the inner wake region and wake width vary behind an upstream cylinder when a tandem cylinder is placed downstream, and what effect does the size ratio and spacing have on these variations?
3. How is the wake momentum deficit behind the downstream cylinder altered when the size ratio and spacing of the upstream cylinder is altered?
4. For the downstream cylinder, what effect does the leading edge and trailing edge flow condition have on the drag reduction and how are these affected by the size and spacing configuration?
5. What is the correlation between the downstream object's drag and overall group's drag for finite cylinders in tandem?
6. How accurately does the flow structures around tandem finite cylinder mimic that around drafting cyclists?

4.2. Section 2: Cyclists

1. To what extent does the drag reduction for both the upstream and downstream cyclist vary when the size ratio and spacing configuration change?
2. How does the wake width and low momentum region behind an upstream cyclist in a drafting configuration change when a trailing cyclist is present, and how does this effect alter between size ratio and spacing configurations?
3. Does the wake size and low momentum region behind a downstream cyclist alter when drafting a cyclist, and what influence does the size ratio and spacing have on this effect?
4. What correlation does the drag reduction of the trailing cyclist have with the overall group drag?
5. To what extent does the drag reduction characteristics and variations with size ratio and spacing match those observed with tandem finite cylinders?

5

Experimental set up and methodology

In this chapter, the experimental methodology for this study is covered. This includes set up descriptions, methodology outlines and detailed analysis of the models and configurations that have been chosen upon.

5.1. Overview

As has been described in the previous section, several different classification of experimental methods have been used to measure the aerodynamic forces and flow structures around tandem cylinders and drafting cyclists. In order to obtain the best results to answer the aforementioned research questions, an experimental process involving the usage of cylinder and cyclist models in a wind tunnel is chosen upon. A force balance test for detailed drag measurements is performed, alongside flow visualisation tests using multi-planar 2D PIV.

5.2. Cylinder Models

A truncated cylinder design, with an aspect ratio, $AR = 3$, is chosen, in order to mimic the geometrical shape and flow structures around a cyclist object, including the shed counter rotating trailing vortices around the top edges (Crouch et al. 2014, Schneiders et al. 2016, Sumner and Reitenbach 2019). A compromise in cylinder diameter is required between maximising the Reynolds number and maintaining the cylinder blockage ratio below 10%. The maximum baseline cylinder diameter that could be achieved is 60mm, with a height of 180mm, resulting in a blockage ratio of 6.75%. In order to sufficiently investigate size interaction effects, whilst also relating to typical size ratios in professional cycling, five variations in upstream cylinder diameter, d are tested, varying by 20% from the baseline size. This results in a pool of upstream cylinder diameters including 48mm ($d/D = 0.8$), 54mm ($d/D = 0.9$), 60mm ($d/D = 1.0$), 66mm ($d/D = 1.1$) and 72mm ($d/D = 1.2$). With each cylinder having an $AR = 3$,

the cylinder heights are 144mm, 162mm, 180mm, 198mm and 216mm respectively. The cylinders are manufactured from polycaprolactam (Nylon 6) rods which are machined down to the specific diameters and heights, allowing for a smooth, uniform surface finish. The blockage ratio of the models varies from 4.32% to 9.72% in a 400mm by 400mm wind tunnel test section, and according to guidelines from Barlow et al. 1999 and Anthoine et al. 2009, the Glauert blockage correction is applied to cylinder data to achieve the corrected drag forces.

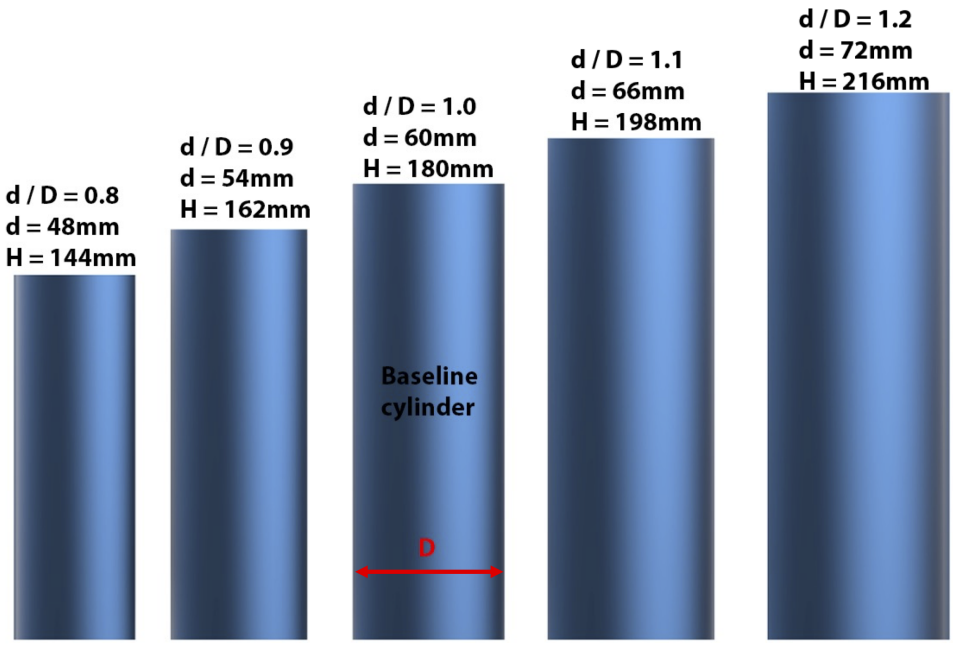

Figure 5.1: The cylinder models of different size ratio used in study

In order to validate the force balance data collected with that from previous research, two near-full span cylinders of 60mm diameter are also tested. These cylinders have a height of 398mm, resulting in a 2mm gap between the cylinder and the test section wall, allowing free movement of the cylinder to occur. Despite this, large oscillatory movement of the cylinders was not observed, therefore allowing for steady state analysis to be performed. For each cylinder model, zigzag strips of 0.25 mm thickness, and 12mm width between peaks are applied to the $\theta = 60°$ leading edge point of the cylinder to perform boundary layer tripping. For a more detailed understanding of the boundary layer tripping used for the cylinder models, the test section photo in Figure A.1 in Appendix A may be observed.

5.3. Cyclist Models

The chosen cyclist model for this experiment is a high resolution 3D scanned CAD model of the former professional cyclist, Tom Domoulin, in the time trial position. This cyclist model has been used extensively in previous cycling aerodynamics research (Terra et al. 2019, Spoelstra et al. 2021, Jux 2022), especially with PIV measurement systems. As the cyclist body generates 70-80% of the total drag (Kyle and Burke 1984) and generates the key flow structures that are of interest in this study, which originate from the hips, thighs and back (Crouch 2013), the usage of an accurate cyclist model is necessary. As the drag forces and flow structures around the bicycle model are of lesser importance, it is deemed sufficient to use a simplified bicycle geometry for this experiment, where the gear system, saddle, aerobars and

wheel spokes have all been removed. The usage of a double disc wheel design is also used. This bicycle design significantly aids in the manufacturing of the model and allows for a more consistent model shape to be produced. The bike model is attached to a thin, rectangular flat plate, with an M8 sized screw attached for mounting.

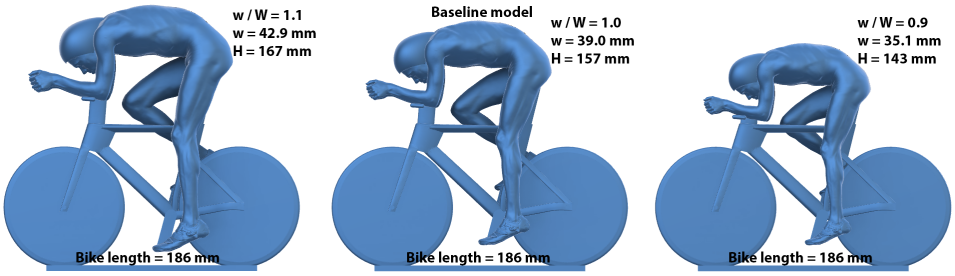

Figure 5.2: The cyclist models of different size ratio used in study

The baseline cyclist model is a 10.8% sized scaled version of the Tom Domouolin time trial model, with the bicycle model adapted around this cyclist shape size. At this scale, the overall dimensions of the cyclist model with the bike included is 40.9 mm width, 185.8 mm length and 157.0 mm height for the baseline model. Detailed body dimensions for the full scale cyclist model may found in Terra et al. 2016 or Jux 2022. The characteristic length of the cyclist model is typically either the torso length or the shoulder width. The shoulder width, $W = 39mm$, is chosen as the characteristic length due to it being less susceptible to subjective measurement, especially for smaller scaled models. This scaling allows for the largest scale one-piece models to be produced using the available additive manufacturing methods. A one-piece model prevents any additional uncertainties being associated with the experiment from the manufacturing process. The models are 3D printed using an Anycubic Photon Mono X 6K SLA printer. In order to investigate size effects in drafting, two additional sized cycling models of different sizes are also used which are at 90% scale ($w/W = 0.9$) and 110% scale ($w/W = 1.1$) relative the baseline model. This range is based off the data pool of rider height and shoulder width lengths within the *Team DSM* roster. The frontal areas of the $w/W = 0.9$, $w/W = 1.0$ and $w/W = 1.1$ cyclist models are $A = 3453mm^2$, $A = 4126mm^2$ and $A = 4992mm^2$ respectively and the shoulder widths are $w = 35.1mm$, $w = 39.0mm$ and $w = 42.9mm$. A detailed view of the surface finish for the 3D printed cyclist model can be viewed in Figure B.1 in Appendix B.

5.4. Model configuration and spacing design

For the cylinder models, a spacing, L, is defined as the distance between the centre points of the two cylinders, and is non-dimensionalised by the 60mm diameter, D, of the trailing baseline cylinder. The dimensionless spacing, L/D is varied from 2.0 to 3.5 which mimics distances between drafting cyclist bodies, and is associated with a similar, representative flow regime. For the cyclist models, the spacing distance is defined as the distance between the lead cyclist's rear wheel's trailing edge and trailing cyclist's front wheel's leading edge. The cyclist bike spacing, L, is non-dimensionalised by the shoulder width of the trailing cyclist, L/W. The test section design allows for the variation in spacing from $L/W = 0$, where there is no gap between the wheels of the two cyclist's bikes to $L/W = 3.0$. This range of spacings allows for a significant variation in drag forces to be experienced in a similar format to that experienced by a group of professional cyclists in a competition environment.

5.5. Wind Tunnel: Wind speeds and Reynolds number

The chosen wind tunnel is the W-tunnel at the Delft University of Technology, which has a maximum operating velocity of 35m/s and minimum turbulence intensity of 0.5% (TU-Delft n.d.). The typically experienced velocities of a team trial or sprint train in a professional competition, is around 15 m/s and basing the characteristic length on the shoulder width of the full scale Tom Domoulin model (W = 410 mm), this results in a Reynolds number estimate of roughly $Re = 4 \times 10^5$ in normal ambient air conditions. Testing the scaled cyclist models, using a similar characteristic length definition, in the wind tunnel at a velocity of 30 m/s results in $Re = 8 \times 10^4$ for the baseline sized model. This lower Reynolds number risks the possibility of laminar separation occurring on the model, especially around the forearm and hip/thigh region, inducing larger wake regions with increased drag. Additionally, boundary layer flow tripping, using zigzag strips, is applied to both the floor and ceiling upstream of the models.

For the cylinder models, the Reynolds number ranges from $0.97 \times 10^5 < Re < 1.45 \times 10^5$ which is similar to that experienced by the full scale cyclist. As already noted, zigzag strips are applied to the cylinder models to perform boundary layer tripping, controlling the point of transition for each test configuration and avoiding laminar separation. Additionally, the usage of flow tripping will prevent testing in a drag crisis regime where large variations in forces occur. Wind tunnel testing with zigzag strips on a cylinder by Timmer and Veldhuis 2021 found sufficient tripping and avoidance of a drag crisis around the $Re = 1 \times 10^5$ region. As there is no previous research or standard for tripping of scaled cyclist models, no zigzag strips are placed on the model itself as the introduction of such items would introduce additional unknown variables. The leading edge surface of the cyclist model can be viewed in Figure B.1 in Appendix B. However, it should be noted that flow tripping on the test section floor and ceiling for these experiment configuration will still take place. These can be viewed in Figure 5.3.

5.6. Force balance campaign

5.6.1. Test section

For the force balance test, a 400mm by 400mm closed test section of 2 metre length is used with a removable plate on the test section floor. This plate is placed in the middle of the 2 metre test section length, allowing for force balance and model access to the wind tunnel test section. The force balance externally connects to a 150mm flat circular platform, which the measured test object is attached to and slots through a 151mm gap in the removable plate, as seen in Figure 5.3. This creates a smooth floor surface with minimal gaps, while still allowing for free movement of the test object to be measured by the force balance. With only one available force balance, in order to measure the total group forces on the tandem objects, dual measurement campaigns of both the upstream and downstream object is performed. To accommodate for this, the test section plate is removed and rotated 180 degrees, before being reattached to the test section floor. This results in a slight difference in the streamwise distance from the tunnel outlet to the measuring platform between the upstream and downstream measurement campaigns.

Figure 5.3: Test section configuration for the force balance experiments, with the upstream object being measured. Additionally observable are zigzag strips placed both on the floor and ceiling boundaries upstream of the test area.

5.6.2. Force balance

The force balance is a strain-guage dual component design that can measure both the drag and lateral forces experienced by the attached model. Two strain gauges measure streamwise forces and are combined to get the total drag force, while a single, center spaced strain guage measures forces in the lateral direction. The measurement acquisition frequency is set to 2.5kHz to adequately capture all major, drag inducing flow phenomena, such as vortex shedding or shear layer attachment. Flow measurement over a 30 second time period are recorded and the ensemble average is taken to describe the major time averaged flow forces. To increase the reliability and accuracy of the force balance data, three repeat measurement of each of the tested configurations was performed, both for the upstream and downstream measured model. In order to reduce the systematic error caused by the placing the models in the incorrect position, the repeat measurements include removing the models and re-installing them in the identical configuration.

5.7. PIV campaign

As mentioned earlier, the most significant challenge associated with performing flow visualisation experiments on tandem objects is the narrow distance between objects being an impedance for optical access. Furthermore, the potentiality for strong reflections from the objects can decrease the relative light intensity of the tracer particles, reducing the accuracy of calculated vector data. As understanding the flow characteristics between the two tandem objects is an integral part of this study, tomographic

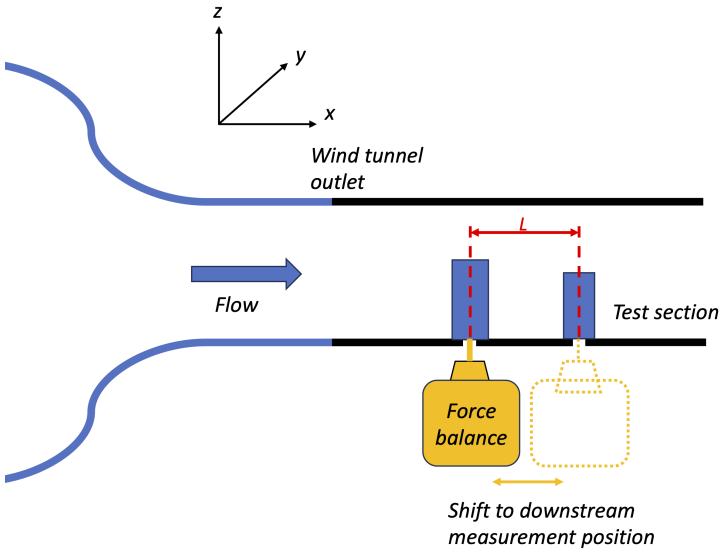

Figure 5.4: Schematic diagram of the wind tunnel set-up used for the force balance campaign. In this specific configuration, the cylinder models are displayed with the measurement of the upstream model.

flow visualisation is deemed unsuitable due to its inability to capture flow in this region. Furthermore, the requirement in this study to change the spacing and size ratio configuration of the tandem objects continuously varies the dimensions of the in-between region, which would require continuous modification to the set up of the four cameras in a tomographic set up. This is decided to be exceedingly time expensive and therefore tomographic PIV is not considered in this study. Further, an alternative volumetric flow visualisation method, namely a 4D Particle Tracking Velocity (PTV), or commonly referred to as "*Shake-the-box*" method, by *LaVision* should also be contemplated. Although this method of flow tracking has previously obtained detailed vector data and described flow patterns around full scale cyclist models, including by Shah 2017, Terra et al. 2019 and Jux 2022, its ability to adequately capture flow structures around scaled cycling models is uncertain. Jux 2022 noted that the smallest vortex sizes that were able to be captured by this method was roughly 40 mm, which is equivalent to the entire shoulder width of the cyclist models used in this study. It is therefore assumed that the "*Shake-the-box*" method is not suitable for capturing the smaller sized flow structures between scaled sized models and is therefore not utilised in this study.

The usage of stereoscopic PIV methods is additionally assosciated with complications for this study. The difficulty for optical access by model blockage would require the two camera set up to have large stereoscopic viewing angles, above 45°, for a laser sheet in the YZ-plane, which is outside the range recommended by Adrian and Westerweel 2010 for accurate capturing of the out-of-plane velocity component. For laser sheets in either the XY or XZ-plane, these viewing angle complications do not occur, however to capture the full 3D flow effects would require several different measurement planes. Most importantly however, similar to a tomographic set-up, although not as severe, translation and re-calibration of a stereoscopic set up is time intensive and not feasible for this study. Furthermore, although the vertical flow component, w, is useful in vortex identification and would be captured by stereoscopic PIV, it is not significant in drag determination for either a cylinder or cyclist, which is largely influenced by streamwise velocity effects, and is the prime focus of this study.

A simple, single camera PIV set up, measuring only 2D component velocity is deemed the optimal compromise between the quality of data gathered and its ability to capture 3D flow structures in a

time efficient manner. Barry et al. 2016a circumnavigated the difficulty of the optical access issues between two drafting cyclists by implementing a quasi-3D method of taking multiple XZ measurement planes, and interpolating the streamwise velocity between the planes. A similar method is executed in this study, however several XY measurement at various Z-heights is used instead. This is such that the important shear layer attachment and wake flow deficit between the two objects can be viewed in increased detail, something that was not possible in the study from Barry et al. 2016a. Additionally, the simplicity of the single camera set up allows for the re-positioning and re-calibration of the system to be swift and the testing of multiple configurations to be possible in an appropriate time frame.

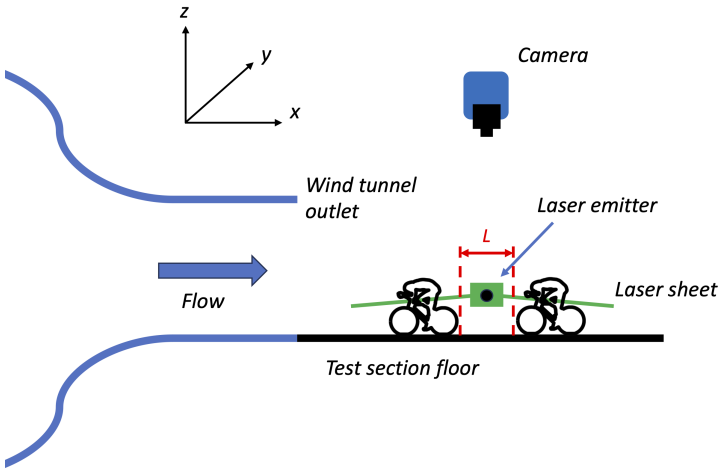

Figure 5.5: Schematic diagram of the wind tunnel set-up used for the PIV campaign.

5.7.1. Test matrix refinement

The test matrix for the PIV experiments is significantly smaller than that for the force balance experiment due to testing time constraints and the increased time intensity for PIV measurements. However, using results collected from the force balance experiments, the changes in configuration that evidently indicate large difference in drag reduction as well as certain anomalous data are tested. Therefore, only the $d/D = 0.8$, $d/D = 1$ and $d/D = 1.2$ cylinder models and $w/W = 0.9$, $w/W = 1$ and $w/W = 1.1$ cyclist models at two different spacings are measured. The $d/D = 0.9$ cylinder case, at $L/D = 3$, is also examined, to a limited extent, due to an interesting and peculiar aerodynamic phenomena being detected in the force balance data.

5.7.2. Test section and models

Similar to the force balance tests, for the flow visualisation PIV measurement campaign, the W-Tunnel is used and the tests are undertaken at a wind speed of $U_\infty = 30m/s$. An open test section is used, with sufficiently large floor plate dimensions of 500 mm width by 1000 mm length, ensuring that unintended flow phenomena such as flow re-circulation caused by the plate does not occur near the model. To prevent the occurrence of strong reflections off the models and reduce the noise of the collected data, both the cylinder and cyclist models are coated in a thin matt black pain layer. It may be noted that the thickness of the paint layer is negligible and its effect on the flow may be largely dismissed.

5.7.3. Laser system

For the light source in the PIV experiments, the *Quantel Evergreen 200* laser is used. The specifications of the laser system is a neodymium-doped yttrium aluminum garnet (Nd:YAG) laser of wavelength 1064 nm, before being halved to 532 nm by a harmonic generator. The laser is double pulsed, with maximum pulse energy of 200 mJ, and tests were conducted at 89% strength. The pulse rate of the laser is 15Hz, with a pulse length of 8 ns for each pulse. The laser operation is controlled through *DaVis* software by *LaVision*, including the strength and pulse rate.

5.7.4. Seeding system

For seeding, a *SAFEX* fog generator is used, producing non-toxic water-gycol based fog formed from *SAFEX normal power mix* fluid. The mean diameter of the fog particles is around 1 μm (Sciacchitano and Scarano 2022).

5.7.5. Imaging system

The *LaVision sCMOS CLHS* camera is used, equipped with a double shutter interframe time of 120 ns, and a field of view (FOV) resolution of 2560 by 2160 pixels (LaVision 2020). To achieve the large field of view required for capturing both tandem object's wake simultaneously, a camera lens set with a focal length, $f = 35mm$ is used. Both the laser pulse rate and camera double shutter recording were set to 15Hz, while the separation time between two image pairs was set to $\delta t = 60\mu s$. This δt, observes the conservative yet popular quarter displacement rule, detailed by Keane and Adrian 1990, for an interrogation window of 32 by 32 pixels, ensuring sufficient capturing of particle displacement. Furthermore, it results in a roughly 10 pixel displacement for a freestream tracer particle between image pairs. With typical uncertainties for captured displacement being 0.1 pixels, as noted by Nobach and Bodenschatz 2009 and Adrian and Westerweel 2010, this minimises the effect of this error on displacement measurements.

In order to sufficiently track particles and prevent under sampling and peak locking of the diffraction-limited particle image diameter (d_τ) on the camera sensor, the (d_τ) must be adequately large. To keep peak locking to nominal levels, Adrian and Westerweel 2010 recommend that the particle image size be roughly 2-4 pixels. For this experiment campaign, to capture the flow interaction and wake of two tandem models, a large field of view size is required for the test configurations, with dimensions of 512mm by 432mm at XY-plane height $Z = 20mm$. This resulted in both the camera object distance and particle image diameter to be relatively large and insufficient tracking of each individual particle. This may be observed in Figure 5.7, where with a higher f-stop, although the particles are sampled by at least 2 pixels, an insufficient resolution for particle displacement tracking is evident. It must be noted that this problem is exacerbated by an incorrect seeding density. To accommodate for this sampling issue, the f-stop of the camera was set to $f_\# = 5.6$, resulting in $d_\tau = 7.5\mu m$. With the pixel size of the camera being $6.5\mu m$, this is below the recommendation of Adrian and Westerweel 2010, however is a sufficient compromise between sufficiently capturing each individual particle's displacement and minimising peak locking.

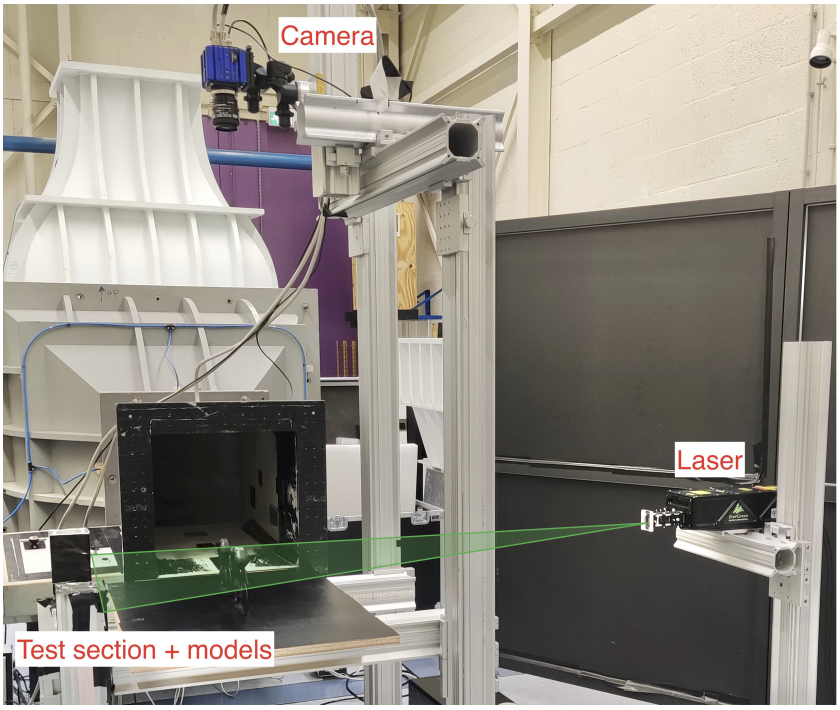

Figure 5.6: Test section of the wind tunnel for the PIV campaign with cyclist models

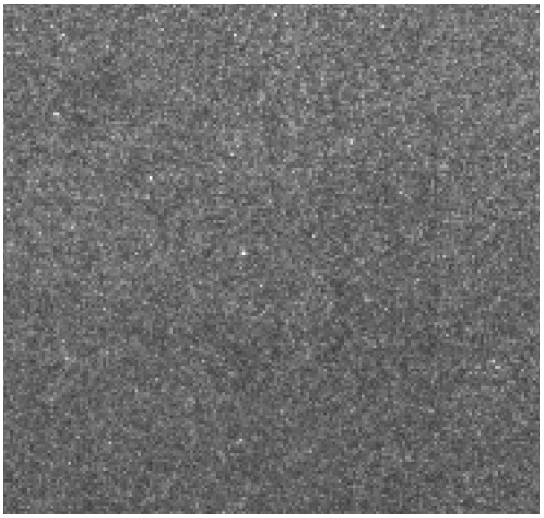

Figure 5.7: Raw image of tracer particles with insufficient seeding density and a camera f-stop setting of $f_{\#} = 11$ and $d_\tau = 14.74\mu m$

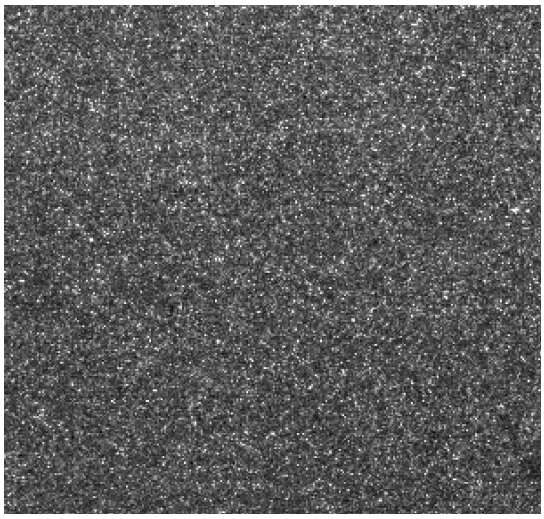

Figure 5.8: Raw image of tracer particles with correct seeding density and a camera f-stop setting of $f_{\#} = 5.6$ and $d_\tau = 7.5\mu m$

5.7.6. Z-Height Measurements

To capture 3D flow phenomena, with sufficient spatial resolution, a multi-planar 2D PIV method is used, with several X-Y planes at staggered Z-plane heights being captured. An overview of the Z-height planes captured are shown in Table 5.1, and additionally illustrated in Figure 5.9 and 5.10. It can be observed that the majority of both the cylinder and cyclist models are captured by the chosen XY-planes. However, no flow measurement close to the floor or near the tip of the cylinder or cyclist body height was performed, due to the presence of strong reflections causing unsatisfactory particle tracking and inaccurate velocity data to be captured.

Table 5.1: Allocation of Z-height measurement planes for both cylinder and cyclist models. Do note that x^* symbolises that at the higher Z-heights, only the $d/D = 1$ and $d/D = 1.2$ configurations are tested.

Z-Height [mm]	Cylinder		Cyclist	
	z / H	Measured	z / H	Measured
20	0.10	Yes	0.13	Yes
40	0.20	Yes	0.25	Yes
60	0.33	Yes	0.38	Yes
70	0.38	Yes	0.45	Yes
80	0.44	Yes	0.51	Yes
90	0.5	Yes	0.57	Yes
100	0.56	Yes	0.64	Yes
110	0.61	Yes	0.70	Yes
120	0.67	Yes	0.76	Yes
130	0.72	Yes	0.83	Yes
140	0.78	Yes	0.89	Yes
150	0.83	No	0.96	Yes
160	0.89	Yes	1.02	No
170	0.94	Yes*	1.08	No
190	1.06	Yes*	1.21	No

Due to testing time constraints, not every configuration is captured at each of the Z-planes. For example, above $Z = 150mm$, no measurement for the cyclist models were performed. This is due the flow characteristics around the upper back having lesser influence on the drag forces of the overall cyclist body, as noted by Crouch et al. 2014, and is therefore skipped. Furthermore, for the cylinder models, at the higher Z-height, namely $Z = 190mm$, only the $d/D = 1$ and $d/D = 1.2$ cylinders are tested, while only $d/D = 1.2$ configurations are tested at $Z = 190mm$. Notably, $Z = 180mm$ was avoided, as this height is equivalent to the height of the $d/D = 1$ cylinder and produced significant flow reflections. It can be noted in Figure 5.6, that the laser is set up on a mechanism which allows for translation in the Z-axis without rotation or shifting in the other axes.

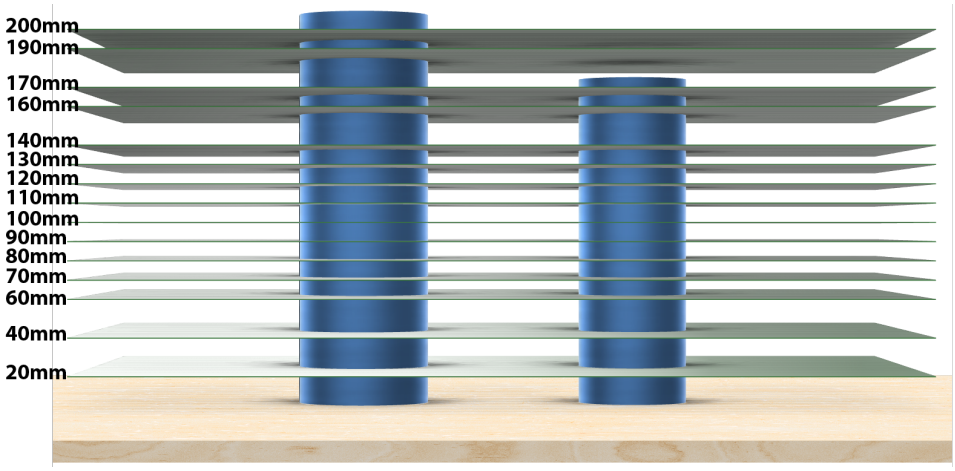

Figure 5.9: Z-plane heights used to capture flow around the cylinder models, shown relative to a leading $d/D = 1.2$ and downstream $d/D = 1$ cylinder model

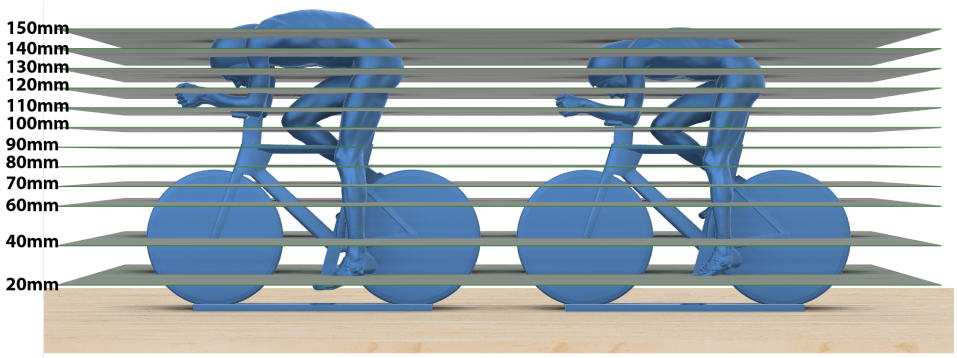

Figure 5.10: Z-plane heights used to capture flow around the cylinder models, shown relative to a leading $w/W = 1.1$ and downstream $w/W = 1$ cyclist model

5.7.7. Camera calibration

The experimental methodology involves setting the laser at specific Z-heights above the test plate. Using a calibration plate placed at this same Z-height, calibration of the camera's magnification and scaling parameters in *DaVis* are performed. Following the calibration, each PIV test configuration is tested in sucession. Once all test configurations have been tested at the specific Z-height plane, the laser height is shifted to the next required Z-height, and the calibration and test configuration measurement processes are repeated.

5.8. Boundary layer flow impact

Boundary layer flow tripping on the cylinder models themselves has already been discussed as an important factor in relating the results obtained in this experiment to those observed at higher Reynolds number situations, including professional cycling events. Additional tripping of the test section floor and ceiling in the force balance campaign has the potential of further increasing the thickness of the boundary layer. Unfortunately, for the force balance campaign, no boundary layer measurement was undertaken. However, for the PIV campaign, where no test section floor tripping was present, flow movement of the boundary layer was captured and vector statistics were calculated. From this analysis, it was found that at the x-position of the upstream model, the boundary layer reached 99% freestream velocity at roughly $z = 19mm$. With the height of the baseline $D = 60mm$ cylinder being $H = 180mm$, this gives a boundary layer to model ratio of $\delta/H = 0.11$ and $\delta/D = 0.32$. From this, it can be noted that the boundary layer has a rather minimal impact on the flow around the cylinder models. Additionally, the strength of the counter-rotating base vortices, observed by Essel et al. 2021, should have a lesser influence on the flow at lower Z-heights. Furthermore, despite a floor test section not being present (in still air) for a moving cyclist, the effect of the boundary layer flow around the cyclist models is also believed to be marginal. This is because the part of the cyclist models immersed within the boundary layer are the mounting plate and lower part of the wheels, which have little influence on the flow around the cyclist body. Therefore, the boundary layer is unlikely to affect the flow variation between the different size ratio and spacing configurations of tandem cylinders and cyclists.

6

Data reduction and processing

In this chapter, the data processing techniques for both the force balance and PIV campaigns are outlined, with the aim of explaining how the data presented in the results chapters is obtained. This includes the method for calculating the drag coefficient and drag reduction, as well the application of a blockage correction. For the PIV data, the photo post-processing and velocity calculation settings and methods are discussed. Additionally, the limitations of the experimental methodology is outlined.

6.1. Force balance data

6.1.1. Drag coefficient and drag reduction

The raw data directly obtained from the force balance is first subtracted by the wind-off "zero" force, before being averaged to obtain the ensemble time averaged drag force on each respective cylinder. As the atmospheric conditions of the wind tunnel are known, the uncorrected drag coefficient may then be calculated. For clarity, the frontal area of the cylinder and cyclist models in a tandem configuration is identical to its individual counterpart. The drag reduction, DR, is determined by normalising the tandem configuration drag coefficient against it's respective individual drag coefficient:

$$DR = \frac{C_{d,individual} - C_{d,tandem}}{C_{d,individual}} \times 100 \tag{6.1}$$

Additionally, as multiple test repeats are taken for each spacing and size ration configurations, both in the upstream and downstream measuring position, the standard error for each data point is also obtained. The standard error, SE, is defined as follows, where σ is the standard deviation and n is the collected number of samples:

$$SE = \frac{\sigma}{\sqrt{n}} \tag{6.2}$$

6.1.2. Blockage Corrections

With a model placed in a closed test section, the flow behaviour will naturally be dissimilar to that of an unbounded air stream case as the presence of walls around the model does not permit the transfer of normal velocity and constrains the flow. This effect, called solid blockage, can clearly be viewed in Figure 6.1 and Figure 6.2, where unlike in the free-air case, the tunnel flow is not able to expand and is constricted between the wall, the model and its wake. This reduces the flow area, and by observing Bernoulli's equation and the continuity equation, an increase in flow velocity must be experienced as it passes by the model region. This has the effect of increasing the measured drag coefficient of the model in a wind tunnel and should be corrected to accommodate for this effect. It should be noted that flow corrections for the PIV campaign's use of an open test sections is not performed. This is because flow visualisation is solely performed without drag determination. Additionally, open test section corrections are less well defined both in general cases and especially for cyclist models, while also being weaker in influence.

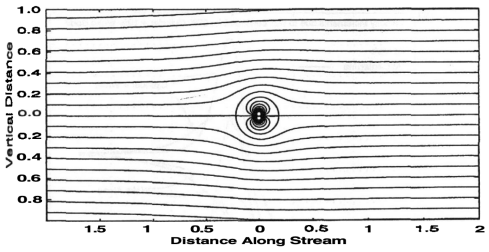

Figure 6.1: Streamlines for a cylinder and its wake in free air (Barlow et al. 1999)

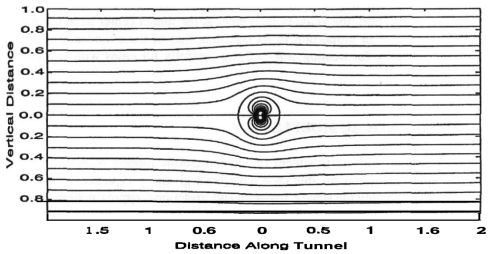

Figure 6.2: Streamlines for a cylinder and its wake in a constrained closed test section (Barlow et al. 1999)

For a bluff body, a wake will be generated that will have a lower than freestream velocity. In a closed test section tunnel, in order to observe the continuity equation, (similar to that of solid blockage) the flow outside of the wake must also be higher than freestream, as seen in Figure 6.3. This effect, called the wake blockage, will lower the pressure behind the model and maintain a conservation of momentum. It must additionally be corrected for when relating to free-air flow situations.

Corrections can be applied to the drag force coefficient on the cylinder models. It must be noted, however, that there is no empirical data for blockage corrections on cyclist bodies and these would be highly specific to body shapes. Therefore, no corrections are applied to measurements using cyclist models. There are several methods to apply blockage corrections to cylinders, namely the methods proposed by Glauert 1933, Allen and Vincenti 1944 and Maskell 1963. Research by Anthoine et al. 2009 found that no single correction method was most suitable to be applied to circular cylinders in all flow regimes. In the super-critical regime, the Glauert formula, as shown in Equation 6.3, with the modification by Modi and El-Sherbiny 1973 using the empirical factor, G = 0.6, provides the best results. Although testing of the models at $Re = 1.0 \times 10^5$ is at the fringes of the supercritical regime (Roshko 1993), with the usage of flow tripping it is adequate to assume the presence of this flow regime. The Glauert blockage correction is therefore applied to both cylinder models, which will accommodate for

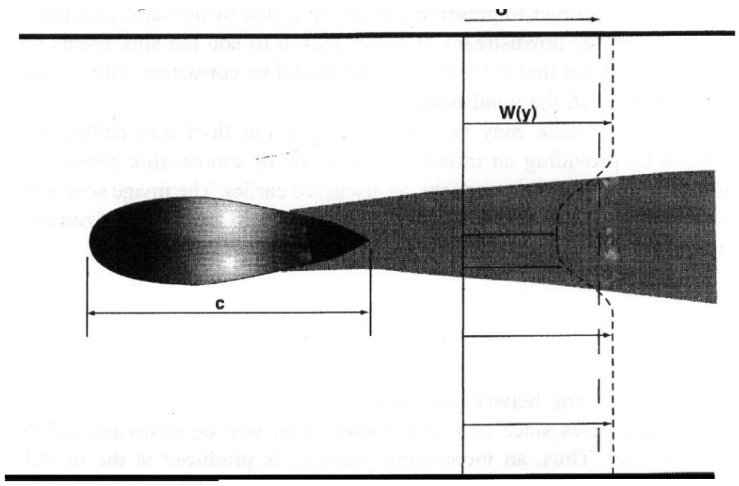

Figure 6.3: Blockage conditions in a close section (Barlow et al. 1999)

both solid blockage and wake blockage, and is defined as follows:

$$C_{d,c} = C_d \left(\frac{1 - GB_t}{1 + 0.822(B_t)^2} \right)^2 \tag{6.3}$$

where $C_{d,c}$ and C_d are the respective corrected and uncorrected drag coefficients, G is the aforementioned empirical factor and B_t is the total blockage ratio of the model in the test section. The blockage ratio is defined as the projected frontal area of the model relative to the average test section cross-sectional area. To avoid confusion, for two objects in tandem flow, the frontal area of the largest sized object is considered for the blockage correction equation.

6.2. PIV data

6.2.1. Image pre-processing

The inhomogeneous light components in the background of the images taken due to light reflections off the models and test section floor itself, have a detrimental effect on the particle tracking and correlation calculation. These areas are clearly visible in the raw image of Figure 6.4 (a). Therefore, these inhomogeneous components must be removed by image pre-processing methods prior to vector calculation. The first method constitutes obtaining the minimum image intensity for each pixel across a sliding filter length of 5 images pairs across all 200 image pairs and then subtracting this from the respective pixel for each of the individual images. As the tracer particles are moving and continuously in differing positions between images, while the background remains constant, a minimum subtraction will remove the background inhomogeneous components, while retaining the tracer particles. Observing Figure 6.4 (b), it can be noted that not all light reflections are necessarily removed, due to the variations in laser intensity between pulses causing differences in image intensity between images (Adrian and Westerweel 2010). This results in the minimum subtraction method being unsuitable for image sets where large amounts of flow reflections are present, such as with the cyclist models used in this study and for XY-planes at Z-heights near the base and tip of the cylinder models. However, due to the

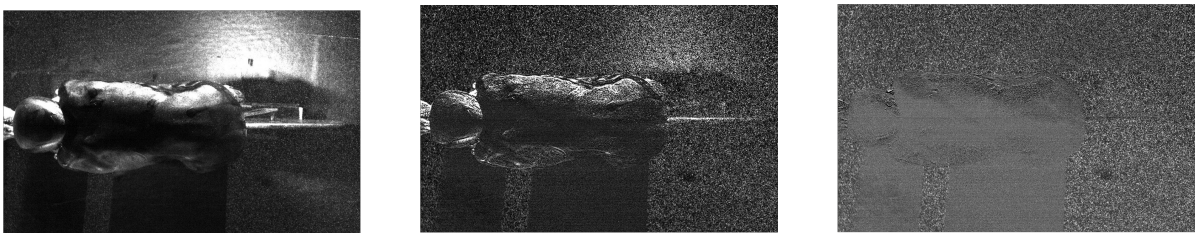

(a) Raw image **(b)** Minimum subtraction **(c)** Average quotient

Figure 6.4: Comparison of images taken in the XY-plane for the cyclist model

large amount of PIV data needed to be processed and the relative time efficient manner of this image pre-processing method, the minimum subtraction method is utilised for the majority of the XY-planes around the cylinder models.

An alternative image-preprocessing method for when large light reflections are present in the image set is also considered. First, the average image intensity across all 200 source image pairs is taken, which will generate an image that contains solely the stationary background and reflection regions, without any tracer particles. Dividing each of the source images by the average reduces the image intensity of the inhomogeneous background components, without effecting the tracer particle's image intensity. This therefore, not only removes background regions, but additionally any significant reflection that are present and increases the intensity of the tracer particles. This can clearly be observed in Figure 6.4 (c), and is used extensively for all images containing the cyclist models and the extremities of the cylinder models. Lastly, before performing vector calculations, masked regions are drawn around each of the test models to prevent the calculation of false velocity statistics in those regions. As both the perspective of the test section varied slightly between the various Z-height planes, individual masked region are needed to be drawn for each configuration. This results in slight variations in velocity components directly next to the model surface, however does not significantly impact vector data further away.

6.2.2. Post-processing methods

LaVision DaVis software is used to process and extract velocity field data from the processed images. Firstly, each image is sectioned off into smaller cells, referred to as interrogation windows and within each window a sufficient number of tracer particles must be captured. The auto-correlation function is used to compare the similarity between two image pairs. The peaks obtained from the correlation function indicate the average particle image displacement between image pairs, and due to the time separation between image pairs being known, the vector component for the interrogation window can be found. It should be noted that interpolation of the correlation peak at a sub-pixel level is also used to increase the accuracy of determining the peak position.

In this study, for the vector calculation, a decreasing size multi-pass method is implemented. This provides a solid, conservative foundation for an initial calculation that minimises the capturing of spurious vectors, which can then be followed by a more refined and increased resolution final calculation without increasing the risk of erroneous vectors. An initial 64 by 64 pixel interrogation window with a 50% overlap and 2 multi-passes is used for the initial calculation. It should be noted, that this is larger than the 32 by 32 pixel interrogation window that the image pair separation time was set up for. This is recommended by Raffel et al. 2018, because the pixel displacement uncertainty decreases with larger

interrogation windows, as a larger number of particle images are considered and the effect of correlation noise is reduced. The usage of multiple passes is used to acquire convergence for the vector data, while the overlap is desired as it increases the spatial resolution of the vector field. For the final calculation, a 24 by 24 pixel interrogation window with 3 multi-passes is implemented with a 75% overlap. The result of this chosen final interrogation window was reached upon through a compromise of sufficient number of particle images within an interrogation window, processing time and an acceptable signal-to-noise ratio for the vector data. Following recommendations from Willert and Gharib 1991, a circular Gaussian weighting is used in the particle displacement calculation for the sub-pixel peak position estimation, which allows for the smaller interrogation window sizes to be used. For vector post processing, the universal outlier detection method is used with similar recommendations as that covered by Westerweel and Scarano 2005. Within a filter region window of 7 by 7 pixels, a vector is deemed spurious and removed if the median residual is found to be greater than two standard deviations. Any empty spaces within the velocity field is filled in via interpolation, while smoothing of the vector is not considered.

In order to align each Z-plane measurement with each other, a homogeneous origin point and mesh grid must be applied to each vector field. The origin point is specified as the most downstream position of the baseline individually tested $d/D = 1$ cylinder model, equivalent to the $L/D = 2.5$ position when a downstream cylinder is additionally placed. An X-Y mesh grid is specified, with the 2D vector field data from each Z-plane interpolated onto the mesh grid. This ensures that interpolation between the Z-planes is possible and by combining the 2D vector fields, a 3D matrix is created.

6.2.3. Wake width and separation point calculation

The wake width and wake separation point can be numerically determined from the flow visualisation data behind both the cylinder and cyclist model and is illustrated in Figure 6.5. The wake width is taken at a half characteristic length downstream from the trailing edge of the object of interest. In the cylinder case, this is at $x = 30mm(x/D = 0.5)$ and for the cyclist case is at $x = 19.5mm(x/W = 0.5)$. The separation distance between the left and right $U/U_\infty = 0.50$ isoline shed from the object is defined as the wake width. The separation point is derived from the cylinder right side (as shown), due to it not being in a shadow region, and is defined as the point where the $U/U_\infty = 0.50$ isoline meets with the masked region. It must be strongly iterated that this is not indicative of the exact point of separation, due to cylinder boundary flow not being captured, however is suitable to describe macro-scale variations in wake shedding points. Lastly, it should be noted that the angle coordinate system for the cylinder models is defined by two symmetrical semi-circles, as pictured in Figure 6.5.

6.3. Limitations of the experimental method

The blockage correction defined in the previous section depends upon empirical data and is applied through the use of the Glauert factor, which is tuned towards infinite span cylinders. As there is no existing correction for truncated cylinders, the corrections applied are not known to be completely accurate. However, the effect that solid and wake blockage has on the tested models is deemed to be more considerable than the unknown effect of the corrections and therefore is applied. Additionally, no buoyancy corrections are available for truncated cylinders or cyclist models, and as the effect of buoyancy is believed to minimal, no buoyancy corrections are applied.

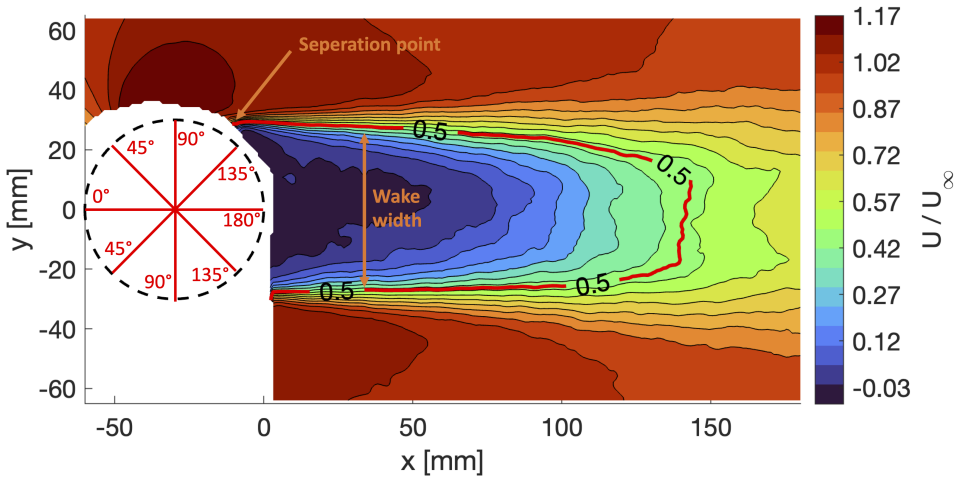

Figure 6.5: Diagram of the streamwise velocity component in the XY plane behind an individual cylinder, showing the definition for the wake width and separation point used in this report

It must be noted that for the cyclist model, designing the two solid disk wheels for ease of manufacturing, does not mimic realistic conditions. In time trial competitions, the usage of a front disc wheel is outlawed, while in road stages neither a rear disc wheel is permitted. The effect that this wheel design will have on the overall drag area of the cyclist is unknown, however as the main investigation constitutes around the differences in cyclist body size and the bike frame size remains constant, it is not deemed to have considerable negative consequences on results. Another effect to be considered is the inability of the wheels to rotate and the effect this has on the drag forces of the cyclist body. Although CFD experimentation by Malizia et al. 2021 found a roughly 7% reduction in drag area for a rotating wheel in a time trial cyclist configuration compared with a static wheel, this effect was very small when analysing the cyclist body drag area, at roughly 0.5%. Not only is this effect therefore inconsiderable for the investigation, but also is within the uncertainty range of the computational methods used.

For the PIV experiments, although a relatively high resolution is available in the X-Y planes, a limited resolution is available in the Z-dimension. This results in a significant limitation, where any flow structure smaller than the minimum Z-plane gap distance of 10mm cannot be fully captured. Additionally, the inability to capture the vertical velocity component, w, results in the dominant counter-rotating shed vortices from both the cylinder and cyclist cases not to be directly captured. Alongside this, as the flow cases experimented are three dimensional, the inability of measuring the out-of-component displacement will lead to increased errors in the in-plane component measurements (perspective error), as noted by Adrian and Westerweel 2010.

Furthermore, alignment of each plane is extremely difficult and several uncertainties must be considered. Firstly, despite a uniform origin point and constant mesh grid being defined for each Z-plane, slight variations in model positioning can still occur, resulting in potential misaligned vector data between Z-planes close to the model. Additionally, due the presence of two models, the camera cannot be positioned directly overhead from both models simultaneously, causing certain sections of the model at lower Z-heights to be obscured by the height of the model. This can be observed in Figure 6.6, where when focusing on the upstream cylinder, at $Z = 20mm$ the leading edge is obscured, however the trailing edge is clear. Meanwhile the inverse is true at $Z = 170mm$. Therefore, it follows that as the Z-height varies, the amount of visible flow close to the model also varies.

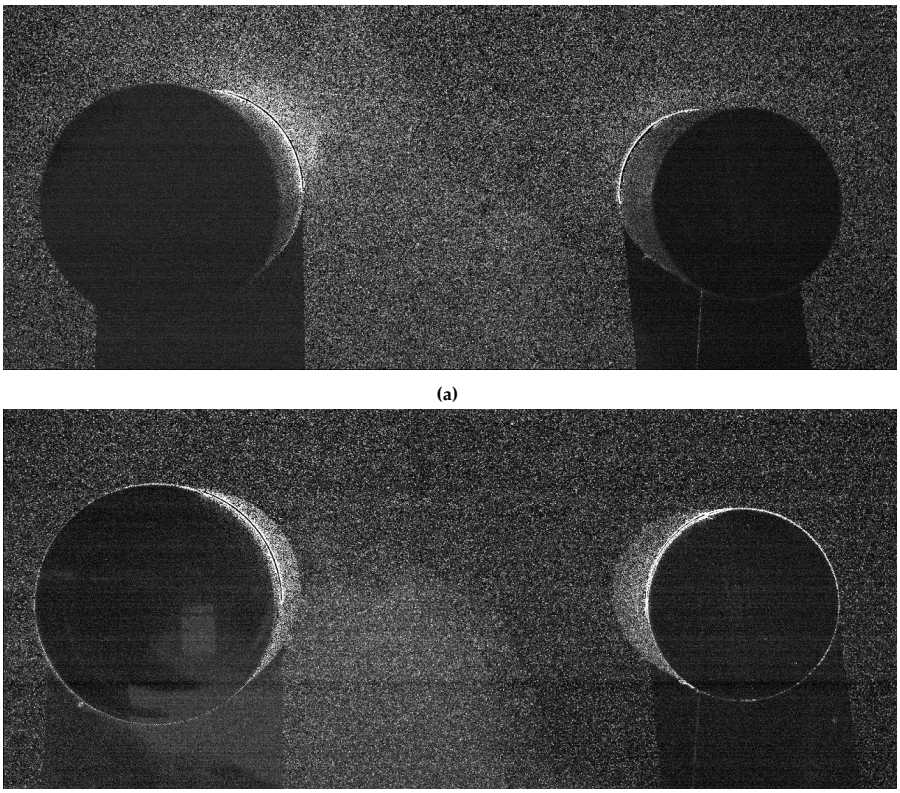

(a)

(b)

Figure 6.6: Light saturation edited images of the $d/D = 1.2$ in $L/D = 3$ configuration at (a) XY Plane $Z = 20mm$ and (b) XY Plane $Z = 170mm$

7

Results and Discussions: Finite cylinders in tandem

In this chapter, the results for the cylinder models are discussed and analysed. Firstly, the individual cylinder case is presented, before independently analysing the variation in drag reduction and flow structures for both the upstream cylinder and downstream cylinder. Further, the group drag reduction for tandem cylinders is covered.

7.1. Individual cylinder

7.1.1. Drag forces

In Table 7.1, the drag forces measured for the individual cylinders in this study is compared with those from literature. When analysing an isolated cylinder, the measured drag forces are higher for an infinite cylinder compared with that of its truncated counterpart, as may be observed in Table 7.1. This reduction in drag coefficient mimics observations by Kim and Christensen 2018 and Sumner and Reitenbach 2019. However, unlike these two studies, in this research the three-dimensional flow effects appear to have a lesser impact on drag forces, with a comparatively small 5% variation in drag coefficient being recorded between the infinite and truncated configuration cases. The reasoning behind this disparity with literature may be understood when examining the experimental methods for each of the studies.

Table 7.1: Drag coefficients for individual cylinders measured in the force balance campaign.

	Model	Re	d / D	AR	Cd
Infinite Cylinder	**Present study (d = 60 mm)**	1.2×10^5	0.317	∞	0.55
	Alam et al. 2003b	5.5×10^4	0.005	∞	1.12
	Alam and Zhou 2007	4.3×10^4	Not given	∞	1.11
	Timmer and Veldhuis 2021	1.1×10^5	Not given	∞	0.60
Truncated Cylinder	**Present study, d = 48mm** $(d/D = 0.8)$	0.97×10^5	0.396	3	0.51
	Present study, d = 54mm $(d/D = 0.9)$	1.1×10^5	0.352	3	0.50
	Present study, d = 60mm $(d/D = 1.0)$	1.2×10^5	0.317	3	0.48
	Present study, d = 66mm $(d/D = 1.1)$	1.3×10^5	0.288	3	0.47
	Present study, d = 72mm $(d/D = 1.2)$	1.5×10^5	0.264	3	0.46
	Wieselsberger 1921	8.8×10^4	Not given	3	0.74
	Okamoto and Yagita 1973	1.3×10^4	0.150	3	0.75
	Sumner et al. 2004	6.0×10^4	2.60	3	0.61

For the infinite cylinder, the studies by Alam et al. 2003b and Alam and Zhou 2007 conducted at slightly lower Reynolds numbers, observed significantly higher drag coefficient values, above $C_d = 1.0$, compared with $C_d = 0.55$ from the present study. This is due to the presence of zigzag strips being used in this study, both at the $\theta = 60°$ leading edge of the cylinder and upstream floor section for the experimented case, delaying the boundary layer separation and creating a smaller wake than that observed by Alam et al. 2003b and Alam and Zhou 2007. Meanwhile, Timmer and Veldhuis 2021 conducted a similar experiment with tripping, with slightly thicker zigzag tape at $\theta = 45°$, resulting in an observed drag coefficient similar to that measured in this experiment, showing good agreement with the force balance data collected.

For the truncated cylinder, using the baseline $d = 60mm, (d/D = 1.0)$ model, a similar situation arises where a measured drag coefficient of $Cd = 0.48$ is a noticeably smaller drag coefficient than that found in literature, which cannot be explained purely by variations in Reynolds number, but again by the presence of flow tripping. The smaller difference in drag coefficients between the infinite and truncated cases can largely be a result of the presence of zigzag strips unequally altering the flow structures between the two cases. For the infinite cylinder, a flow case with limited 3D flow effects, increasing the turbulence intensity from flow tripping will increase the amount of flow mixing between streamlines, which is inherently a 3D flow effect that is not present or as strong in non-tripped cases. Meanwhile, 3D flow structures already exist for truncated cylinders, with the presence and effect of the tip vortices having already been previously discussed, causing 3D flow mixing. Therefore, flow tripping in these cases will still reduce the wake size through delayed boundary layer separation from the sides of the truncated cylinder, however 3D flow mixing will not increase as much compared with that of the infinite cylinder case. This explains the increased similarity in drag coefficient between the truncated and infinite cylinder configuration when flow tripping is used.

7.1.2. Velocity data

The variation in flow structures with Z-height of the cylinder can be observed through the PIV flow visualisation experiment. In Figure 7.1, the velocity profile for the isolated cylinder configuration is shown at several Z-heights, including near the fixed end, the centre line and near the free end. Observing Figure 7.1, near the fixed end, but above the boundary layer, at $z/H = 0.22$, a large low velocity region

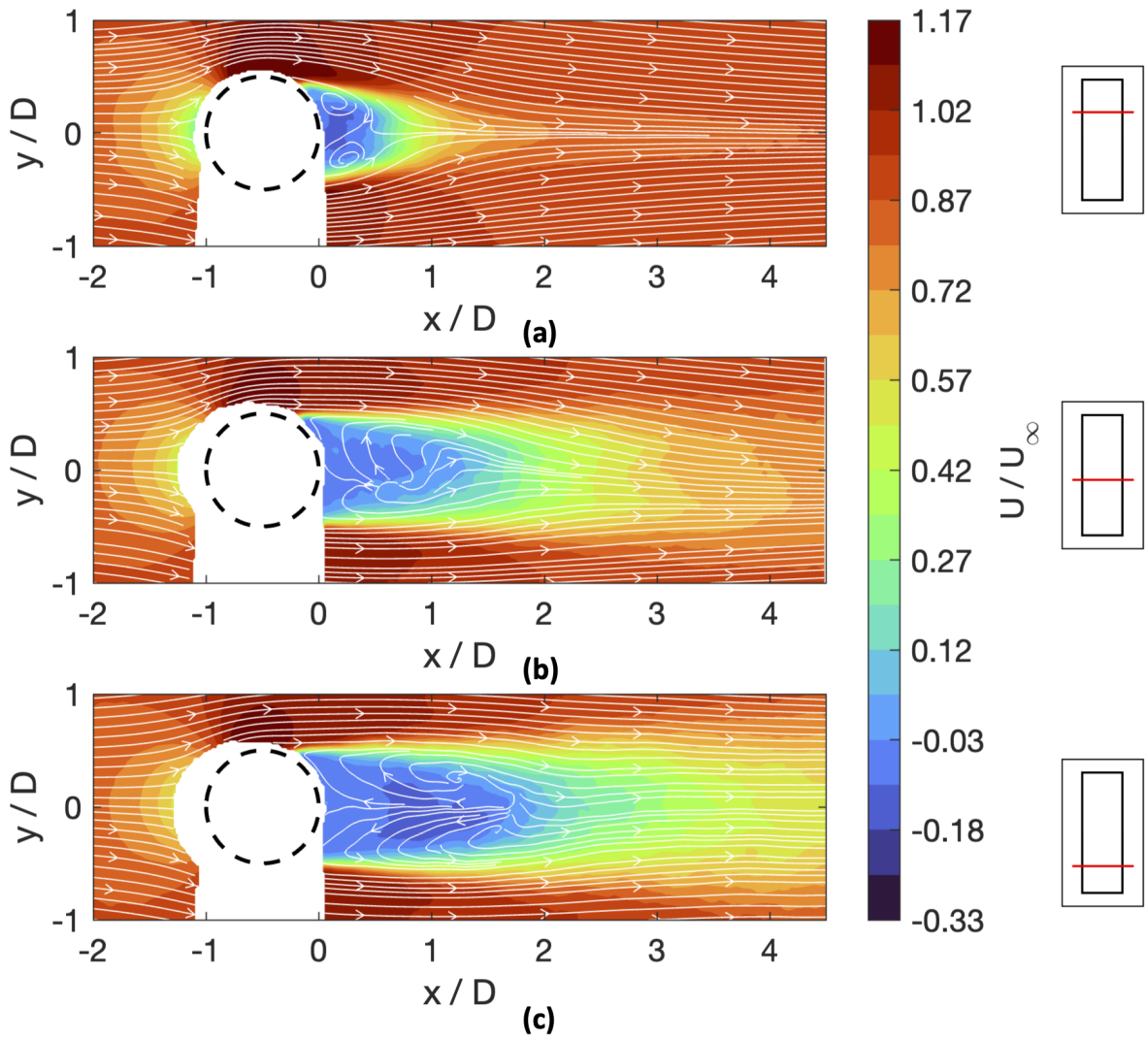

Figure 7.1: Contour plots of x-component velocity behind an isolated cylinder at heights (a) $z/H = 0.78$, (b) $z/H = 0.50$, (c) $z/H = 0.22$

of stagnant flow is captured behind the cylinder, indicating a re-circulation region of flow with negative streamwise velocity. Furthermore, the length of the wake is noted to be relatively long compared to those at the higher Z-heights, agreeing with the observation made by Luo et al. 1996, noting that longer wake formation lengths appear at the base of finite cylinder. Furthermore, the location of the shed shear layers, which indicates the position of the boundary layer separation, is found around $\theta = 115°$ at $z/H = 0.22$. Interestingly, near the free end of the cylinder at $z/H = 0.78$, similar to that noted by Essel et al. 2021, the boundary layer separation point can be observed to be slightly further downstream due to the close proximity of the tip vortices. The extent of the downwash on the truncated cylinder is illustrated when observing the differing wake lengths at the higher Z-heights. At the cylinder mid-height, $z/H = 0.50$, a comparatively smaller wake is observed, despite the position of the shed shear layer remaining constant, indicating that the downwash tendency of the wake is transporting flow away from the upper Z-heights. Near the free end at $z/H = 0.78$, a very short wake formation length is apparent and a near full wake recovery occurs at $x/D = 2$ behind the cylinder at the upper height. Although in general, a low momentum region does not necessarily correlate with a drag force,

Terra et al. 2017 notes that in the wake of an object, where flow separation occurs, near the object, a trailing edge low momentum region typically corresponds with an equally significant pressure force. At the upper Z-heights, a negative streamwise velocity region is located directly behind the cylinder trailing edge, indicating that the local drag coefficient for the cylinder increases when the wake length decreases. Luo et al. 1996 commented that at the free-end, the counter-rotating vortices are closer to the cylinder surface and due their low pressure characteristics, this results in a wake pressure drop at the free-end, causing a small vortex formation length and also a higher local drag coefficient.

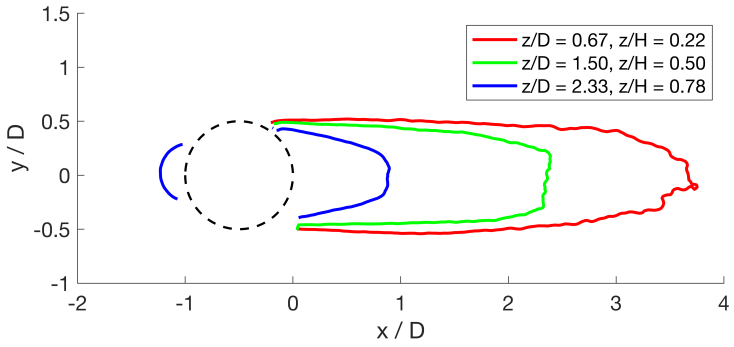

Figure 7.2: Isoline in the X-Y plane of $U/U_\infty = 0.50$ comparing the wake size at different heights behind an isolated cylinder

To highlight the variation in wake size observed above, single contour lines of $U_x/U_\infty = 0.50$ at three Z-heights shown earlier are superimposed on each other in Figure 7.2. It is illustrated that, similar to observations noted by Essel et al. 2021 for cylinders with relatively small aspect ratios, the shear layer shedding point remains relatively constant (apart from near the base and free end), resulting in a similar wake width immediately downstream of the cylinder between all three heights, however, the length of the wake varies significantly. It can be observed that the wake formation length of the cylinder varies considerably across the height and decreases in length with increasing Z-height. This is due to the trailing vortices at the free-end bringing freestream flow into the wake, causing a downward movement of wake flow, as described by Luo et al. 1996 and Sumner and Reitenbach 2019. This downstream movement of flow will increase the vortex formation length of the cylinder down the cylinder height, and results in an increased wake pressure and an associated lower local drag coefficient. This described variation in vortex formation length can clearly be observed in Figure 7.1 (b) and (c) and the effect it has on the velocity profile close to the cylinder surface. By plotting the full velocity profile of the near wake behind the downstream cylinder in the YZ-plane (Figure 7.3), the variation in drag forces can be better reported. At the free-end, the low momentum region is observed to cover 25% of the entire cylinder height. This is assosciated with a region of high local drag coefficient and is equally observed by Luo et al. 1996 near the free-end heights. Interestingly, between $0.1 < z/H < 0.75$, the velocity profile remains similar in magnitude, with a small peak being observed at $z/H = 0.40$. It is hypothesised that these are due to the presence of a re-circulation region in the Z-axis existing at the lower heights, similar to that observed by Essel et al. 2021. Near the base, the flow around the cylinder interacts with the boundary layer, forming a pair of base vortices inducing a weak upwash. It is possible that the interaction between the base vortices and tip vortices occurs at at $z/H = 0.4$, inducing a streamwise flow movement. However, it should be noted that as the z-component velocity is not captured in this study, it is not possible to be certain of this hypothesis. The downwash phenomena is highlighted in a more qualitative sense in Figure 7.4, where an isosurface of $U_x/U_\infty = 0.50$ for the entire wake is displayed. The wake growth down the cylinder height is clearly portrayed, showing a non-uniform low velocity region behind a truncated cylinder.

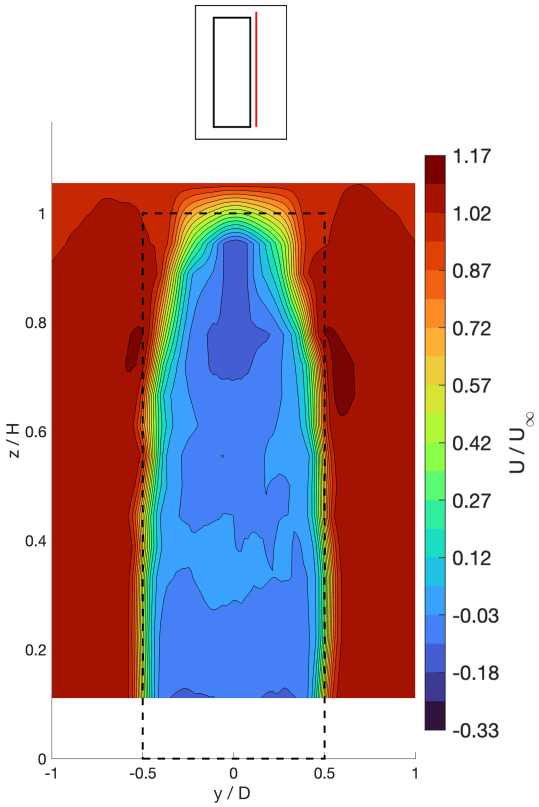

Figure 7.3: X-component velocity profile immediately behind the individual truncated cylinder

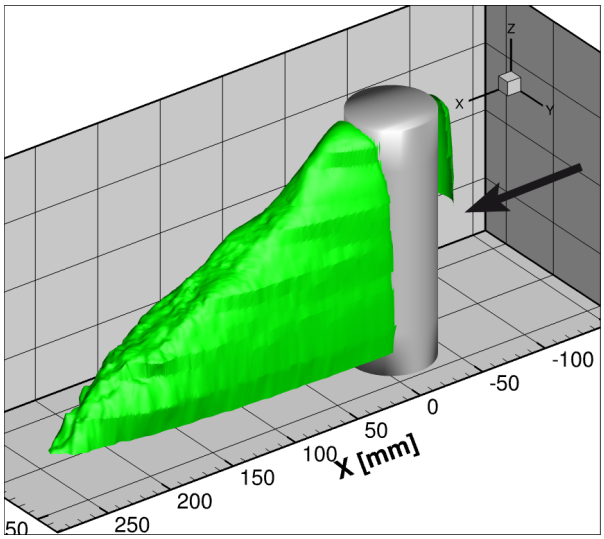

Figure 7.4: Isosurface of $U/U_\infty = 0.50$ around an isolated cylinder

7.2. Upstream cylinder

7.2.1. Drag forces

When a cylinder is placed in tandem behind another, the drag forces on the upstream cylinder are found to vary, altering the drag coefficient, $C_{d,up}$. In Figure 7.5, the variation in drag forces for the upstream cylinder appear to follow a non-uniform relationship with tandem spacing, especially for the smaller sized cylinders, $d/D = 0.8$ and $d/D = 0.9$. For these two cylinders, initially a reduction in $C_{d,up}$ occurs with L/D, reaching a minimum value at $L/D = 2.5$ and $L/D = 3.0$ respectively. This behaviour is followed by a measurable increase in $C_{d,up}$ with L/D. A minimum $C_{d,up}$ is also observed for the $d/D = 1$ configuration, however its prominence is far more subtle, with a only a slight increase in $C_{d,up}$ with larger spacings being recorded. It may be noted that comparing these results to that obtained by Sumner and Reitenbach 2019 for equally sized truncated cylinders of $AR = 3$ in tandem, the drag coefficients in this study are measurably lower (due to the aforementioned flow tripping and Reynolds effects), however the behaviour with spacing is similar. Sumner and Reitenbach 2019 observed a minimum $C_{d,up}$ around $L/D = 2.25$ for their $d/D = 1$ configuration, before slightly increasing afterwards for larger spacing, which this study's results mimic, however at a slightly higher spacing. An additional observation is that for the larger sized cylinders, $d/D = 1.1$ and $d/D = 1.2$, no minimum $C_{d,up}$ is found, with the drag coefficient continuing to decrease with L/D.

In Figure 7.5, evaluating just the drag coefficient can be misleading, especially when analysing size effects, where differences in drag forces between configurations can be undervalued ($2.0 < L/D < 2.5$)

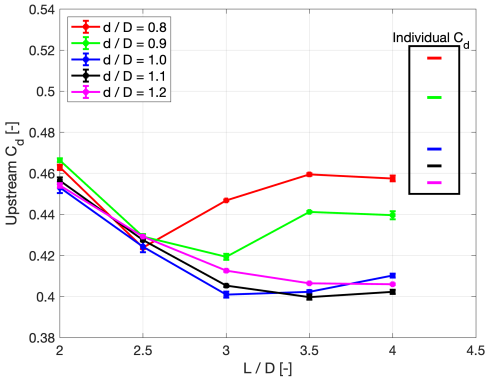

Figure 7.5: Drag coefficient variation with tandem spacing for the upstream cylinder

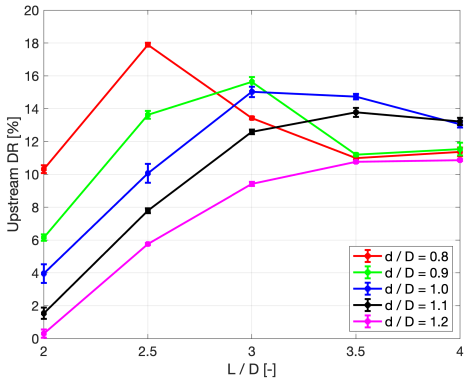

Figure 7.6: Drag reduction variation with tandem spacing for the upstream cylinder. The drag forces are normalised by each upstream cylinder's individual C_d.

or exaggerated ($3.0 < L/D < 4.0$). These differences can be properly observed by normalising each of the measured drag forces into drag reductions, DR, relative to each cylinder's respective individual drag coefficient. This is calculated as follows:

$$DR = \frac{C_{d,individual} - C_{d,up}}{C_{d,individual}} \times 100 \tag{7.1}$$

The variation in drag reduction for each cylinder configuration is plotted in Figure 7.6. Interestingly, between ($2.0 < L/D < 2.5$), a clear divide between the different sized cylinders is observed, where the smaller sized upstream cylinders experience the largest drag reductions. At $L/D = 2.5$, the smallest $d/D = 0.8$ upstream cylinder, reaches a peak in drag reduction of around 18%, which mimics results from Alam and Zhou 2007. Furthermore, it is evident that the slightly larger upstream cylinders of $d/D = 0.9$ and $d/D = 1.0$ reach their maximum drag reductions at the next measured spacing of $L/D = 3.0$. This suggests that changes in the flow regime are occurring between the various spacing and size ratio configurations and are causing notable variations in drag reduction. These observations hence indicate significant interaction between both spacing and size effects, and notable influences on drag reduction. Interestingly, it appears that the prominence of the drag reduction peak is reduced for the larger sized upstream cylinder and is absent entirely for the largest $d/D = 1.2$ configuration within the tested spacing range. Beyond $L/D > 2.5$, the relationship between size ratio, spacing and drag reduction begins to blur, with noticeable intertwining in DR_{up} between configurations. Peculiarly, at $L/D = 3.5$ the drag reduction for the largest and smallest tested cylinders, $d/D = 0.8$ and $d/D = 1.2$, are indistinguishable. It is therefore clear that for the upstream cylinder, the nature of the downstream cylinder has a relevant impact on the flow structure interaction between two tandem cylinders and influences the upstream cylinder's drag forces.

7.2.2. Velocity data

In Figure 7.7, several X-Y plane contour plots at differing Z-heights are shown for the $d/D = 1$, $L/D = 3$ tandem configuration. The largest discrepancy between the wake for the tandem configuration and that of the isolated cylinder is that the presence of the downstream cylinder in the wake causes an expansion

of the upstream cylinder's wake and it's width to be larger. Meanwhile at the lower Z-heights, there is a removal of the flow re-circulation area around $x/D = 1$ and a larger flow expansion occurring near the downstream cylinder, due to its stagnation point. However, similar to the individual flow case, the wake can be observed to decrease in size with increasing Z-height, due to the free-end tip vortices and induced downwash phenomena still occurring. This variation in wake width has several impacts on the drag forces experienced by the upstream cylinder. At the bottom of the cylinder, it can be observed that the wake fully envelopes the downstream cylinder, creating a continuous region of stagnant flow between the cylinders and is synonymous to extended-body regime. Meanwhile at $z/H = 0.50$, the flow is now observed to attach onto the downstream cylinder, suggestion a flow regime change to the re-attachment regime. Lastly, at $z/H = 0.78$, the flow regime has changed yet again, and the free end of the cylinders exist within the co-shedding regime.

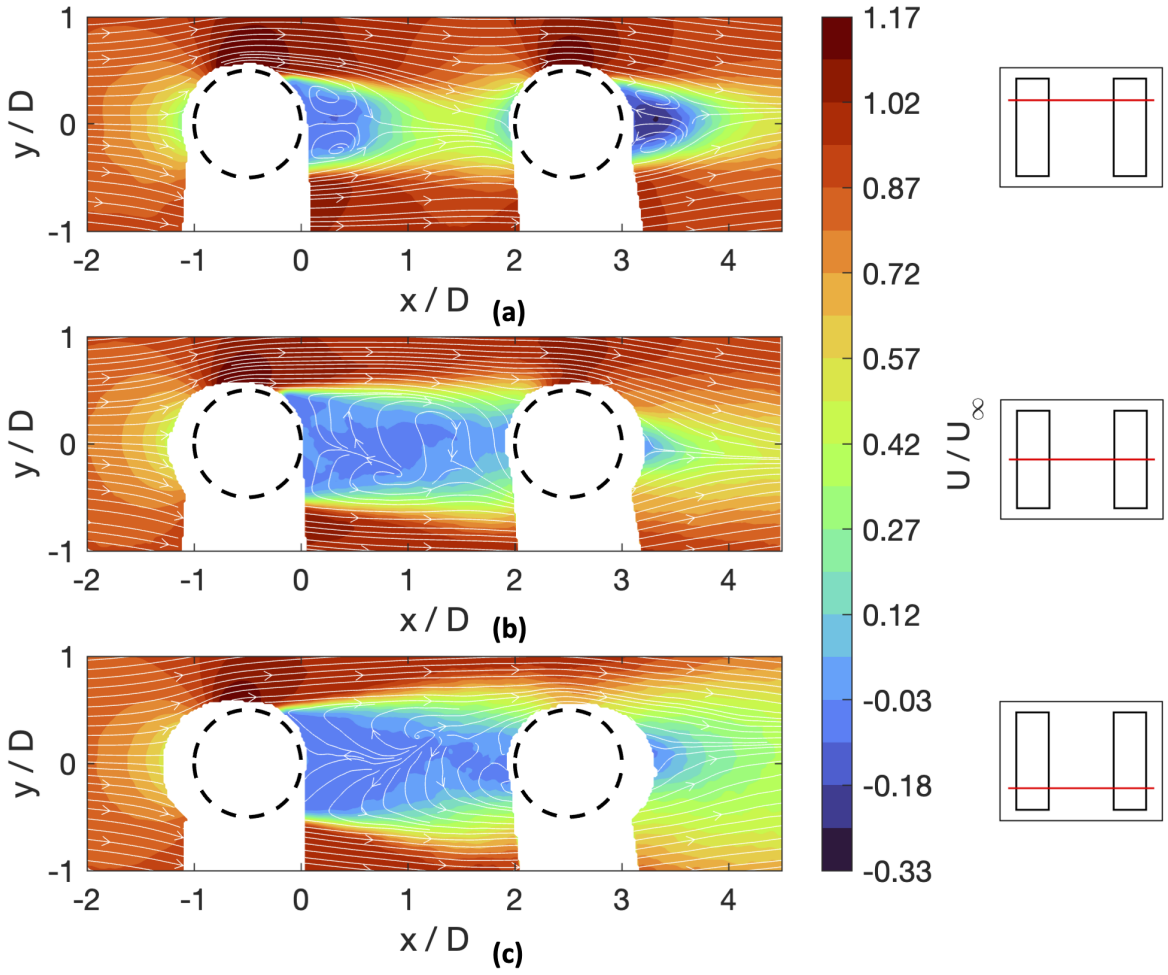

Figure 7.7: Contour plots of x-component velocity for two tandem cylinders in a $d/D = 1$, $L/D = 3$ configuration at heights (a) $z/H = 0.78$, (b) $z/H = 0.50$, (c) $z/D = 0.22$.

In Figure 7.8, several X-Y planes are plotted at the mid-height $Z/H = 0.50$, comparing the wake width between different size ratio configuration at $L/D = 3$ and that of the individual cylinder case. For the $d/D = 1$ configuration, the direct effect that a tandem downstream cylinder has on the upstream cylinder can be observed, where compared with individual case, the wake between the two cylinders is noticeably wider. This is largely due to the downstream cylinder's leading edge creating a high pressure region which expands the wake. Furthermore, as expected when a larger or smaller cylinder is placed

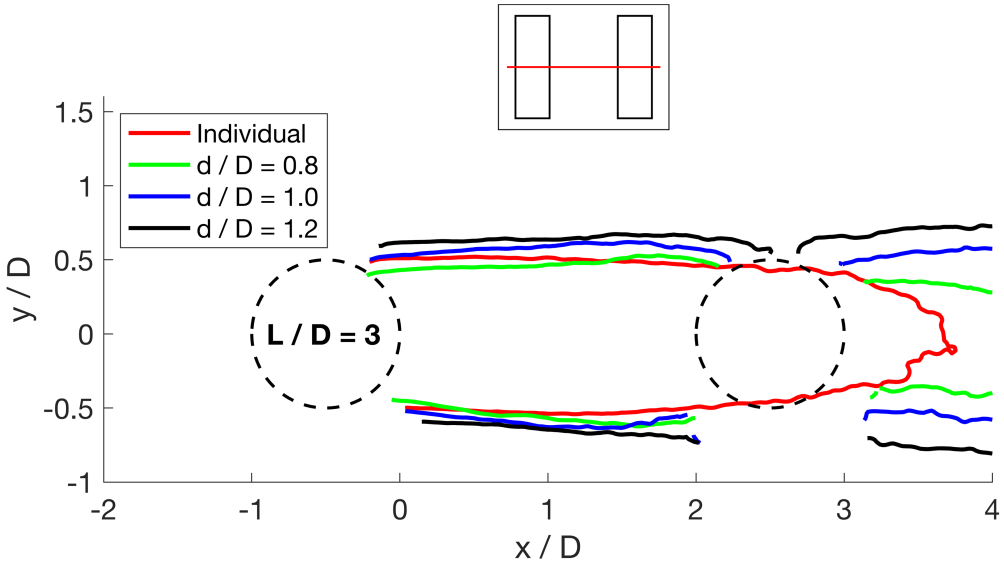

Figure 7.8: X-component velocity isoline in the X-Y plane at $z/H = 0.50$ of $U/U_\infty = 0.50$ comparing the wake size for different size ratio configurations for a spacing of $L/D = 3.0$

upstream, the wake width is is correspondingly larger or smaller. This is intuitive, as a larger object will have a bigger cross section and therefore will create bigger wake. However, a bigger wake will be influenced to a lesser extent by the high pressure region. Furthermore, due to the increased sheltering of the downstream cylinder by a larger upstream cylinder, the high pressure region will be reduced in magnitude, further lowering its influence. Both of these effects are visible in Figure 7.8 and explain for the drag reductions noted in Figure 7.6 at $L/D = 3.0$. It should also be noted that the larger cylinders are also higher in height and therefore immerse the downstream cylinder within its wake for higher Z-heights. Most notably, it can deduced that for the $d/D = 1.2$ case, at $z/H = 0.50$, the cylinders are still in the extended-body regime, due to the wake fully enclosing the downstream cylinder. In Figure 7.9, the wake width variation is shown and illustrates clearly the extent of the wake expansion. Even when a smaller upstream cylinder is used, namely the $d/D = 0.8$ case, the wake is still wider than that of the individual configuration.

From Figure 7.9, it can be noted that for each tandem configuration a larger wake width is measured at $L/D = 3.0$ compared with $L/D = 2.5$ at $z/H = 0.50$ for all size ratio configurations. When analysing the drag reduction's relationship with the spacing, it is observed that between $L/D = 2.5$ and $L/D = 3.0$, the drag reduction was found to increase and decrease to similar levels relative to the $d/D = 1.0$ baseline case, for both the larger and smaller size ratio configurations. Analysing the XY-plane velocity contour plot comparison between the two spacing configurations in Figure 7.10, it is possible to understand this phenomena. When the spacing is increased, it is found that the flow velocity between the two cylinders increases in magnitude, due to the higher level of energy mixing into the wake by the freestream. This causes the incoming flow for the downstream cylinder to be higher than that for closer spacing configurations, resulting in a stronger high pressure region. The effect of having a more substantial high pressure region will influence the pressure region of the upstream cylinder to a greater extent, reducing the upstream cylinder's drag force. This is the flow characteristic that is occurring for the larger size ratio configurations. Meanwhile, for the $d/D = 0.8$ case, due to the smaller nature of the of the upstream cylinder, this maximum high pressure region occurs around $L/D = 2.5$. It should be noted, that at small spacings, the flow velocity between the two cylinders can be relatively low, similar to that of the

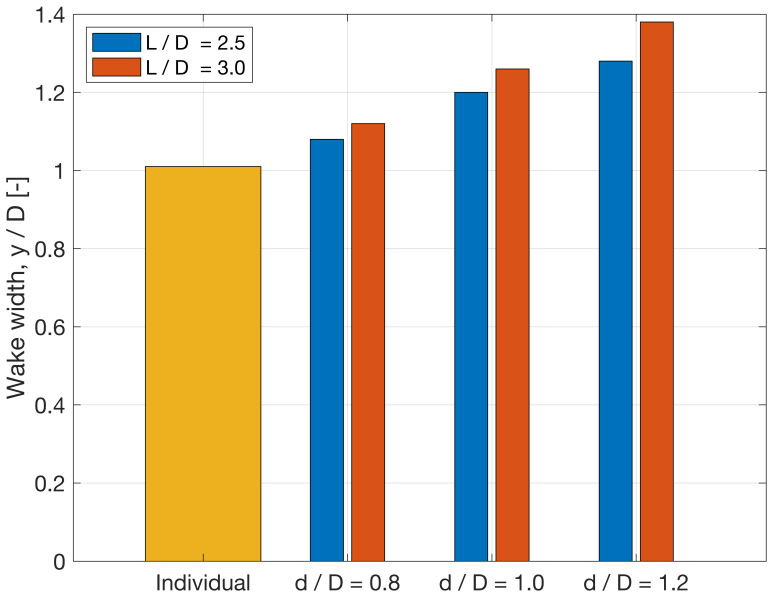

Figure 7.9: Wake width comparison for x-component velocity isoline $U/U_\infty = 0.50$ at $z/H = 0.5$

extended body regime, while at larger spacings, the influence of the downstream cylinder's stagnation point is reduced due to the increased distance. This change in flow regime occurs at different spacings for each of the size ratio configurations, and to differing extents, explaining the large fluctuations in drag reductions measured. For the $d/D = 0.9$ and $d/D = 1.0$, this optimal compromise between wake velocity and distance to the downstream stagnation region occurs around $L/D = 3.0$ and around $L/D = 3.5$ for $d/D = 1.1$ case. Furthermore, the absence of the drag reduction peak for the larger size ratio upstream cylinders can be related to their optimal locations being at a higher spacing.

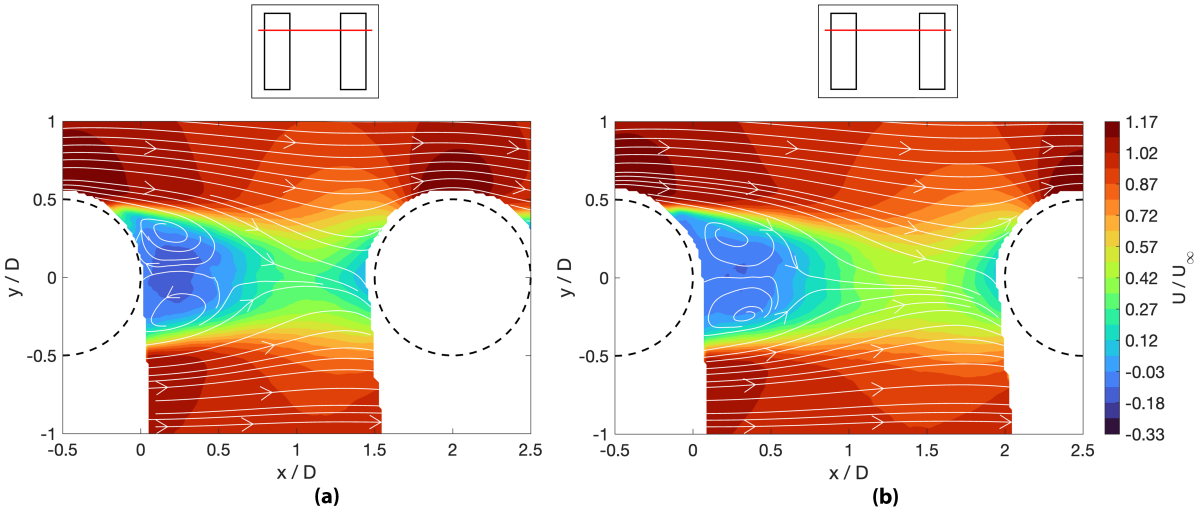

Figure 7.10: Velocity contour lines of x-component velocity in between two tandem cylinders in the X-Y plane at $z/H = 0.78$ for the $d/D = 1$ size ratio configuration at spacing (a) $L/D = 2.5$ and (b) $L/D = 3.0$

7.3. Downstream cylinder

7.3.1. Drag forces

The behaviour of the aerodynamic forces on the downstream cylinder is relatively more predictable and correlated compared with those on the upstream cylinder. Analysing Figure 7.11 this is clearly the case, where especially for the configurations with larger size ratios, a decreasing d/D results in an increasing $C_{d,down}$. Meanwhile, $C_{d,down}$ increased with increasing L/D. Of note though, is that for the smaller size ratio cases of $d/D = 0.8$ and $d/D = 0.9$, a small variation in drag coefficient with L/D is measured, with the inclusion of slight fluctuations, particularly for the $d/D = 0.9$ configuration at $L/D = 3.0$. As the downstream cylinder remained constant during the experiments, converting the drag coefficients into drag reduction is normalised with the identical individual drag coefficient for each configuration, resulting in a simple inverse graph, as shown in Figure 7.12. From this plot, a similar observation is made that the drag reduction is heavily influenced by the size and spacing ratios, with a notably larger range in drag reductions being presenced compared with the upstream cylinder.

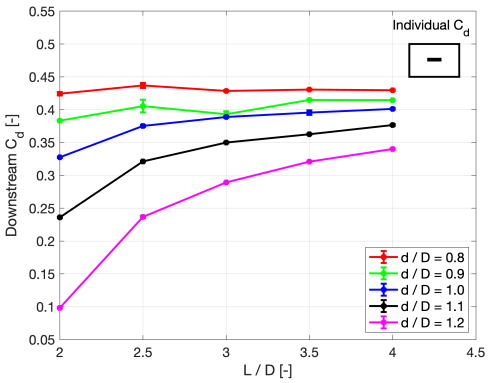

Figure 7.11: Drag coefficient variation with tandem spacing for the downstream cylinder

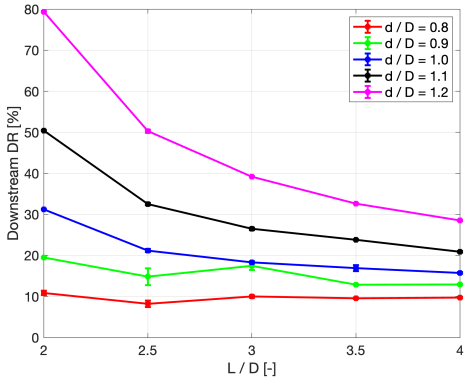

Figure 7.12: Drag reduction variation with tandem spacing for the downstream cylinder. The drag forces are normalised by the downstream cylinder's ($d/D = 1.0$) individual C_d.

An interesting observation is that a large variation in drag reduction occurs between $2.0 < L/D < 2.5$ for each of the tested size ratios, before beginning to taper off with increasing spacing. It appears that the larger size ratio cases maintain a negative curve gradient between drag reduction and spacing, while for the smaller size ratios cases, a flatter curve and even slightly positive gradient for the $d/D = 0.8$ configuration is evident. Furthermore, another peculiarity to occur at the smaller size ratios is that the drag reduction for $d/D = 0.9$ and $d/D = 1.0$ configurations at $L/D = 3.0$ is measured to be near identical, suggesting a potential change in flow condition for the $d/D = 0.9$ case causing a moderate change in drag forces for the downstream cylinder. Another observation is that, particularly at the smaller spacings, the drag reduction differences between the various size ratio configurations is significant and varies between cases. At $L/D = 2.0$, a 30% variation between the $d/D = 1.2$ and $d/D = 1.1$ cases is noted, meanwhile between the $d/D = 0.9$ and $d/D = 0.8$ cases, this difference is only 10%. This non-proportionality in drag force differences with various size ratios suggests that it is not just merely a variation in incoming wake width and velocity that is causing the changes in drag reduction between configurations, but also a flow phenomena that is occurring on the downstream edge of the trailing cylinder. When analysing the upstream cylinder earlier, it was clear that at the close spacings, for the $d/D = 1.2$ case, the two cylinders where still in the extended body regime. It is possible that the large

drop in drag reduction for this size ratio configuration between $L/D = 2.0$ and $L/D = 2.5$ is due to a flow regime switch to the re-atatchment regime having a signifcant effect on the downstream cylinder's drag forces. For the smaller size ratio configurations, this regime switch occurs at smaller spacings which are not captured in this study and therefore could explain for the shallower curve gradients observed.

7.3.2. Velocity data

The velocity field for the downstream cylinder is very different to that of the individual cylinder or upstream case, due to the flow being heavily perturbed upstream. For the drafting cylinder, the drag reduction is due to both upstream flow effects and reductions in size for the trailing edge low velocity regions. Both of these effects can be analysed in Figure 7.13, where the velocity contours at various Z-heights for the $L/D = 3, d/D = 1.0$ configuration are shown. At the low Z-height, $z/H = 0.22$, a very large and wide wake is evident both at the leading and trailing edge of the downstream cylinder. When analysing the incoming flow velocity for the cylinder, intuitively, due to the drag force being proportional to the square of velocity, reducing the incoming velocity will reduce the drag force. Another observation at this low Z-height, is that the cylinder is fully immersed within the wake, which results in a reduced flow acceleration around the edges, hence producing a weaker adverse gradient. Pairing this pressure gradient effect with the increased turbulence intensity of the incoming flow, mixing higher energy flow into the cylinder side boundary layer, this causes the boundary layer separation point to be delayed significantly. This effect can be clearly viewed at $z/H = 0.22$, with the low velocity region being nearly entirely removed from the trailing edge of the cylinder. It must be noted that the masked region is larger for the lower Z-heights due to the cylinder blocking optical access, resulting in less of the low velocity, near surface flow to be captured. Nevertheless, this observation is still occurring further away from the cylinder surface, demonstrating that low velocity region reduction is still occurring.

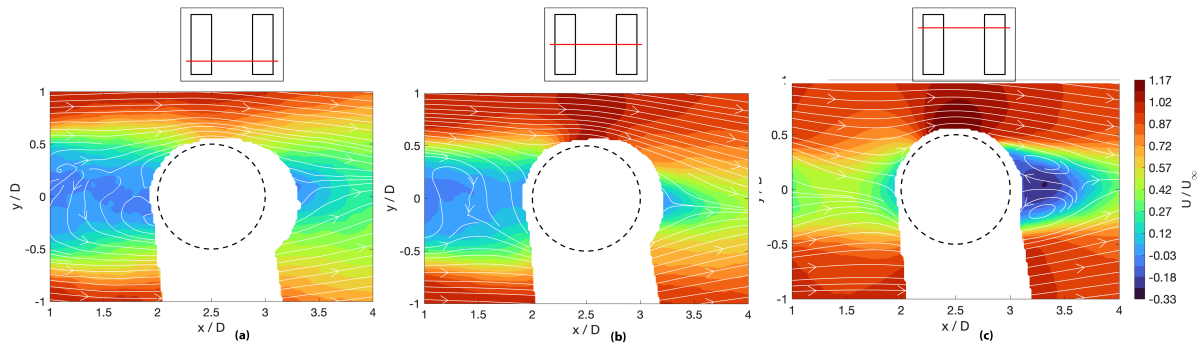

Figure 7.13: Velocity contour lines of x-component velocity around the tandem downstream cylinder for the $L/D = 3, d/D = 1$ in the XY plane at Z-height (a) $z/H = 0.22$, (b) $z/H = 0.05$, (c) $z/H = 0.78$

It should be highlighted that for the downstream cylinder's trailing edge, the size of the wake does not entirely correlate with the drag resistance experienced. Moving higher up the cylinder, namely $z/H = 0.50$, both the incoming wake and shedded wake for the downstream cylinder is reduced in size, with the incoming velocity being of a slightly higher average velocity to that measured at $z/H = 0.22$. Additionally, the incoming wake is narrower, causing the downstream cylinder to no longer be fully immersed. However, at the trailing edge, the low velocity region is of similar size to that at the lower Z-height, implying an equivalent local drag force. This is noted by Luo et al. 1996 where they observe a relatively constant local drag coefficient for the bottom half-height of a finite cylinder. Near the top of cylinder, at $z/H = 0.78$, the very narrow wake, associated with a measurably higher incoming

flow velocity, causes a large flow acceleration and its associated strong adverse pressure gradient. Interestingly, this produces a considerable region of negative velocity at the trailing edge, which can be associated with a local drag increase at this specific Z-height trailing edge, relative to the individual cylinder case. A detailed view of these variations in wake width in the YZ plane immediately upstream and downstream of the trailing cylinder is illustrated in Figure 7.14. Furthermore, it can be noted, that indeed a sizeable low velocity region is present behind the trailing cylinder at the higher Z-heights.

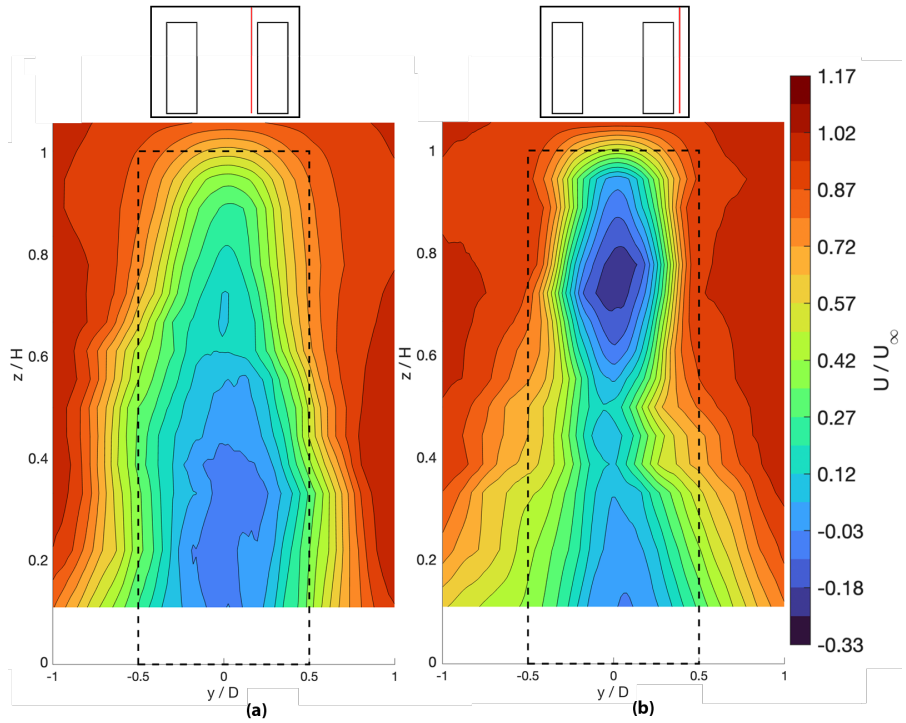

Figure 7.14: Velocity contour lines of x-component velocity in the YZ-plane, (a) immediately upstream and (b) immediately downstream, of the trailing cylinder for the $d/D = 1.0$, $L/D = 3.0$ configuration

The noticeable low velocity region at Z-height $z/H = 0.78$ is not present behind an individual cylinder. Unlike the upstream cylinder, as there is no further flow interaction behind the trailing cylinder, and observing findings by Terra et al. 2017, this additional low momentum region must result in a lower base pressure at this height for the drafting cylinder relative to its individual counterpart. There are two reasons for why this phenomena is occurring; firstly, as observed by Kim and Christensen 2018, despite the downwash produced by the upstream cylinder, the downstream cylinder is still susceptible to below freestream incoming flow at nearly all Z-heights. This results in the tip vortices produced at the free-end to be of weaker strength, reducing the flow energisation of the wake at the higher Z-heights. However, this does not fully explain how come the low momentum region only occurs at high Z-heights, which counter-intuitively is most influenced by these tip vortices. The second contributing factor can be understood when observing Figure 7.13 again. At $z/H = 0.78$, unlike at the lower Z-heights, the downstream cylinder is no longer fully immersed within the wake of the upstream cylinder. This results in large flow acceleration to occur around the cylinder sides, resulting in an associated strong adverse pressure gradient to be present on the trailing edge of the downstream cylinder. This pressure gradient results in boundary layer separation to occur around $\theta = 130°$ point for the $L/D = 3, d/D = 1$ configuration, causing a larger sized low momentum wake to be present. It is the combination of these two flow features that causes a local drag increase to occur near the free end of a drafting cylinder. It must be noted though, that for the larger aspect ratio cylinders tested by Luo et al. 1996, this drag

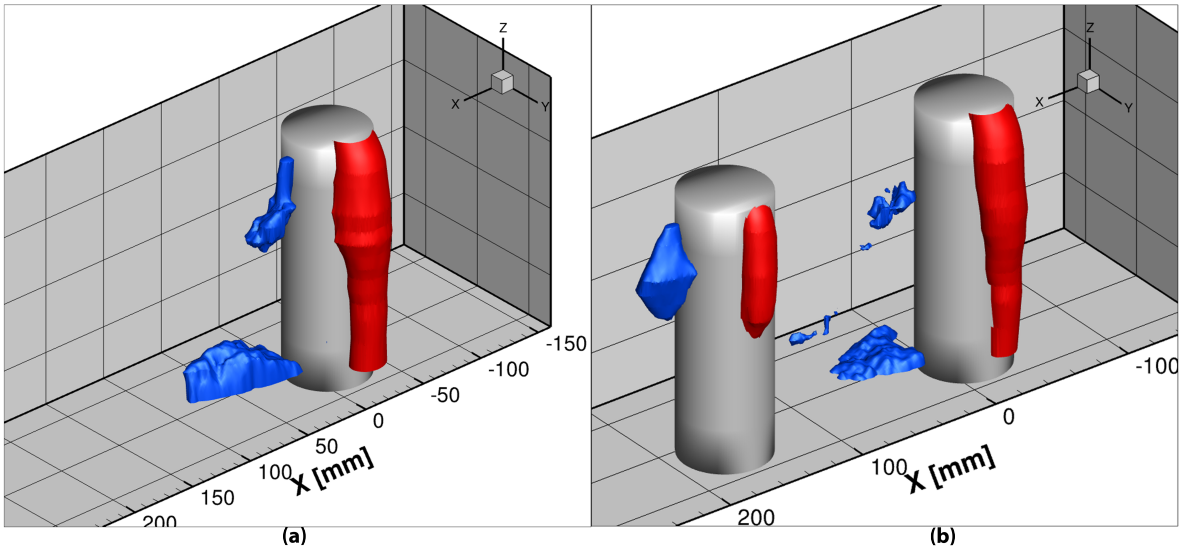

Figure 7.15: Isosurfaces of x-component velocity for $U/U_\infty = -0.1$ (blue) and $U/U_\infty = 1.2$ (red), for the (a) Individual cylinder and (b) $L/D = 3, d/D = 1$ configurations

increase for the downstream cylinder is not observed, suggesting that this phenomena only occurs for cylinders with lower aspect ratios.

In Figure 7.15, the 3D plot of the isosurfaces for $U/U_\infty = -0.1$ highlight the variation in drag forces caused by these specific regions and their contributing factor. In the $L/D = 3, d/D = 1.0$ case, the trailing $U/U_\infty = -0.1$ region is larger than that for the individual case, and contained within this isosurface is a region of even deeper negative velocities which are not present in the individual case, that can be viewed in Figure A.2 in Appendix A. Furthermore, the low momentum isosurface relationship with the flow acceleration region, shaded in red, is clear with both isosurfaces featuring at similar Z-heights. Interestingly, another observation from this isosurface analysis is that the low momentum, re-circulation region near the base of cylinder is reduced in size and magnitude for both the upstream and downstream cylinder. For the downstream cylinder, at the base, there is relatively little flow acceleration and a weak adverse pressure gradient. This causes the boundary layer interaction and pairing between the cylinder sides and test section floor to have a weaker influence on flow separation and reduces the size of the re-circulation region. A comparison in near-cylinder-base flow between the individual cylinder and cylinders in tandem configuration in the XY-plane is shown in Figure A.3 in Appendix A.

The variation in wake width upstream and downstream of the cylinder can be used to analyse where areas of drag reduction for the downstream cylinder occur, and how changes in upstream cylinder affect this and is plotted in Figure 7.16. Immediately upstream of the trailing cylinder, it is logical that the incoming wake width decreases as the Z-height increases, due to the downwash effect in the upstream cylinder's wake. Furthermore, as noted earlier, the larger cylinders produce larger wakes, which results in a wider wake to be experienced downstream. This implies that from a purely upstream perspective, the higher the size ratio, the larger the upstream drag reduction due to an increased size of the incoming wake. The wake width immediately downstream of the trailing cylinder, however does not follow the same trend. For the larger size ratios, namely $d/D = 1.2$, downstream of the drafting cylinder, the wake

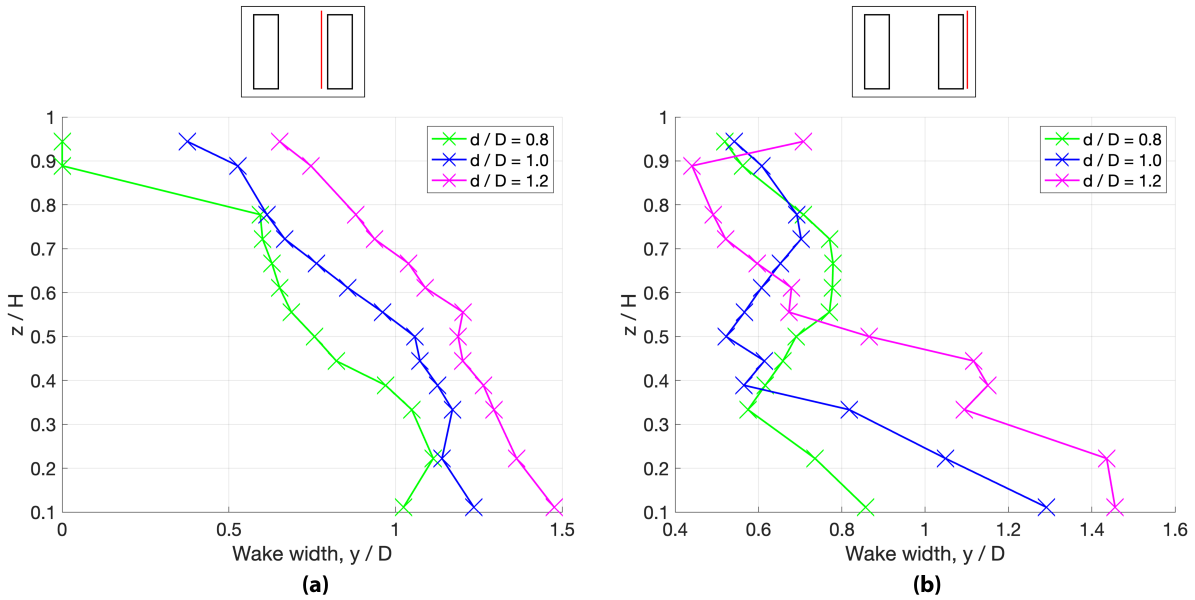

Figure 7.16: Wake width for the x-component velocity isoline $U/U_\infty = 0.5$ for various size ratio configurations, (a) immediately upstream, and (b) immediately downstream, of the trailing cylinder

width is still found to decrease in size as the Z-height increases. Due to the larger upstream wake immersing the downstream cylinder up to the higher Z-heights, a wake size increase occurs only at the very top of the downstream cylinder. This increase in wake width at the higher heights results from the drafting cylinder transitioning from being within the wake to into the freestream, where a strong adverse pressure gradient exists, and creates earlier flow separation with a larger wake. For the smaller size ratio $d/D = 1.0$, a minimum downstream wake width is found around the mid-height, at $z/H = 0.50$, before increasing again with Z-height, due to the drafting cylinder not being fully immersed in the wake above $z/H = 0.50$. Interestingly, for the smallest size ratio, $d/D = 0.8$, it's inability to adequately shelter the downstream cylinder is highlighted as not just being an upstream effect, but also a downstream effect, as a relatively large downstream wake is also present. The downstream wake in the $d/D = 0.8$ case is even larger than that for the $d/D = 1.0$ configuration around the cylinder's upper mid-height. At the upper Z-heights, the drag penalty of having a smaller object upstream is experienced most, with the downwash effect wake resulting in more and more freestream flow conditions to occur for the trailing cylinder, mimicking the individual cylinder case and its assosciated higher drag forces. Furthermore, at the free-end, for both the $d/D = 0.8$ and $d/D = 1.0$ cases, the downstream cylinder is in the freestream and the wake produced is similar and not dependant on the nature of the upstream cylinder. The size ratio effect is most prominent at the low Z-heights, where large variations in wake width are apparent. This is not just because the upstream wake is widest here but also because it interacts with the base boundary layers.

In Figure 7.17, the effect that the spacing of the cylinders has on velocity field around the downstream cylinder is plotted. Interestingly, upstream of the trailing cylinder, the small change in spacing appears to have minimal impact on the wake width and does not explain for the 3% change in drag reduction observed earlier in Figure 7.12. This suggests that the wake profile at the rear of the drafting cylinder must also account for drag force variations between the two spacings. Downstream of the trailing cylinder, again very similar wake sizes between spacing configurations are present, with the only discernible differences occurring at the lower Z-heights, where the $L/D = 2.5$ case is wider. However

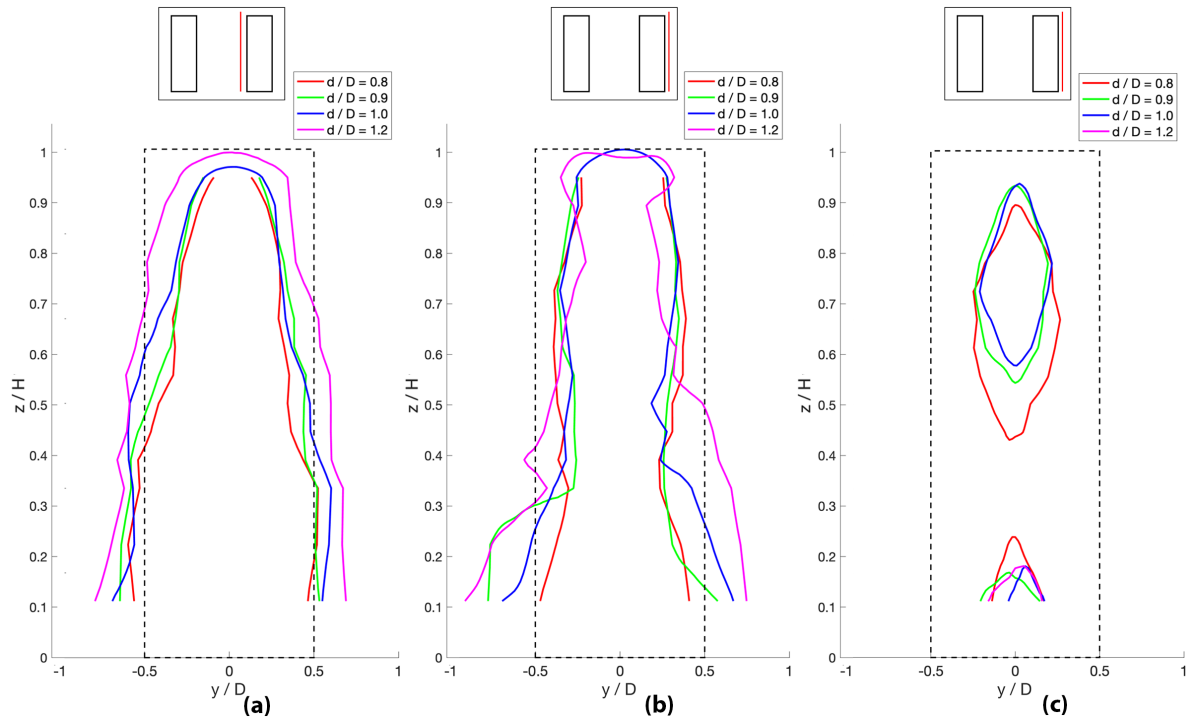

Figure 7.17: Spacing comparison of x-component velocity isolines in the YZ plane immediately downstream of an individual cylinder and for the $L/D = 3, d/D = 1$ tandem configuration, (a) immediately upstream of the trailing cylinder with isoline $U/U_\infty = 0.50$, (b) immediately downstream of the trailing cylinder with isoline $U/U_\infty = 0.50$, (c) immediately downstream of the trailing cylinder with isoline $U/U_\infty = 0$

as noted earlier, a direct correlation between the wake width and drag force at the lower Z-heights is not advised due to the lack of flow separation occurring in this region. However, when observing the very low velocity isoline of $U/U_\infty = 0$, an explanation for the variation in drag reduction is possible, with a discernible difference being evident. The $L/D = 2.5$ configuration has a smaller low momentum region, which results in a smaller drag penalty to occur on the trailing edge. This observation suggests that for the larger size ratio configurations of $1.0 < d/D < 1.2$, the declining gradient of the drag curve (particularly between $2.5 < L/D < 4.0$) observed earlier in Figure 7.12, is due to the upstream flow conditions remaining rather similar, while the downstream conditions vary, which are of weaker influence.

In Figure 7.18, a similar analysis of the wake width is performed, but with configurations of differing size ratios and is the plotted version of the wake width data presented in Figure 7.16. As noted previously, the larger the upstream cylinder, the wider the incoming wake. Downstream of the trailing cylinder, the non-uniformity of the wake is clearly highlighted with no comprehensible trend between size ratio and width of the $U/U_\infty = 0.5$ isoline possible. The exception again is at the low Z-heights where the larger size ratio creates a wider wake, but as mentioned earlier, at these Z-heights, a wider wake does not necessarily correlate with a differing drag force. Analysis of the inner wake is therefore required. The $U/U_\infty = 0$ isoline illustrates clearly that the smaller size ratios contain larger low momentum regions on the trailing edge. This demonstrates that the size ratio indeed has an influence on the downstream effect for drag reduction. It may be further noted, that for the $L/D = 3, d/D = 1.2$ configuration, no low velocity region at the upper Z-heights appears. When a larger cylinder is placed upstream, not only is a larger incoming wake present, containing relatively lower velocity components, the higher wake heights also causes the downstream cylinder to be fully immersed within the wake for higher Z-heights.

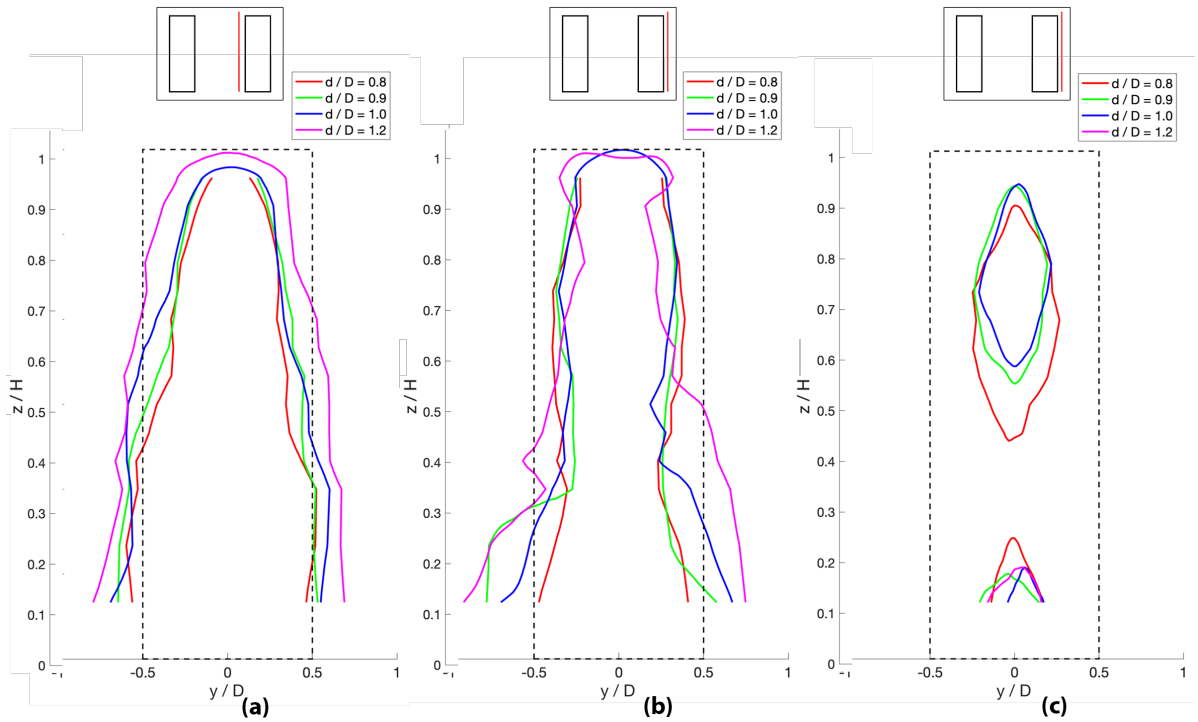

Figure 7.18: Size ratio comparison of x-component velocity isolines between the individual and $L/D = 3, d/D = 1$ tandem configuration in the YZ plane, (a) immediately upstream of the trailing cylinder with isoline $U/U_\infty = 0.5$, (b) immediately downstream of the trailing cylinder with isoline $U/U_\infty = 0.5$, (c) immediately downstream of the trailing cylinder with isoline $U/U_\infty = 0$

This results in a smaller region where large flow acceleration occurs around the cylinder, resulting in a smaller low momentum wake region at the high Z-heights. Both of these effects explain for the large differences in drag reduction for the downstream cylinder measured between configurations of larger size ratios.

Lastly, when referring back to the drag reduction plot in Figure 7.12, the similarity in drag reduction values for both $d/D = 0.9$ and $d/D = 1.0$ at $L/D = 3.0$ was mentioned as a peculiarity in the results, with the difference between the two configurations being a 0.8% difference in drag reduction. By quantifying the area contained within the $U/U_\infty = 0.5$ isoline shown in Figure 7.18, both upstream and downstream of the trailing cylinder, a more detailed analysis on the respective drag forces is possible. Upstream of the trailing cylinder, the isoline area for the $d/D = 1.0$ case is 3% larger than that $d/D = 0.9$ case, and downstream of the cylinder, only 0.9% smaller for the $U/U_\infty = 0$ isoline area. These small margins must first be acknowledged to be within the margin of uncertainty for the PIV measurements. However, it is still plausible that the $d/D = 0.9$ data point at $L/D = 3.0$ is not merely a measurement error, but one due to a slight variation in flow characteristics, between $2.5 < L/D < 3.0$. As an increase in drag reduction in this spacing range also occurs for the $d/D = 0.8$ configuration, it can be assumed that a similar flow phenomena is occurring and the flow visualisations at both $L/D = 2.5$ and $L/D = 3.0$ can be viewed. Due to the small size of the $d/D = 0.8$ upstream cylinder, a large volume of freestream flow is mixed into the gap between the two cylinders. A more notable high pressure region and wake expansion occurs at $L/D = 3.0$ with the smaller size ratio configurations and the high velocity contingent in the wake of the upstream cylinder is forced upwards at an earlier stage. This results in reduced flow curvature and acceleration over the free-end of the downstream cylinder and a weaker adverse pressure gradient, creating a slightly smaller wake behind the trailing cylinder at the upper Z-heights. The consequence

Table 7.2: Comparison between incoming flow and drag reduction for the downstream cyclist for all PIV tested tandem configurations

Spacing	Size ratio	Inflow velocity reduction (%)	Drag reduction (%)
$L/D = 2.5$	$d/D = 0.8$	50.8	8.2
	$d/D = 1.0$	55.4	21.2
	$d/D = 1.2$	61.6	50.3
$L/D = 3.0$	$d/D = 0.8$	52.7	10.0
	$d/D = 1.0$	55.9	18.3
	$d/D = 1.2$	61.7	39.2

of all of these effects is that the downstream cylinder at $L/D = 3.0$ experiences a weaker drag force compared with that at $L/D = 2.5$. In Appendix A, Figure A.4 is plotted showing the velocity profile in the XZ mid plane for both spacings and can be viewed for additional understanding. It is believed that a similar effect is occurring for the $d/D = 0.9$ configuration. It should also be noted that this does not appear to occur at the larger size ratio configurations due to the higher heights of the upstream cylinder reducing the level of freestream mixing in the gap between the two cylinders.

In Table 7.2, the squared velocity average in the YZ plane's immediately upstream of the downstream cylinder is displayed and compared with the measured drag reductions from the force balance campaign. The dimensions of the YZ-plane is $1 < y/D < 1$ in width and $0.11 < z/H < 1.06$ in height. The velocity is normalised by the freestream flow, and is squared to allow for comparison with the dynamic pressure. Of interest is when comparing these inflow velocity reductions with the measured drag reductions. It can be noted that the presence of an upstream cylinder provides significant shelter for the trailing cylinder, with the incoming velocity reduction for the trailing cylinder being greater than 50%, for even the $d/D = 0.8$ configuration. This further suggests that there is a strong upstream drag reduction effect. The fact that the overall drag reduction is lower implies that a downstream effect is also present which increases the drag for the trailing cylinder. This quantification of velocities further supports the observations made for Figure 7.14 and 7.17, which showed that downstream of the trailing cylinder a noticeable relative drag penalty is experienced. It should be noted that the inflow velocity reduction is inflated slightly due to the large stagnation point at the front of the trailing cylinder, which further decreases the velocity of the wake shed from the upstream cylinder.

7.4. Group interaction summary

For analysis of the group interaction between the two tandem cylinders, the combined drag reductions experienced by both cylinders can be calculated. This is measured by summing the upstream and downstream tandem drag coefficients and normalising with the summation of the two individual drag coefficients. As expected, the results are predominantly influenced by the downstream drag reduction due to it being larger than the upstream drag reduction. This includes a similar prevalent trend in the group data, where a larger size ratio configuration will result in a higher overall group reduction, and is an effect that decreases with higher spacings. However, there are also compelling data points which are not apparent when analysing just the individual drag reduction components. Excluding the largest size ratio configuration, an interesting observation is that beyond $L/D = 2.5$, the overall drag reduction is noted to vary by relatively small amounts with increased spacing. This can be explained by the downstream drag reduction decrease being compensated with an increase in the upstream drag

reduction. Furthermore, for some configurations, at $L/D = 3.0$, the upstream drag reduction increase is remarked to be even greater than the downstream drag reduction decrease, and causes the group drag reduction to increase slightly.

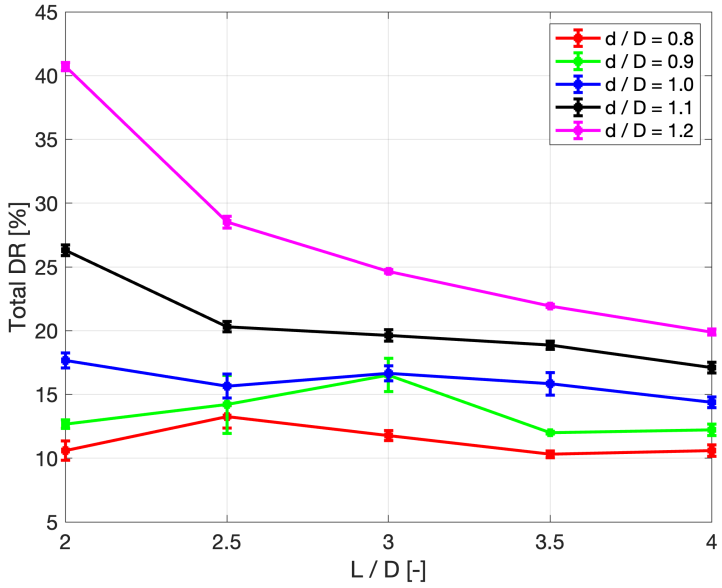

Figure 7.19: The total drag reduction for a group of cylinders in tandem at various spacings and configurations

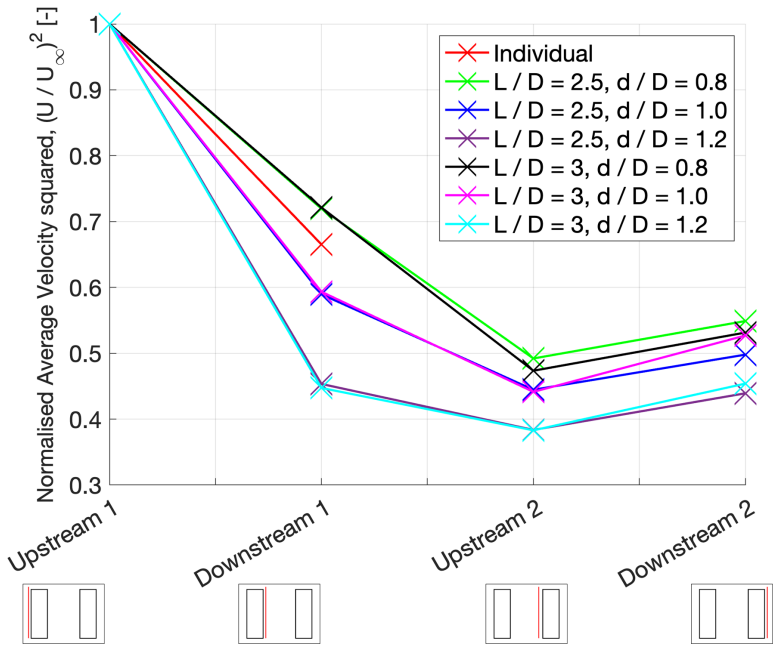

Figure 7.20: Normalised average squared velocity comparisons at various YZ-plane locations

By taking the average of the normalised squared velocity in the YZ-plane upstream and downstream of both tandem cylinders, a macroscopic analysis of each configuration is possible. Up until the "Upstream 2" location, the configurations which have been earlier noted to create larger wakes in between the two cylinders, naturally create a larger deficit in the average squared velocity and is particularly notable for the $d/D = 1.2$ cases. It can also be observed that each of the size ratio

configurations are similar in value and show minimal variation between spacing configurations. It should additionally be noted that the reduction in squared velocity between "Downstream 1" and "Upstream 2" is primarily due to the stagnation point, which reduces the magnitude of the incoming velocity, despite the influence of freestream mixing.

The increase in squared velocity from "Upstream 2" to "Downstream 2", suggests that a reduction in the velocity deficit is occurring across the downstream cylinder. However, as noted before, this is due to the undervaluing of the squared velocity at location "Upstream 2". If the squared velocity at 'Downstream 2' is compared with that at "Downstream 1", it can be observed that an increase in the velocity deficit occurs downstream of the trailing cylinder for most configurations. Interestingly, the deficit across the $d/D = 0.8$ and $d/D = 1.0$ are relatively similar. This suggests that if a third downstream cylinder is positioned, it will be less effected by the nature of the most upstream cylinder. This exception to this is for when a $L/D = 1.2$ cylinder is placed upstream. In this case, the velocity deficit across the downstream cylinder is in fact observed to decrease slightly or even remain constant. This is largely due to the absence of the low momentum region behind the trailing cylinder in the $d/D = 1.2$ cases.

8

Results and Discussions: Drafting cyclists in tandem

In this chapter, the results for two drafting cyclists is discussed and analysed and compared with the results obtained in the previous chapter for the cylinder models. Firstly, the aerodynamic characteristics for the individual cyclist case is detailed and compared with that collected from the tandem configurations. The drag reductions and variation in flow structures for the upstream and downstream cyclist is analysed independently from each other. The group interaction and drag reduction for two drafting cyclists is additionally covered and the aerodynamic relationship between tandem cylinders and drafting cyclists is discussed.

8.1. Individual cyclist

8.1.1. Drag force data

To best appreciate the interaction effects between two drafting cyclists, it is first recommended to understand and analyse the flow structures around an individual cyclist and observe how these alter when another cyclist is placed in an influencing position. In Table 8.1, the individual drag coefficient for each of the four cyclist models is shown. At a quick glance, an observation is that the increase in size of the cyclist model from $w/W = 0.9$ to $w/W = 1.1$ results in a slight reduction in drag coefficient due to the higher Reynolds number. This mimics observations by Terra et al. 2020, where the wake width behind the lower leg and arm around an identical full scale cyclist model was found to decrease in magnitude with Reynolds number. However, the variation in drag coefficient is fairly minor and not significant enough to believe that different flow structures are occurring between the various models. It must be noted that the model $w/W = 1$ (a) has the largest drag coefficient due to damage ascertained before testing, requiring repairs to be undertaken that increased its drag coefficient slightly. Comparing results with literature is of difficulty as the majority of previous cycling aerodynamics tests undertaken

Table 8.1: Drag coefficients for each of the cyclist models, including comparison with values from literature using experimental wind tunnel methods

Model	U [m/s]	Re	Method	Cd
$w/W = 0.9$ **(Present study)**	30.0	7.2×10^4	Static	0.75
$w/W = 1$ **(a) (Present study)**	30.0	8.0×10^4	Static	0.76
$w/W = 1$ **(b) (Present study)**	30.0	8.0×10^4	Static	0.74
$w/W = 1.1$ **(Present study)**	30.0	8.7×10^4	Static	0.73
Terra et al. 2019	14.8	3.6×10^5	Static	0.72
Padilla et al. 2000	13.9	Not given	Static	0.65
Nørstrud et al. 2008	13.9	Not given	Static	0.79
Underwood et al. 2011	11.1	Not given	Dynamic	0.80 - 0.86

do not provide drag coefficient data independent from the frontal area, or do not provide information about the tested Reynolds number, as noted by Crouch et al. 2017. However, comparison with the force balance measurement of an identical full scale cyclist model is available from Terra et al. 2019, where a high degree of equivalence in drag coefficient values with those collected in this study is observed. In Table 8.1, additional literature values for full scale wind tunnel tests are provided, which were performed at velocities slightly lower than competition speeds. Therefore it can be assumed that the Reynolds numbers are of similar magnitude to that in this present study. It can be observed that the drag coefficient values measured in this study are comparable with that of other wind tunnel results. The literature values displayed re-iterate that the drag coefficient for a cyclist is not just dependent on the Reynolds number, but additionally determined by the position and shape of the cyclist and bike.

8.1.2. Velocity data

Similar to the cylinder case, the flow around a cyclist is not 2D but varies across the Z-heights due to 3D flow effects, however also varies due to a non-uniform cross sectional area of the cyclist body with height. The effect of this variation is shown in Figure 8.1, where the wake behind the cyclist is shown at three heights. Namely, $z/H = 0.51$, located at knee height, $z/H = 0.64$, located at thigh height, and $z/W = 0.76$, located at hip height. It can first be observed, that at each height there is a reasonable region of below freestream velocity region behind the cyclist that is comparatively similar in both shape and size between the differing heights. However, when focusing on the lower velocity regions in the wake, considerable change occurs across the heights. It can be deduced that as the Z-height increases from the knee towards the hip region, the low momentum region behind the cyclist increases both in size and in magnitude. This suggests that the largest drag producing areas of the wake is around the hip area, similar to observations by Crouch et al. 2014. However, it can also be observed that at the lower plane $z/H = 0.51$, despite the smaller low velocity region, the entire wake itself is longer and consists of larger regions of semi-low velocity, suggesting that the wake recovery length is longer. This mimics the wake behind an individual cylinder, with both wake cases containing a downwash element. By analysing the x-component velocity plot, Figure 8.2, located in the YZ-plane immediately downstream of the cyclist's rear wheel, clear identification of the flow separation regions is possible.

As noted by Crouch et al. 2014, two dominant counter rotating vortex pairs are shed from the cyclists lower back and hip region, produced by pressure gradients between the lower back/hip areas and beneath the torso. The cyclist model in this study is in its "high drag" condition with the left leg fully lowered and the right leg fully raised. Observing Figure 8.2 in detail, the flow over the right hip, at

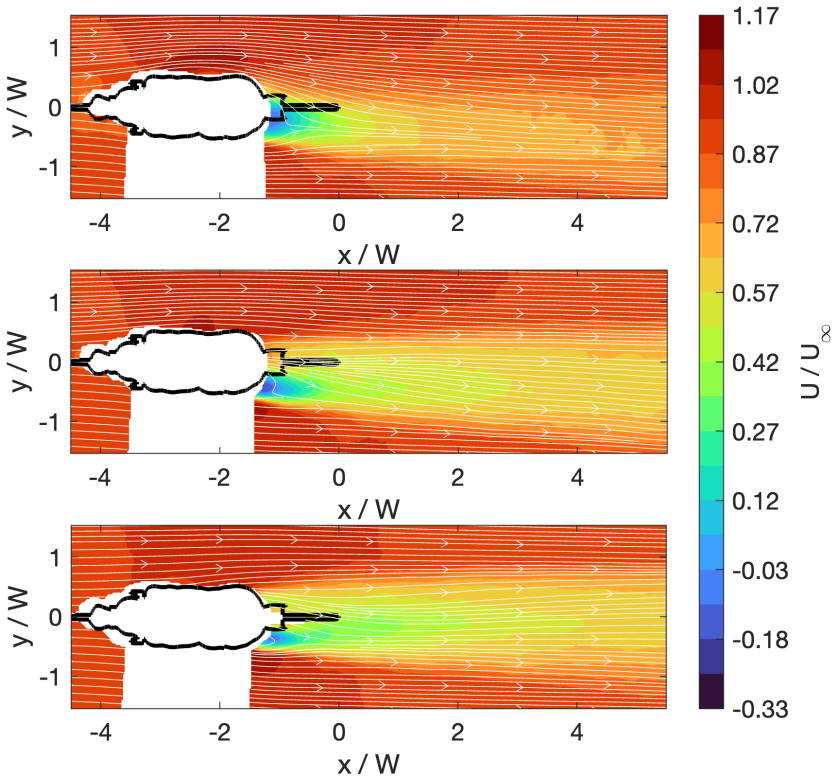

Figure 8.1: X-component velocity contours in the XY-plane around an individual cyclist at Z-heights (a) $z/H = 0.76$, (b) $z/H = 0.64$, and (c) $z/H = 0.51$

$z/H = 0.75$ remains attached and is illustrated as a region of near free-stream velocity. Meanwhile, at the base of the hip and in between the legs, the flow separates and together form a strong anti-clockwise vortex, originating from the center, around thigh height ($z/H = 0.70$). Meanwhile, on the left side there is a region of low velocity extending up towards the low back, due to large flow separation occurring high on the hips, forming a weaker, clockwise vortex centered on the left upper hip ($z/H = 0.80$) . The difference in strength between the two counter-rotating vortices causes an asymmetric wake that tends to the left (when viewing the wake from behind the cyclist) and explains for the velocity profiles plotted in Figure 8.1.

Additionally, in Figure 8.2, the velocity captured in this experiment, (d), is compared with that obtained from a similar PIV experiment by Barry et al. 2016a, (a). Firstly, focusing on the velocity profile captured in this study, a non-uniform wake profile is evident, with the wake shifted towards the left and a high velocity region appearing behind the right hip region. Comparing this wake formation with that captured by Barry et al. 2016a, a fairly different wake is captured in this study. Firstly, it should be noted that the velocity profile in their study is behind a symmetrical positioned cyclist, with equal locations of flow separations occurring either side of the cyclist, creating equivalent counter rotating vortices and therefore creates a symmetrical wake. Between the velocity captured by Barry et al. 2016a and the one in this study, a comparable peak low velocity region is observed around a similar location in the wake between $0.38 < z/H < 0.58$, however the magnitude of the velocity in this region is significantly lower in the study of Barry et al. 2016a. The formation of this low momentum wake region is believed to be flow separation caused by multiple factors, namely low momentum between the legs and strong pressure gradients between the legs and hip region. It is hypothesised that despite the cyclist model used by Barry et al. 2016a being in the "low drag" symmetrical condition, the cyclist body position was

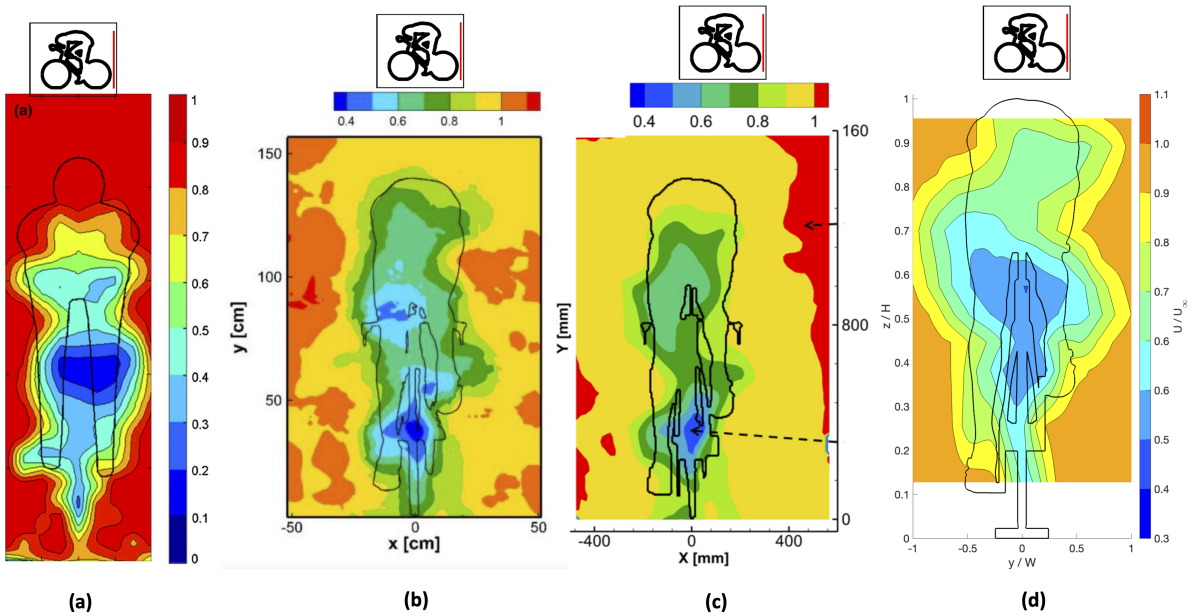

Figure 8.2: X-component velocity contour comparison in the YZ-plane immediately downstream of the an individual cyclist's rear wheel for a (a) TT position cyclist from Barry et al. 2016a, (b) identical full scale model at $Re = 5.74 \times 10^5$ (Terra et al. 2016), (c) identical full scale model at $Re = 1.64 \times 10^5$ (Shah 2017) and (d) this study at $Re = 8.0 \times 10^4$

considerably more upright, causing larger flow curvature over the back and stronger adverse pressure gradients, resulting in a lower velocity wake. The wake measured by Terra et al. 2016 and Shah 2017, using PTV methods for a full scale version of the identical cyclist model, shown in Figure 8.2, (b) and (c), observe a relatively similar wake profile and Shah 2017 noted that another reasoning for the low momentum region is that the measuring position of the YZ-plane is behind the wake of the bike frame and wheel, while being further away from the hips and back regions. It can be noted however, that although the shape of the wake in this study is similar to that captured by Terra et al. 2016 and Shah 2017, the low momentum region in this study is notably larger. This is potentially due the use of a multi-planar technique used in this study, and its coarse resolution in the Z-axis, causing the hip/back flow separation low velocity region to merge with the rear wheel low velocity region through Z-plane interpolation. Nonetheless, it can be reasoned that adequate flow capturing for the description of aerodynamic flow structures has been performed.

When comparing the $U/U_\infty = 0.5$ contour lines behind the cyclist at the three given Z-heights, plotted in Figure 8.3, the variation in wake shape is clearly evident. As observed, the wake is much longer at the low Z-height but is also quite narrow. Furthermore, the left side flow separation is clearly dominant at these Z-heights. At the higher Z-heights, the wake is found to transition to one that is shorter and wider. There are three possible explanations for this; the upstream shape producing the wake at higher heights is wider, resulting in a wider wake. Secondly, at the higher Z-heights, flow separation on the left side no longer takes place, and thirdly, a downwash contingent is pushing low momentum flow downwards, extending the wake at lower Z-heights.

Lastly, the downwash tendency of the wake behind a cyclist is more clear when qualitatively analysing the $U/U_\infty = 0.5$ isosurface in Figure 8.4. Similar to the cylinder condition, the wake can be observed to grow towards the floor region, however the extent at which this occurs is less significant due to the relatively weaker strength of the vortices formed. Furthermore, the non-uniform and asymmetric

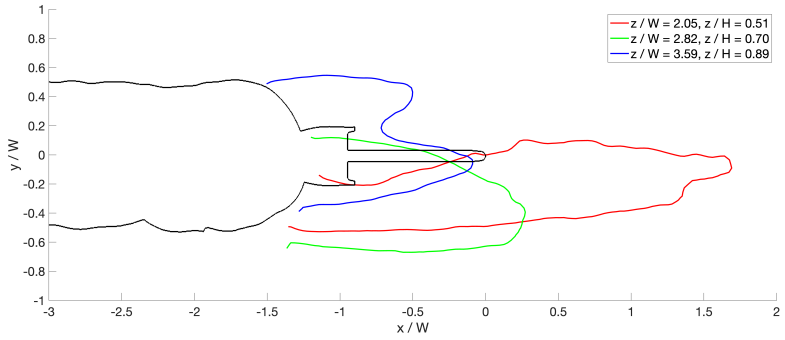

Figure 8.3: Isolines of x-component velocity $U/U_\infty = 0.50$ in the XY-plane directly behind an individual cyclist's body at several Z-heights

profile of the wake is clear and tends slightly the left. The region of high velocity flow attachment on the right side upper hip is evidently not covered by this isosurface. Additionally, just below and towards the Y-axis centerline, the low velocity region within the strong counter-clockwise vortex is described slightly, despite the lack of Z-component velocity being measured in this study.

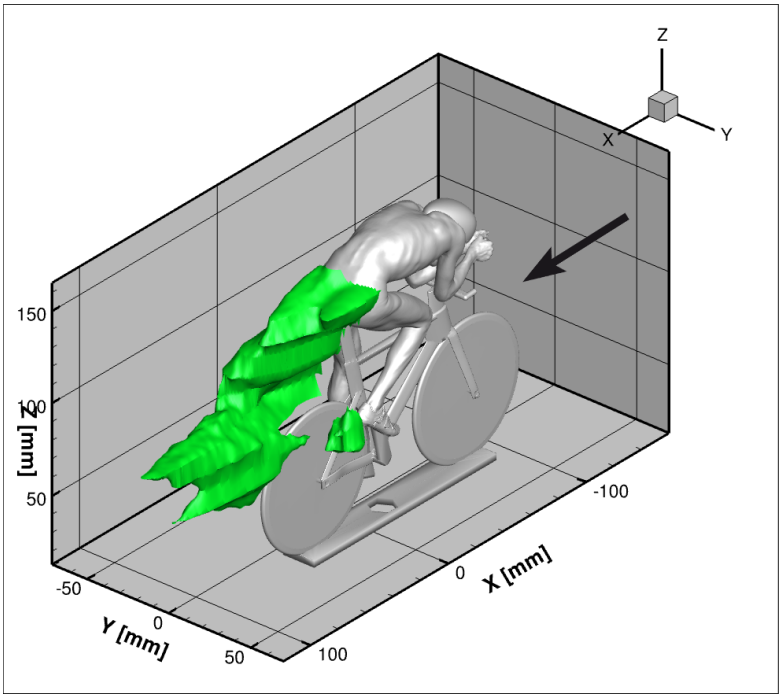

Figure 8.4: Isosurface of x-component velocity $U/U_\infty = 0.50$ behind the individual cyclist model

8.2. Upstream cyclist

8.2.1. Drag forces

Similar to the cylinder experiments, at close spacings, a lower drag coefficient for the upstream cyclist is experienced relative to its isolated case for each of the configuration cases, as can be observed in Figure 8.5. Another similarity is that as the spacing increases, $C_{d,up}$ increases as well, tending towards the isolated case. However it must be noted that the overall range of drag coefficients is far smaller than the

cylinder case, and lacks the presence of any large fluctuations in drag coefficient for each of the size configurations that were present for the upstream cylinder. This suggests that unlike the cylinder case, no flow regime change is occurring between the various spacings and that the upstream interaction effect between the two cyclists is more predictable. It should be noted, although the drag coefficient curve for the $w/W = 1$ configuration is higher compared with other configurations, this is due to the relatively large individual drag coefficient of the damaged upstream $w/W = 1$ cyclist, as mentioned earlier.

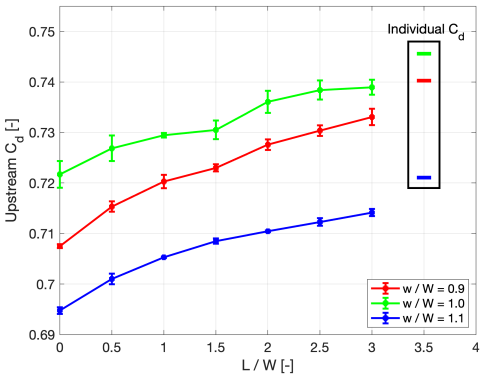

Figure 8.5: Drag coefficient variation with tandem spacing for the upstream cyclist

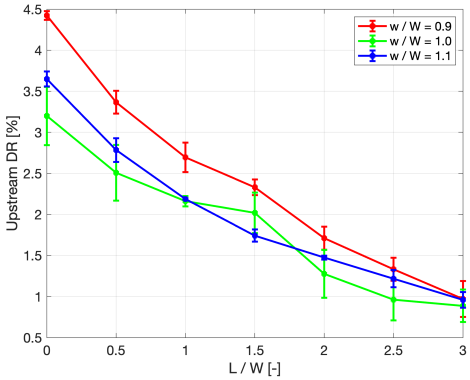

Figure 8.6: Drag reduction variation with tandem spacing for the upstream cyclist. The drag forces are normalised by each upstream cyclist's individual C_d.

The relatively small influence of the upstream flow interaction for the cyclist case is illustrated in Figure 8.6, where noticeably smaller drag reduction values are present compared with the cylinder case. Intriguingly, it appears that there is a non-linear relationship between the size ratio and the upstream drag reduction, with the $w/W = 1$ configuration experiencing lower drag reductions than that for $w/W = 1.1$ case for all spacings, excluding at spacing $L/W = 1.5$. It must be noted, that it is unclear if this unexpected, slight fluctuation in results is due to an undetermined aerodynamic effect or perhaps an anomaly caused by experimental errors, especially as the differences between data points are within their respective margins of error. It should also be noted that the difference in values lying with the error margins is largely due to the very small value differences in drag reduction for the cyclist configurations and not due to a large increase in experimental error assosciated with these measurements. Additionally it is believed that the increased standard error assosciated with the $w/W = 1$ configuration data is due to the damaged model not having the equivalent structural integrity of the other models and was found to oscillate slightly under aerodynamic load. Another observation is that similar to the cylinder case, at the greater spacings, the drag reductions for the leading cyclist from each of the size ratio configurations congregates around similar values and even becomes equivalent at $L/W = 3.0$. With the drag reduction at the largest tested spacing being roughly 1%, it highlights the upstream drag reduction effect is not only of lesser influence compared with tandem cylinder configurations, but also diminishes at a quicker rate.

The tendency for the drag reduction data to decrease with larger spacings, allows for the interpolation of numerical values between the experimented data points by extracting lines of best fit for each of the w/W curves. This is shown in Figure 8.7, where the experimental data is overlaid with best fit lines and compared with similar $w/W = 1$ configuration data of cyclists in TT positions from literature. The X-axis spacial data from the experimental method with 10.8% scale models is converted into dimensional full

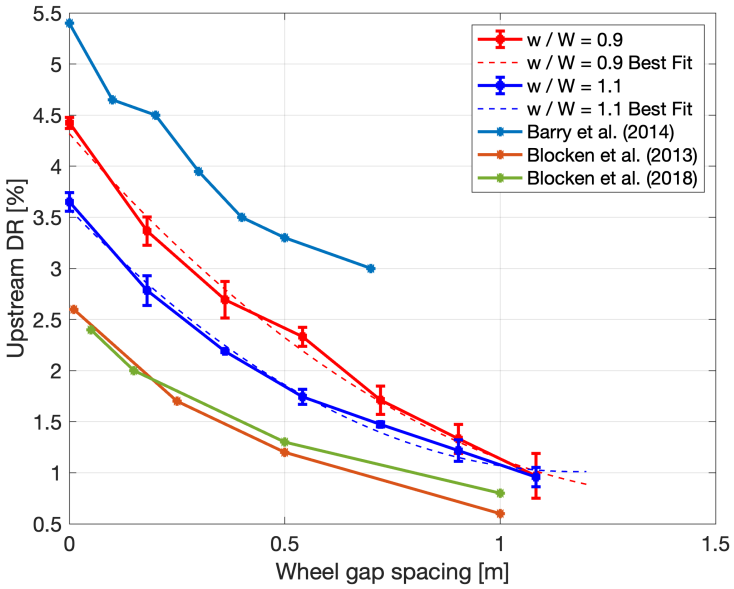

Figure 8.7: Drag reduction variation for the upstream cyclist with wheel gap spacing, including comparison with literature and overlaid lines of best fit

scale wheel spacing by $\left(w/D \times 39 \times \frac{100}{10.8}\right)$. It must be noted that a non-linear, 2nd order line is chosen as a linear fits does not satisfactorily follow the non-linear behaviour of the upstream drag reduction. Due to the fluctuating nature of the $w/W = 1.0$ data, a best fit line operation is not performed on this dataset and is therefore not displayed in Figure 8.7. By interpolating between the empirical constants of the quadratic equations for both the $w/W = 0.9$ and $w/W = 1.1$ best fit curves, the drag reductions for any given combination of size ratio and wheel gap spacings typically seen in professional cycling circumstances can be derived. This is shown in Equation 8.1, where the reader may be reminded that $\left(\frac{w}{W}\right)$ is the shoulder width ratio for the upstream cyclist relative to the downstream cyclist and L is the wheel gap spacing in meters:

$$DR_{up}[\%] = \left(1.12\left(\frac{w}{W}\right) + 0.56\right)L^2 + \left(2.17\left(\frac{w}{W}\right) - 6.76\right)L - 3.69\left(\frac{w}{W}\right) + 7.64 \tag{8.1}$$

Comparing the results from this study with those from literature highlights that slight variations in testing conditions, specifically cyclist posture and shape, and experimental methods can obtain slightly differing results. Nonetheless, it must still be reiterated that the difference with literature is extremely marginal at less than 2%, and it can therefore be observed that the results obtained in this study agree with those captured in previous investigations. It can additionally be noted, that in the wind tunnel experiment by Barry et al. 2014, a similar fluctuating and non-linear behaviour in the upstream cyclist's drag reduction is recorded. Interestingly, the results from Blocken et al. 2013 and Blocken et al. 2018, both do not capture any fluctuating behaviour, however this may largely be due to the nature of the CFD methods used in their study.

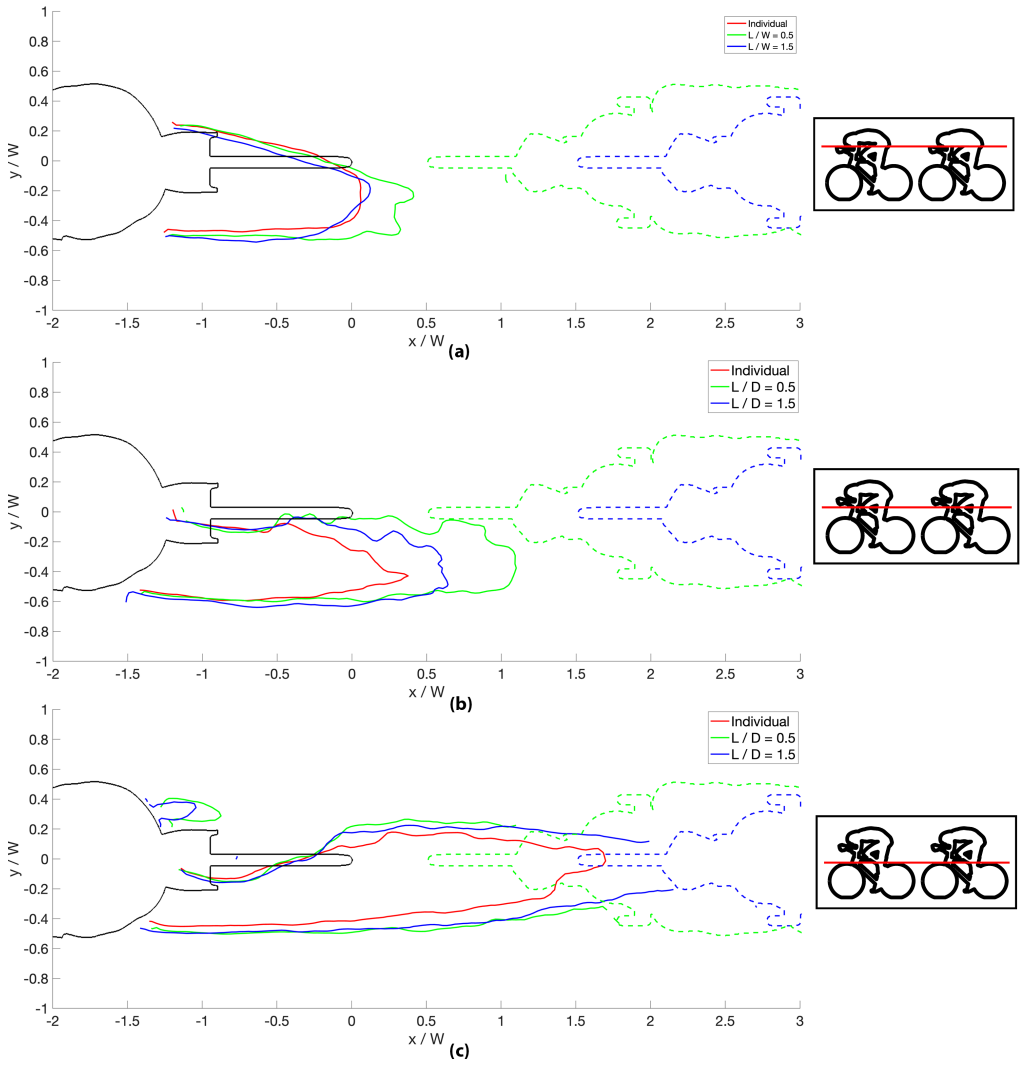

Figure 8.8: Wake isolines of x-component $U/U_\infty = 0.5$ for various configurations in XY-plane at Z-heights (a) $z/H = 0.76$, (b) $z/H = 0.64$, (a) $z/H = 0.51$.

8.2.2. Velocity data

Likewise with the cylinder case, the upstream cyclist's wake is altered by the presence of a downstream cyclist. This wake alteration is illustrated in Figure 8.8, where the wake isolines at several planes for differing spacing configurations are overlaid. The most obvious difference is that the wake appears to extend longer downstream when there is a cyclists downstream and is additionally slightly wider resulting in an overall larger low velocity region behind the cyclist. This is especially the case for closer spacings, namely $L/W = 0.5$. Meanwhile, the wake of the upstream cyclist begins to mimic the individual case at the larger spacings. This is in line with the relatively small 2% drag savings observed earlier in Figure 8.6. Interestingly, another observation is that for both the $L/W = 0.5$ and $L/W = 1.5$ cases, the upstream cyclist's entire low speed wake envelopes the leading edge of the downstream cyclist. From this, it can be deduced that the downstream cyclist's stagnation point is contained within this wake, increasing its overall pressure and therefore reducing the drag force on the lead cyclist. Pressure readings were not taken in this study, however CFD methodology by Blocken et al. 2013 observed a 26% increase in pressure on the upper surface back of a cyclist in a TT position when a drafting cyclist was

placed immediately downstream. Blocken et al. 2013 contributed this pressure increase to the reduced drag forces for the upstream cyclist.

Unlike in the cylinder case, the wake of the cyclist is relatively narrow and when the wake approaches the downstream cyclist, very little expansion of the wake occurs. This is possibly due to the reduced bulbous nature of the cyclist's leading edge creating a weaker high pressure region, further reducing the wake expansion. Furthermore, as observed earlier when analysing the flow around the individual cyclist, the wake behind a cyclist is not only relatively narrower than that behind a cylinder, but also contains a higher average velocity. All of these characteristics suggests that the high pressure region at the rear of the wake is not as influential compared with the cylinder case and explains for the lower drag reductions experienced for the upstream cyclist compared with the upstream cylinder.

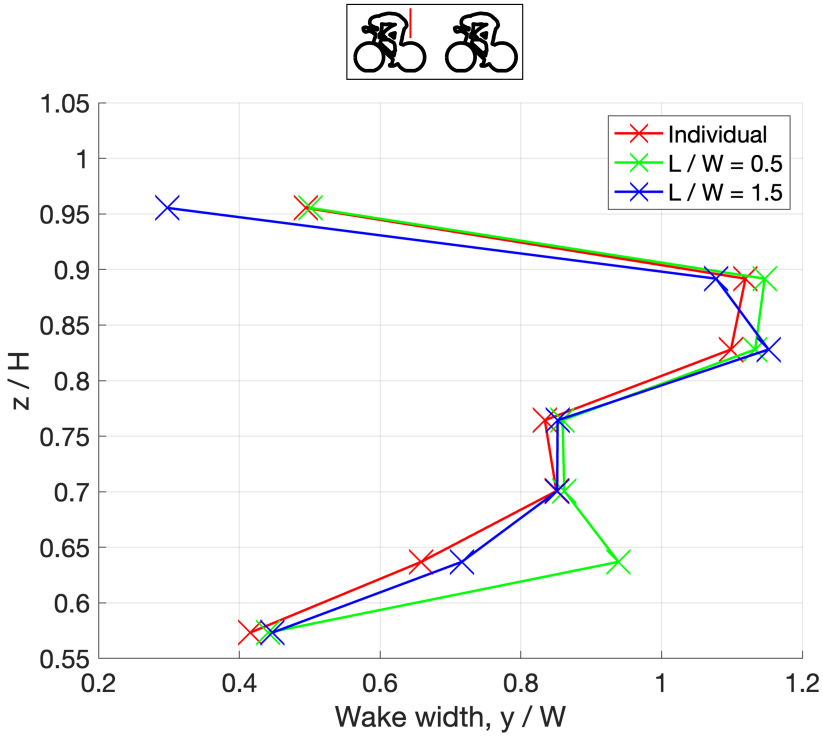

Figure 8.9: Wake width variation directly behind the cyclist body for the X-component $U/U_\infty = 0.70$ isoline in the XY-plane at various Z-heights. It may be noted that planes below $z/H = 0.51$ are not considered, due to the lack of optical access

The wake behind the upstream cyclist is found to vary with height and it can be analysed by measuring the width of the $U/U_\infty = 0.70$ isoline behind the cyclist body at several Z-heights, to get a better understanding of how the wake behaviours differs when a cyclist is positioned downstream, as shown in Figure 8.9. It should be noted, that the wake formation close the cyclist body can only be analysed at the upper Z-heights due to the bike frame blocking optical access below $z/H = 0.50$. Firstly, it can be observed that the wake width progression is not a linear trend like that noticed with the upstream cylinder in Figure 7.9, however varies noticeably due to the varying cross sectional area of the cyclists body and separation regions and vortices being present. However, it can still be observed that there is a relative trend between the various configurations at each Z-height. Firstly, the wake width is found to be slightly larger for the $L/W = 0.5$ case compared with the $L/W = 1.5$ case at all heights, indicating that the spacing ratio has a slight influence on the wake width for the upstream cyclist. On average a larger wake is observed behind the cyclists in a tandem configuration, particularity at

heights $0.58 < z/H < 0.64$, which can be attributed to the Z-height location of the downstream cyclist's handlebar and arms being at a similar height.

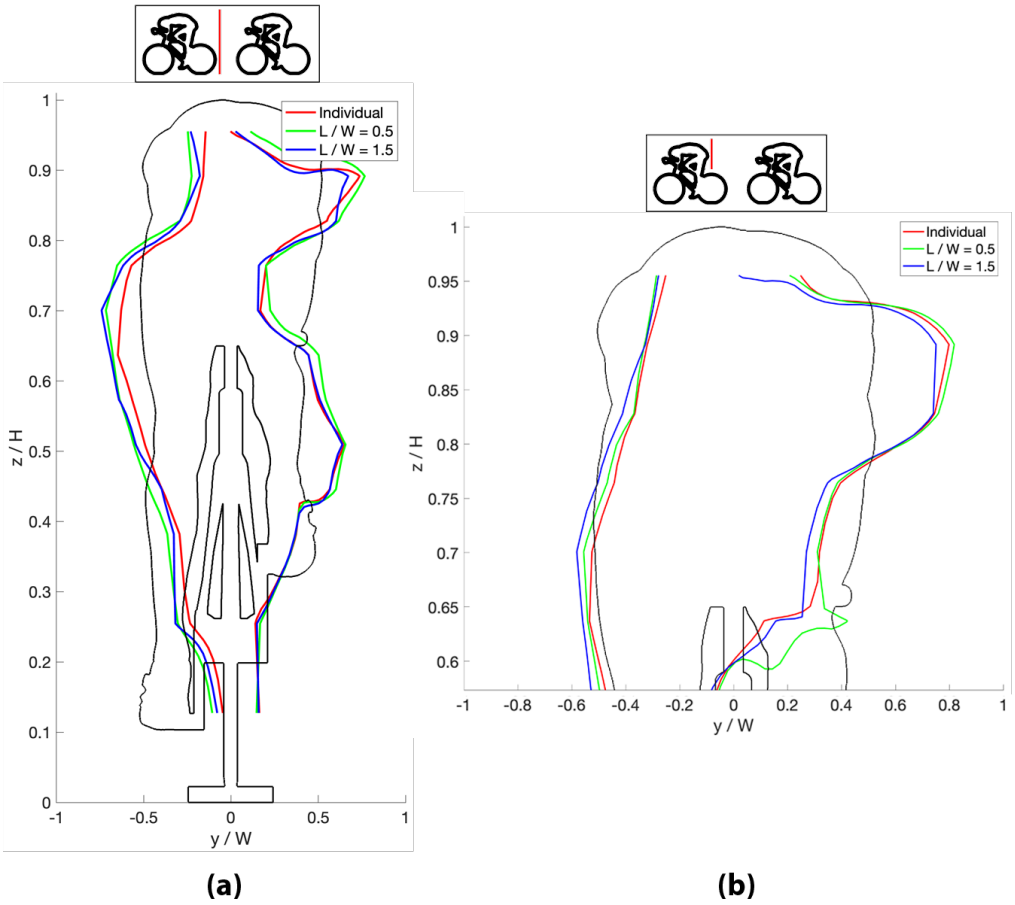

Figure 8.10: Spacing comparison for the x-component isoline $U/U_\infty = 0.70$ in the YZ-plane (a) immediately downstream of upstream cyclist's the rear wheel, and (b) immediately downstream of the upstream cyclist's body

In Figure 8.10, the formation of the wake in the YZ-plane behind the cyclist's rear wheel (a) and behind the cyclist's body (b) is analysed. Downstream of the cyclist's bike, the extent of the wake expansion is most noticeable for the $L/W = 0.5$ case, with the wake being wider at the mid Z-heights below the cyclist's hips, while being relatively similar at the top of the Z-heights. This observation can be explained again due to the presence of the cyclist's leading edge region, namely the hands, shoulder and head being positioned at similar Z-heights, and therefore is also the location of the higher pressure region that influences the upstream cyclist's wake. An additional reason is, that as noted before, the separated flow region behind the cyclist is located at the base hip height. This low momentum region is influenced most by the high pressure region and therefore expands the most when a downstream cyclist is present. The area contained within the $U/U_\infty = 0.70$ isolines is measured to be 15% and 7% larger for the $L/W = 0.5$ and $L/W = 1.5$ cases relative to the individual case. These differences in wake are also observed behind the leading cyclist in a tandem configuration using the Ring of Fire technique, where Mahalingesh 2020 notes an expanded wake compared to the individual case. The wake area increases between spacing configurations are larger than the drag reduction differences recorded in Figure 8.6, suggesting that the velocity profiles in this rear wheel YZ-plane is not fully indicative of drag forces on the upstream cyclist.

Both Crouch et al. 2014 and Shah 2017 observed that the relatively small regions where the vortices are formed, accounted for around 20-30% of the total drag on a cyclist. Shah 2017 notes that this is due to the vortices transferring the freestream streamwise flow energy into cross-flow components, resulting in a momentum deficit which contributes to overall drag forces. Therefore, to achieve a better understanding on the variation in drag forces on the cyclist model between configurations, analysis of the wake profile immediately behind the cyclist body is required. The shape of the wake behind the cyclist's body is found to differ minimally between the various configurations, which better mimicks the drag reduction data, but is also closer to the margins of uncertainty for the PIV data. Yet it can still be observed that the wake for the $L/W = 0.5$ case remains the largest of the three configurations shown. This is further the case when analysing the area again contained within the $U/U_\infty = 0.70$ isolines shown, with the $L/W = 0.5$ and $L/W = 1.5$ cases being measured to be 5.7% and 1.3% larger than the individual case. Most notably, these area increases better match the drag reductions of 3.2% and 2.0% recorded in the force balance experiment for the two respective configurations. Furthermore, it indicates that for the upstream cyclist, the wake region close the cyclist body describes the drag forces experienced relatively accurately compared with the wake further downstream. It is hypothesised that the downstream wake is not only susceptible to freestream mixing but also experiences a larger flow expansion, as it is closer to the downstream cyclist's leading edge and therefore influenced more by the high pressure region. Lastly, at roughly $z/H = 0.65$, the $L/W = 0.5$ configuration's wake isoline can be found to deviate slightly from the individual case and is believed to be due to the proximity of the downstream cyclist altering the flow separation region and vortex formation behind the upstream cyclist. This is noted by Barry et al. 2016a, where the presence of a downstream cyclist, will expand the wake slightly in the Y-axis direction, by translating the thigh vortex away from the cyclist centreline and is clearly the case in Figure 8.10. Furthermore, the attached flow regime around the right thigh can be noted to stay attached for longer, with the assosciated high velocity region shifted further towards the Y-axis center line. This wake profile may be observed in more detail in Apendix B, Figure B.3.

A similar analysis of the wake behind the upstream cyclist can be performed to better understand the influence that the size ratio has on the drag reduction, as shown in Figure 8.11. Firstly, it must be noted that the cyclist profile illustrated in Figure 8.11 is that of the downstream, $w/W = 1$ sized cyclist, and not that of the upstream cyclist which varies in size. Nevertheless, it is clear that when a larger cyclist is positioned upstream, the wake produced behind the rear wheel is also noticeably larger, with the area contained within the isoline for the $w/W = 1.1$ and $w/W = 0.9$ case being 21% larger and 13% smaller relative $w/W = 1.0$ configuration. This is intuitive as a larger upstream body should naturally create a larger wake. Furthermore, it can be observed that certain patterns in the wake are translated slightly in the Z-direction and stretched in the Y-axis between configurations. When analysing the wake downstream of the upstream cyclist's body, a similar wake formation and translation is apparent to the one observed behind the rear wheel. The wake area in the near body YZ plane is measured to vary by around 15% between the different size configurations, and since the size ratios vary by 10%, this explains for the relatively small differences in drag reduction between different size ratios, shown in Figure 8.6.

Analysing the wake isolines between the $w/W = 1.0$ and $w/W = 1.1$ cases, it is not exactly clear what the underlying cause behind the higher drag reductions for the upstream cyclist in the $w/W = 1.0$ configuration is. It is possible, that due to the $w/W = 1.0$ upstream cyclist having been damaged, which increased its individual drag coefficient, resulted in the $w/W = 1.0$ upstream model having a larger relative wake size. This could have caused this specific cyclist model to be influenced by a lesser extent

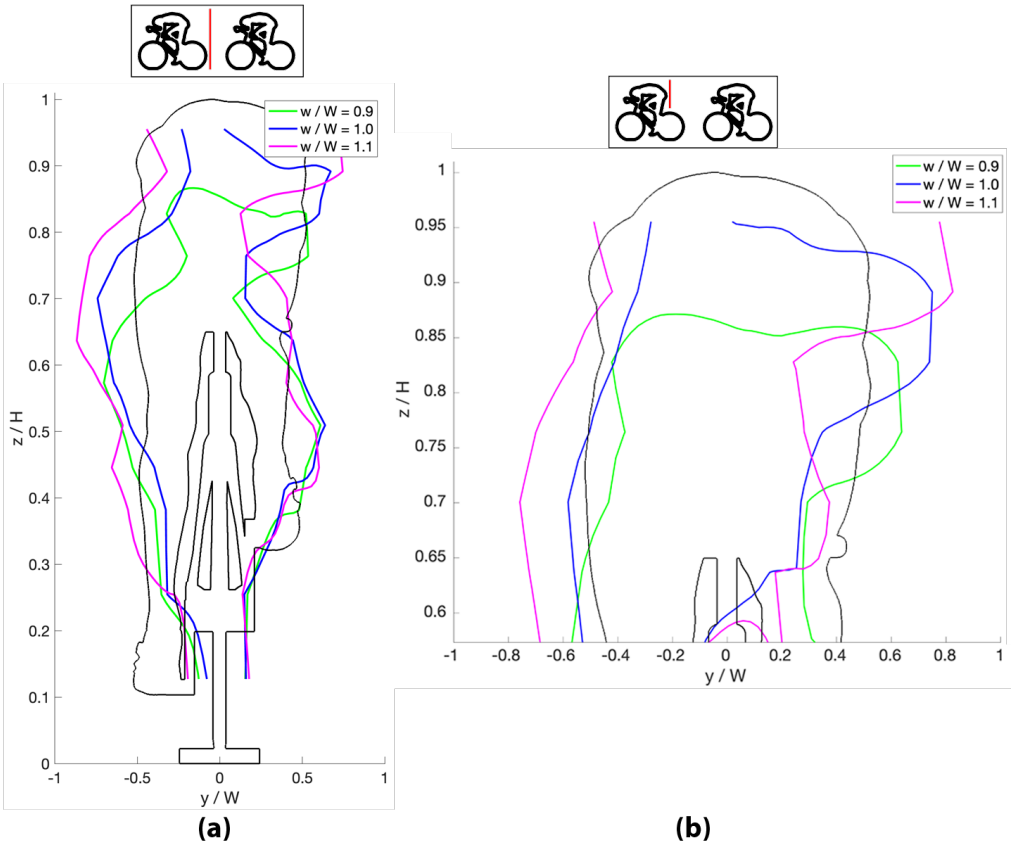

Figure 8.11: Size ratio comparison for the x-component isoline $U/U_\infty = 0.70$ in the YZ-plane (a) immediately downstream of upstream cyclist's the rear wheel, and (b) immediately downstream of the upstream cyclist's body

by a higher pressure region in its wake compared with a non-damaged model, provoking a lower drag reduction. Figure B.4 in Appendix B suggests this, with the wake directly behind the bike frame at $z/H = 0.38$ showing a smaller region of low velocity directly behind the rear wheel for the $w/W = 1$ case compared with both the $w/W = 0.9$ and $w/W = 1.1$ cases. Therefore, the unexpected drag reduction results in Figure 8.6, showing the $w/W = 1.0$ configuration to have the lowest drag reduction, should not be concluded to be caused by a non-linear flow phenomena, but by a manufacturing difference in the cyclist model. Nonetheless, it should still be re-iterated that this effect is still extremely marginal and only highlighted due to the very low margins in the drag reduction for the upstream cyclist, and can consequently still be regarded as valuable data.

8.3. Downstream cyclist

8.3.1. Drag forces

For the downstream cyclist, similarities can be derived from the cylinder case, where an increase in spacing results in a higher drag coefficient, meanwhile an increase in size ratio leads to a reduced $C_{d,down}$, as can be seen in Figure 8.12. However, it should be noted, that differences in drag coefficient for the various configurations are smaller than that for the cylinder case, suggesting that size ratio has a reduced influence on the drag reduction for cyclists. This is more apparent when analysing the drag reductions values in Figure 8.13, where on average, a less than 1% variation in drag reductions are

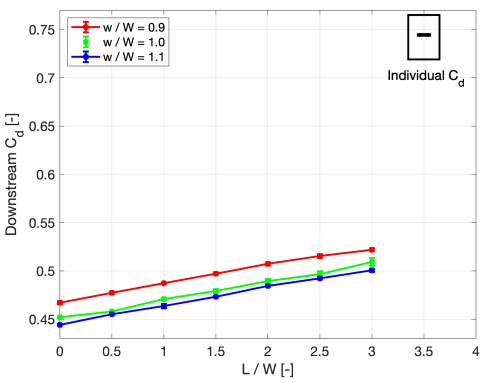

Figure 8.12: Drag coefficient variation with tandem spacing for the downstream cyclist

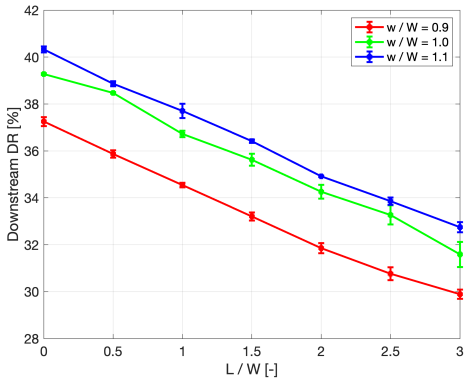

Figure 8.13: Drag reduction variation with tandem spacing for the downstream cyclist

measured between the $w/W = 1.0$ and $w/W = 1.1$ cases. Interestingly, counter to the cylinders, the larger differences in drag reduction occurs between the smaller size ratio configurations, $w/W = 0.9$ and $w/W = 1.0$, where an average difference of around 2% is observed relative to the $w/W = 1.0$ case. It should be additionally noted, that for the cyclists, a reduction in gradient for the drag reduction curve, which is observed with the cylinder data, does not occur for the cyclist models. This suggests that no significant flow regime changes occur for the cyclist cases and that the dominant flow structures remain of similar characteristic. Furthermore, it indicates that, in contrast with the cylinder models, a more equitable variation in the upstream and downstream drag reduction effects occurs between the various cyclist configurations.

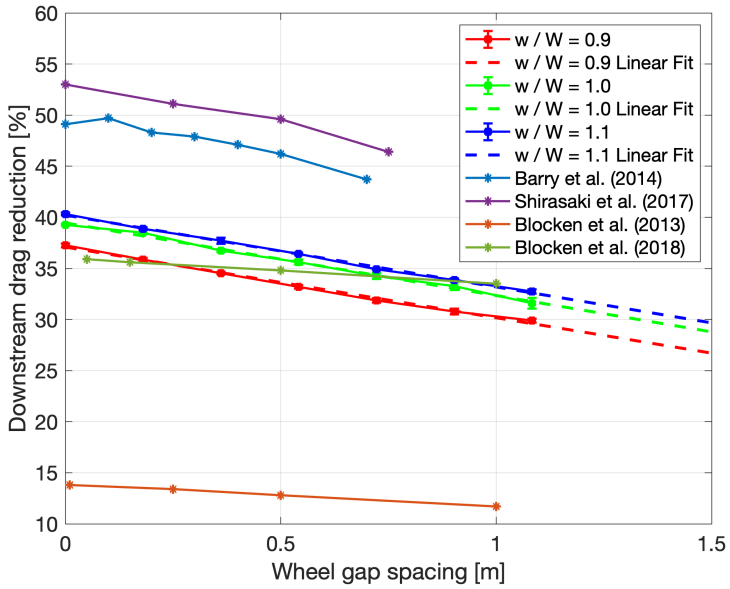

Figure 8.14: Drag reduction variation for the downstream cyclist with wheel gap spacing, including comparison with literature and overlaid lines of best fit

Similar to the upstream cyclist case, a line of best fit can be used to interpolate between data points. However, unlike the upstream case, the downstream cyclist's drag reduction follows more of a linear pattern, perhaps partly due to a linear behaviour of flow interaction with spacing for the downstream cyclist, however it cannot be excluded that the a larger variations in percentages mask any of the small

fluctuation in values. In Figure 8.14, the data is dimensionalised, overlaid with regression lines and compared with data from literature. Firstly, it may be noted, that each of the linear fit lines follow a similar gradient, unlike the upstream cyclist data, with the average gradient being −7.02. In order to obtain an equation that can describe the downstream drag reduction for any spacing and size configuration, a linear interpolation of the y-axis intersections must first be performed for the various size configurations. Through his method, the following equation may be utilised to obtain a drag reduction value for the downstream cyclist for any realistic size and spacing configuration scene in competitive racing:

$$DR_{down}[\%] = -7.02L + 15.62\left(\frac{w}{W}\right) + 23.30 \tag{8.2}$$

Although Equation 8.2 usefully describes and interpolates the data obtained in this study, comparing with literature shows large differences in values obtained from previous experiments. It should first be noted that both Barry et al. 2014 and Shirasaki et al. 2017 performed dynamic experiments, while the cyclist model used in Blocken et al. 2013 and Blocken et al. 2018 was in the "low drag" symmetrical leg position. It is hypothesised that the predominant reasoning for the larger drag reduction values obtained by Barry et al. 2014 and Shirasaki et al. 2017 is that both methods utilised downstream models that were smaller in size than the upstream cyclist. Furthermore, both experiments have cyclists in more upright positions than the cyclist model used in this study, which will result in a larger wake for the downstream cyclist to be immersed in, hence causing greater drag reductions. Meanwhile, the CFD generated results from Blocken et al. 2013 drastically underestimate the drag reduction forces for a drafting time trial cyclist, and is unmatched by other results in literature. It should be noted that in this study, bicycle frames and wheels are not included and only the cyclist bodies are modelled, however Kyle 1979 demonstrates that the majority of drag forces originate from the cyclist body anyway. Furthermore, the results from Blocken et al. 2018, use a similar CFD method but now including both cyclist body and bike model, are in the same range as that collected in this study, however, the gradient of the drag reduction curve with spacing is far shallower, suggesting a far longer wake being computed in CFD which is not observed in this study.

8.3.2. Velocity data

The flow characteristics around the downstream cyclist is heavily influenced by the nature of the incoming flow shed from the upstream cyclist. In Figure 8.15, the variation of the velocity contours in the XY plane at several heights is observed. At $z/H = 0.51$, the incoming wake is a relatively low momentum region and is also quite wide. Similar to the cylinder case, this is one of the main contributions to the drag reductions for the downstream cyclist, whereby a low velocity incoming flow will naturally reduce the drag force experienced by the cyclist, and can be highlighted as the main "sheltering" effect in tandem cycling. However, the incoming velocity still appears to be of a higher velocity compared with the cylinder case. It can also be noted that drag reducing flow effects are also occurring on the trailing edge side of the cyclist. The wake behind the drafting cyclist is wider, and at the lower Z-heights, appears to be a continuation of the wake shed from the upstream cyclist, suggesting a similarity to the extended-body flow regime observed with cylinders. However, observing the inner regions of this wake, there appears to be an absence or large reduction in size of the low momentum regions, that were previously observed behind the individual cyclist. As these low momentum regions indicate flow

separation, it is apparent that there is reduced flow separation behind the trailing cyclist. This implies that there is both an upstream and downstream drag reduction effect on the drafting cyclist. It may be further noted, that both of these effects appear to take place at the higher Z-heights as well, despite the downwash tendency of the incoming wake. A tapering of the wake width with Z-height, like that observed with the cylinders, is not as apparent with the cyclist cases due to the relative lower strength of the vortices shed from the cyclists trailing edge, inducing a weaker downwash. At $z/H = 0.76$, not only is the downstream cyclist still fully immersed within the upstream cyclist's shed wake, but the incoming wake width is of similar magnitude to that seen at lower Z-heights. This is dissimilar to the cylinder case at an equivalent Z-height, and can be partly attributed to the more streamlined leading edge of the cyclist, creating a less evident wake expansion. However it must be noted that the contents of this wake at the higher Z-heights is of relativity higher velocity and contains far smaller low momentum regions.

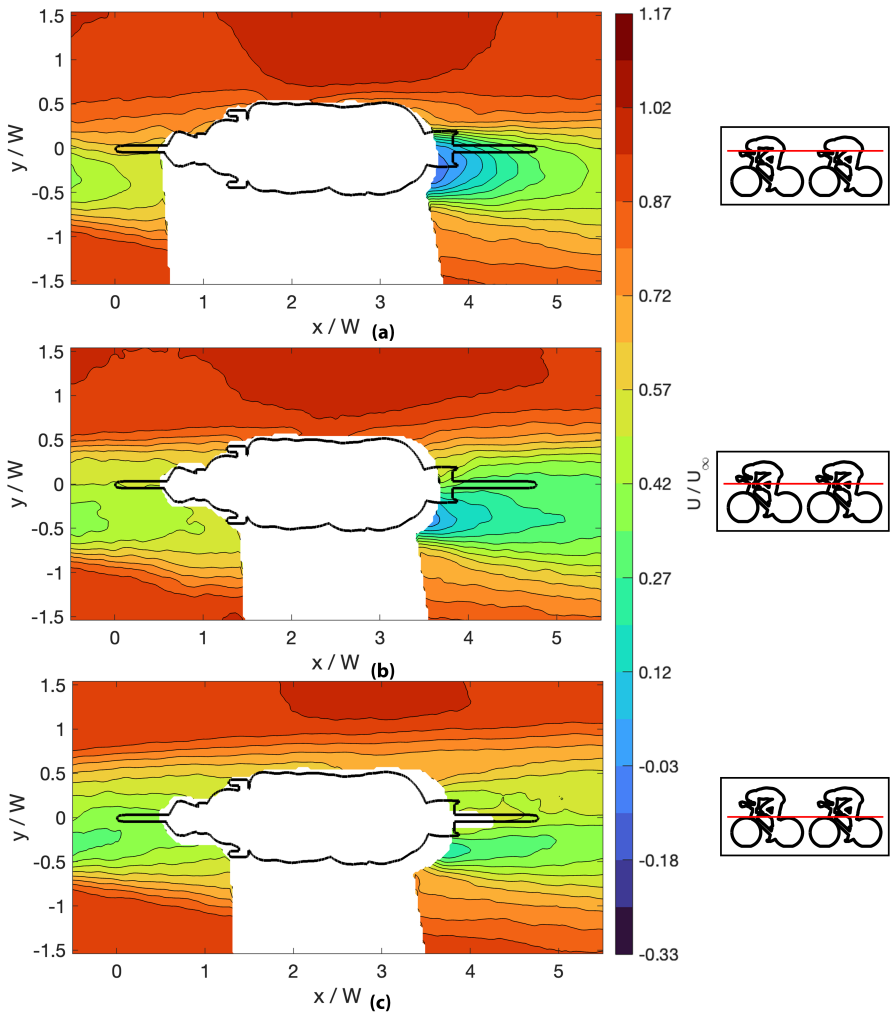

Figure 8.15: X-component velocity contours in the XY-plane around around the tandem downstream cyclist at Z-heights (a) $z/H = 0.76$, (b) $z/H = 0.64$, and (c) $z/H = 0.51$

The variation in wake width around the trailing cyclist with Z-height can be computed at each XY plane and compared with each other and different configurations, as shown in Figure 8.16. It should be noted that the definition of wake width for the cyclist cases is higher for the cyclist conditions, due to the incoming wake being of higher velocity, and is the width for $U/U_\infty = 0.70$ isolines. Furthermore, as the flow features close to cyclist body are to be observed, no wake width computation at the lower

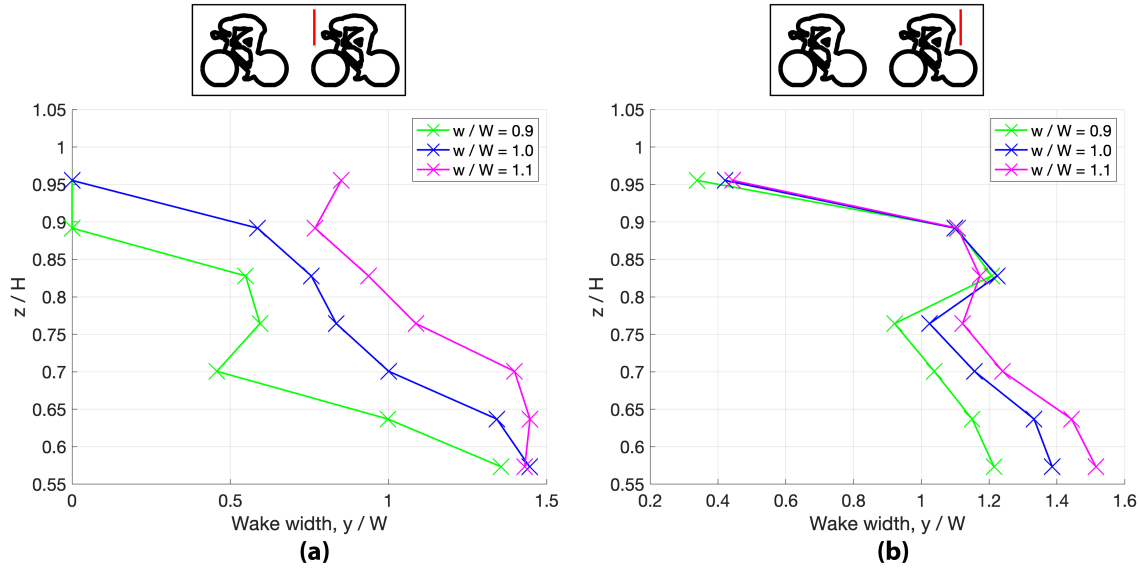

Figure 8.16: The wake width for the $U/U_\infty = 0.70$ x-component velocity isoline measured (a) immediately upstream, and (b) immediately downstream of the trailing cyclist's body.

Z-heights is possible, due to the bike frame blocking optical access and creating a region with no velocity vectors. Upstream of the cyclist, roughly above knee-height, $z/H = 0.54$, the wake width shows minimal variation between size ratio configurations before beginning to diverge at the higher Z-heights. This mimics the wake width observed for the cylinder configurations at very low Z-heights. This suggests that the downwash tendency of the cyclists wake is less extreme and also only occurs at higher heights. This is intuitive as the flow separation regions are located around the thighs and lower back at higher Z-heights, $0.60 < z/H < 0.85$. The wake width drop off point for the cyclist models is delayed to higher Z-heights for the larger size ratio configurations, implying that the larger upstream cyclist will create a larger wake, immersing the downstream cyclist within its wake for longer at higher Z-heights. It must be noted that the entire wake region behind the $w/W = 1.1$ upstream cyclist is not captured and therefore the wake-width drop off point is not observed. For the smaller size ratio configuration, $w/W = 0.9$, a local minimum wake width upstream of the trailing cyclist at $z/H = 0.70$, is measured to grow again slightly, before becoming absent above $z/H = 0.85$. This is due the wake behind the small upstream cyclist being narrow, and the presence of the downstream cyclist's hands, arms and head causing a stagnation area and assosciated flow expansion, increasing the width of the wake. It can be noted that this local wake width minimum is only apparent for the $w/W = 0.9$ case, as for the larger size ratio cases, the incoming wake is wide enough to not be altered as significantly by the leading edge expansion region. For further analysis, the XZ-plane velocity contour plot for each of the size ratio configurations is shown in Figure B.5, in Appendix B.

Downstream of the trailing cyclist, a different trend in wake width with Z-height is observed which appears more fluctuating and less correlated. Between $0.57 < z/H < 0.76$, the wake width behaves in a contrasting fashion to that behind the individual cyclist, where downstream of the drafting cyclist, the wake width is found to decrease, not increase with Z-height. This is believed to occur as the flow separation regions have largely been removed from the downstream cyclist's trailing edge. This is partly due to reduced flow acceleration and weaker adverse gradients around the hips, but also increased turbulence of the incoming flow delaying the separation point. Furthermore, it can also be remarked that the larger incoming wakes caused by a larger upstream cyclist, will also create a larger wake behind

the drafting cyclist. This expanded wake behind a trailing cyclist is also observed by Mahalingesh 2020. Interestingly, the difference in wake width between the $w/W = 0.9$ and $w/W = 1$ cases in this spacing range is slightly greater than that between the $w/W = 1.0$ and $w/W = 1.1$ cases. This potentially explains for the asymmetrical variation in drag reductions observed earlier in Figure 8.13.

Analysing the YZ velocity plot in Figure 8.17 (b), the local minimum in wake width can be attributed to the right side attached flow regime. Interestingly, the wake width is then observed to increase again slightly, followed by another decrease at the upper limits of the Z-height. It can be noted as well, that a disconnection between the characteristics of the wake width upstream and downstream of the trailing cyclist is noted above $z/H = 0.76$. This is due to the flow returning to being separated again behind the lower back (and above the hips), before the wake being removed entirely at the top of the cyclists back, due to the lower cross sectional area of the cyclist at this height. Furthermore, similar to at the leading edge, the size ratio has a direct influence on the wake width on the trailing edge of the downstream cyclist, however as noted previously with the cylinder case study, this does not necessarily correlate with an increase in downstream-caused drag forces.

Referring to the drag reduction plot in Figure 8.13, similar drag reduction values for both the downstream cylinder and cyclist are observed, roughly around the 30% to 40% reduction range, however as observed in Figure 8.15, the incoming velocity is noticeably larger than that for the cylinder case. This suggests that the upstream effect on drag reduction is less powerful, and downstream effect compensates for the higher relative drag forces experienced at the leading edge. By analysing the velocity profile directly behind the trailing cyclist in the YZ plane in Figure 8.17 (a, b), a better understanding of the downstream wake profile is possible. When observing the wake immediately downstream of the trailing cyclists rear wheel, in plot (a) and (b), it is apparent that there is a larger region $U/U_\infty = 0.4$ for the drafting cyclist in the $L/W = 0.5, w/W = 1.0$ configuration, compared with the individual case. This suggests that the drafting cyclist experiences a larger trailing edge drag penalty, and is in accordance with measurements by both Barry et al. 2016a and Mahalingesh 2020, who comment on a reduced energy recovery of the wake to freestream conditions behind a trailing cyclist. However, observing the velocity solely behind the rear wheel is not indicative of the overall drag forces on the cyclist body. The wider wake experienced by the drafting cyclist, will result in a longer wake, as observed earlier in the XY-plots shown in Figure 8.15 and is similar to that observed around the tandem cylinders. The medium-low velocity region, such as the $U/U_\infty = 0.4$ isoline within the wake, is insulated from freestream mixing for longer, resulting in a longer wake formation length and will actually decrease the local drag coefficient. This is hypothesised to be reasoning behind the low velocity region observed in Plot (b).

When analysing the wake immediately downstream of the cyclist's body, in plot (c) and (d), it can now be observed that the individual cyclist has a much larger region of very low velocity, that is additionally lower in magnitude compared with the drafting condition. This is dissimilar to the downstream cylinder condition, and can be described as an effect caused by a delay of flow separation in the tandem configuration. Barry et al. 2016a notes that the strength of vorticity is lower behind a trailing cyclist than that of a individual cyclist, due to the lower incoming flow velocity, which in theory would increase the flow separation behind the cyclist body. However, as the incoming flow not only contains higher turbulence levels, but having the cyclist also immersed within the wake, prevents large flow acceleration around the cyclists leg/hip region, reducing the strength of an adverse gradient and creating a smaller wake. This is notable, as it appears that despite the similarities in wake profiles between the cylinder and cyclists cases, differences in flow characteristics directly around the cyclist body

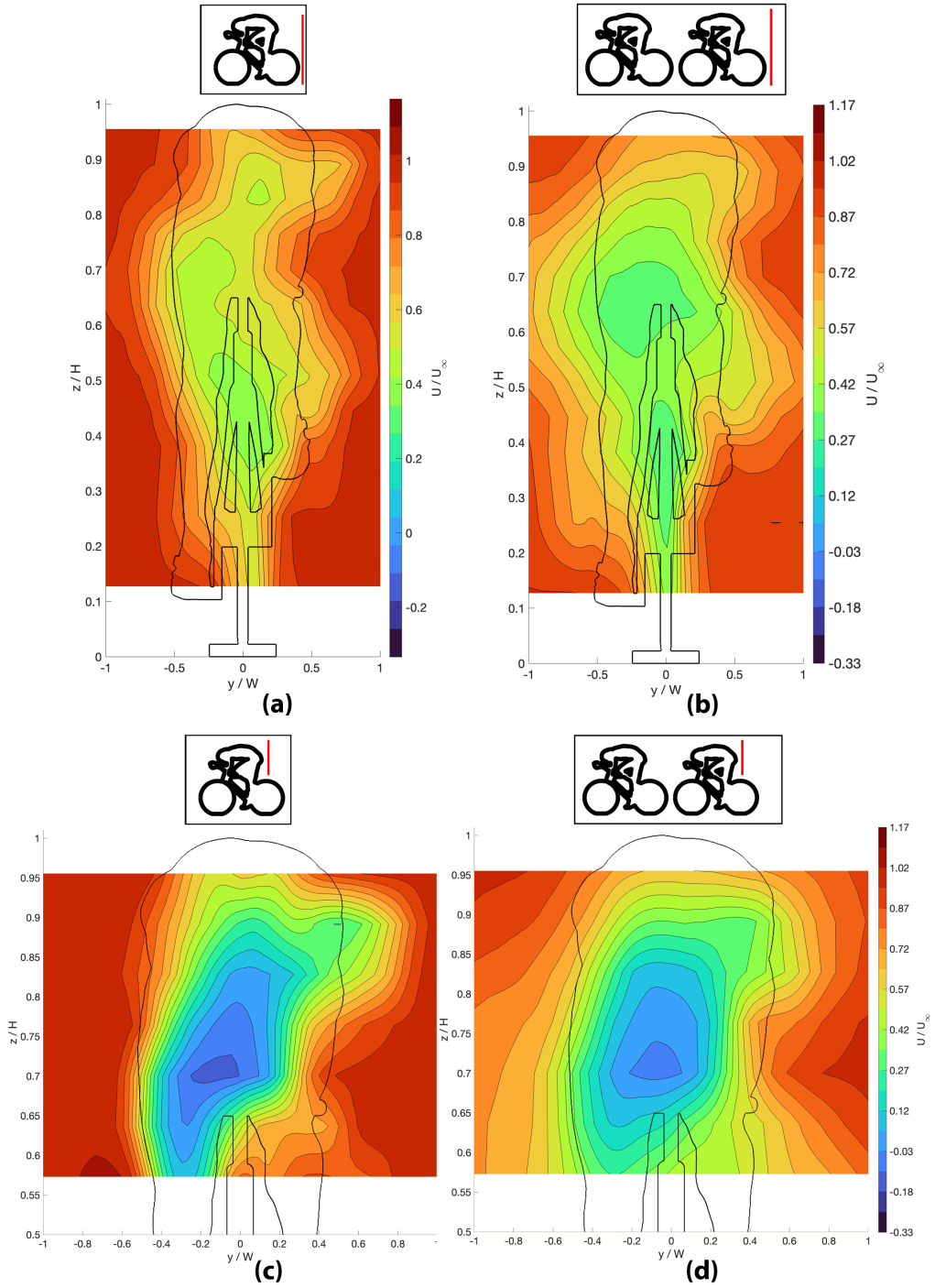

Figure 8.17: X-component velocity in the YZ plane (a) Downstream of an individual cyclist's rear wheel, (b) Downstream of a drafting cyclist's rear wheel, (c) Downstream of an individual cyclist's body, (d) Downstream of a drafting cyclist's body

causes no large flow separation to appear behind the trailing cyclist. The high speed flow acceleration region around the cyclist occurs at Z-heights ($z/H = 0.75$) which are still in the presence of the upstream cyclist's wake and is reprieved from any significant flow acceleration. This can be observed further in Figure 8.17, where the freestream region on the right side hip region ($z/H = 0.75$) is displaced further away from the cyclist body.

The net effect of having a smaller low momentum wake behind the cyclist will reduce the drag forces

experienced downstream of the trailing cyclist. This finding contradicts comments by Barry et al. 2016b and Mahalingesh 2020, however it must be noted that in both studies, wake analysis further downstream than that shown in Figure 8.17 (c), (d) is performed. Furthermore, Blocken et al. 2013 contrarily remarks that the presence of an upstream cyclist, reduces the magnitude of the under pressure present at rear of the drafting cyclist and agrees with the findings of this study. It must additionally be noted, that unlike in the cylinder cases, there is no extreme low velocity region behind the drafting cyclist, which explains how come the trailing cyclist experiences similar net drag reduction values to that of the downstream cylinder but without the same levels of drag reduction at the leading edge.

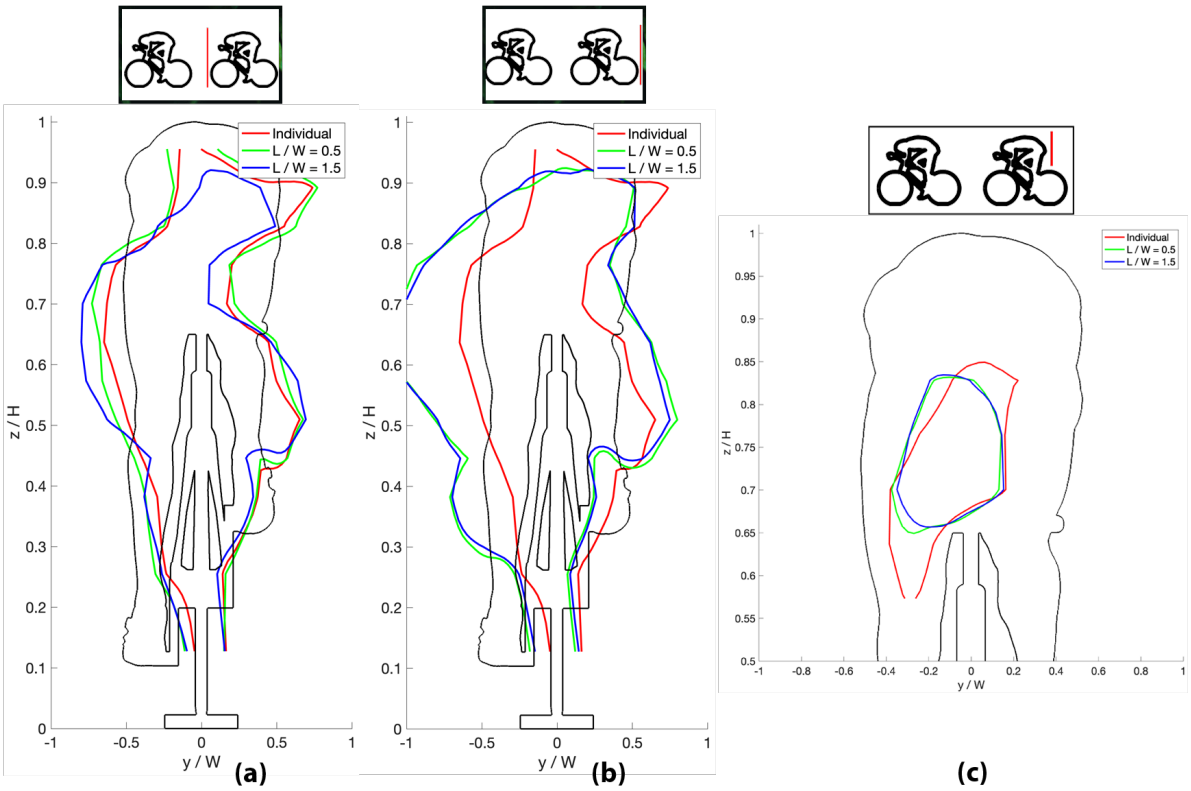

Figure 8.18: X-component velocity comparison between spacings in the YZ plane (a) upstream of a drafting cyclist's front wheel with $U/U_\infty = 0.70$ isoline, (b) downstream of a drafting cyclist's rear wheel with $U/U_\infty = 0.70$ isoline, and (c) downstream of a drafting cyclist's body with $U/U_\infty = 0.10$ isoline

From the drag reduction plot in Figure 8.13, it can be referred that between the $L/W = 0.5$ and $L/W = 1.5$ cases, there is a roughly 2% variation in drag reduction, and in Figure 8.18 the upstream and downstream flow conditions for the drafting cyclist for these two configurations is compared. It can clearly be observed from this analysis that it is purely a difference in upstream flow conditions that is the cause for the variation in drag forces between the two spacings. The drafting cyclists in the $L/W = 0.5$ case, experiences a wake of larger size, with the $U/U_\infty = 0.70$ isoline being measured to be 7.2% larger than that for the $L/W = 1.5$. This is due to reduced freestream mixing occurring for the smaller spacings causing a larger incoming wake. It can further be noted that the incoming wake size for the $L/W = 0.5$ case is even larger than that immediately downstream of the individual cyclist. This is partly due to the minimal wake shrinking that occurs between the two upstream and downstream cyclist, but also due to some flow expansion occurring at the drafting cyclist's leading edge, caused by its stagnation point. Behind the drafting cyclist, as observed earlier, the wake is much larger than that for the individual case. However, most crucially, the spacing is found to have minimal influence on

shape of the downstream velocity profile. This finding holds not only true for the $U/U_\infty = 0.70$ isoline, but also for the low momentum $U/U_\infty = 0.10$ isoline. This further suggests that the cyclist spacings seen in competition environments only effects the upstream conditions for the drafting cyclist and not the downstream wake characteristics.

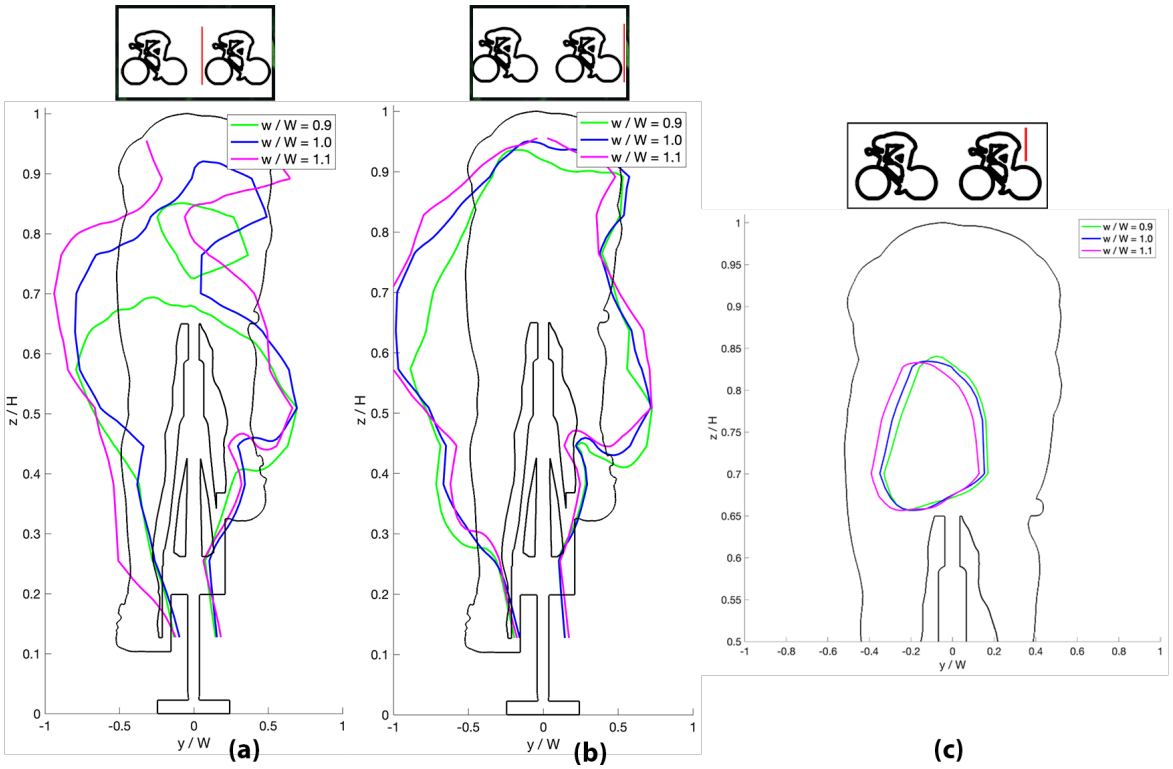

Figure 8.19: X-component velocity comparison between size ratios in the YZ plane (a) upstream of a drafting cyclist's front wheel with $U/U_\infty = 0.70$ isoline, (b) downstream of a drafting cyclist's rear wheel with $U/U_\infty = 0.70$ isoline, and (c) downstream of a drafting cyclist's body with $U/U_\infty = 0.10$ isoline

A similar wake analysis is performed in Figure 8.19, to compare the leading and trailing edge flow conditions for the different size ratio configurations. Evidently, for the large size ratio configurations, having a larger upstream cyclist causes the downstream cyclist to experience a larger wake. For the $U/U_\infty = 0.70$ isoline behind the trailing cyclist, relative to the $w/W = 1.0$ baseline, the $w/W = 0.9$ case sees an 20 % reduction in wake size, while the $w/W = 1.1$ case sees a 23 % increase in wake size. Despite the similar variations in wake isoline area, the $w/W = 0.9$ case, was observed earlier, in Figure 8.13, to have a larger variation in drag reduction, relative to the $w/W = 1.0$ baseline case. It is believed that the nature of the incoming flow causes the downstream cyclist in the $w/W = 0.9$ case to experience a greater variation in drag reduction relative to the $w/W = 1.0$, compared with the $w/W = 1.1$ case. The incoming wake for the $w/W = 0.9$ case is most similar to other configurations at the lower heights, namely $z/H < 0.60$, but shrinks considerably at higher heights. As the majority of the cyclist cross section is located at the higher Z-heights where the cyclist body is present, this is where the majority of upstream drag forces are experienced. As the smallest upstream cyclist does not adequately shelter these upper Z-height regions, a lower drag reduction for the downstream cyclist must occur.

Meanwhile, the size ratio appears to have a small influence on the downstream velocity profile as the drag reduction plot in Figure 8.13 would suggest. However, similar to observations made by Mahalingesh 2020, the complex interaction between the two cyclists does result in a slightly taller

trailing wake when a larger cyclist is placed upstream. However, unlike Mahalingesh 2020, no noticeable widening of the trailing wake is measured when a smaller cyclist is placed upstream. In the low momentum region behind the cyclist body, which has a comparatively more significant influence on the drag force, no noticeable difference in the $U/U_\infty = 0.10$ isoline is apparent between the various size ratio configurations. This is an interesting observation as it implies that despite the main drag reductions for the downstream cyclist being caused by both upstream and downstream flow variations, the differences between different size and space ratios is found to be predominantly an upstream effect.

In Figure 8.20, the full 3D flow around two drafting cyclists is fully visualised and compared between two size ratio configurations. Here, it is again clear where the drag reduction for the downstream cyclist occurs from, with a large low velocity wake being impinged upon the downstream cyclist. Also the variation in size and location of this wake connecting with the cyclist downstream is noticeable with the differing size ratio configurations. For the $w/W = 1.1$ case, the $U/U_\infty = 0.50$ wake connects with the downstream cyclist's upper body and legs, where the majority of the drag forces of a cyclist are experienced, while for the $w/W = 1.0$ case only the legs are immersed within this isosurface. Furthermore, it is apparent that despite the large variation in incoming wake size between the two configurations, a much smaller difference in wake size occurs behind the downstream cyclist.

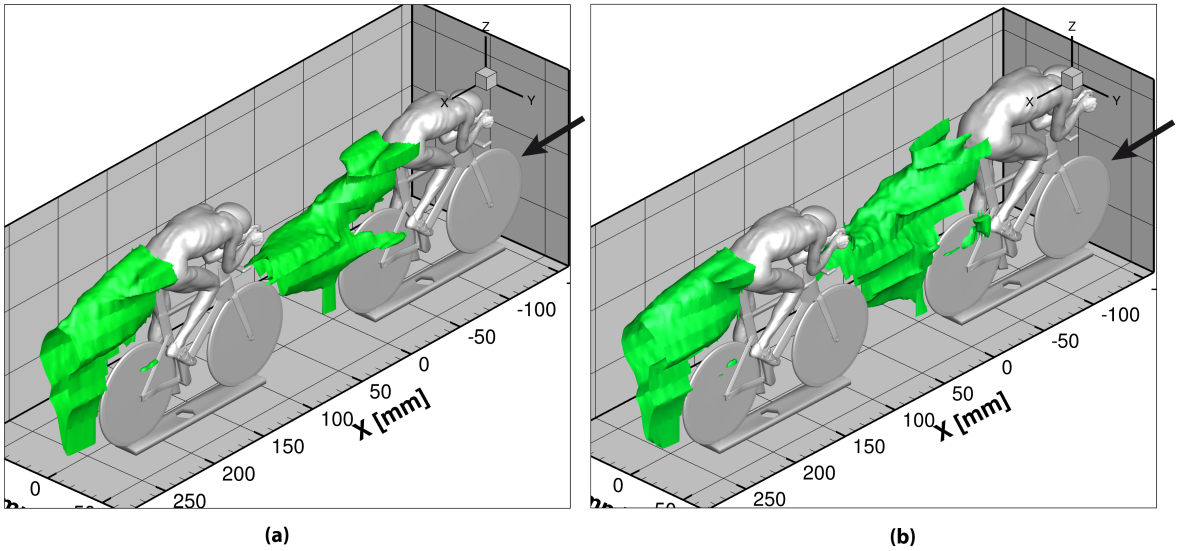

Figure 8.20: Isosurface of x-component velocity $U/U_\infty = 0.50$ around a tandem in cyclists with spacing $L/W = 1.5$ and size ratios (a) $w/W = 1.0$, and (b) $w/W = 1.1$

For the downstream cyclist, the extent the upstream and downstream effects have on the drag reduction can be quantified when measuring the inflow and outflow conditions for the trailing cyclist. The squared streamwise velocity component in YZ-plane immediately upstream of the downstream cyclist is measured and averaged to relate it to the incoming dynamic pressure and is then normalised relative to the freestream conditions. The dimensions of this measurement domain are $-1 < y/W < 1$ and $0 < z/H < 1$. The reductions in average incoming squared velocity are shown in Table 8.2 and compared with the drag reductions measured in the force balance campaign. It is further clear that the downstream cyclist experiences a lower incoming velocity relative to the freestream conditions and this accounts for the majority of the downstream cyclist's drag reduction.

However, it should also be noted that the measured drag reductions are greater than than the

Table 8.2: Comparison between incoming flow and drag reduction for the downstream cyclist for all PIV tested tandem configurations

Spacing	Size ratio	Inflow velocity reduction (%)	Drag reduction (%)
$L/W = 0.5$	$w/W = 1.0$	27.7	38.5
	$w/W = 1.1$	32.1	38.9
$L/W = 1.5$	$w/W = 0.9$	23.7	33.2
	$w/W = 1.0$	27.1	35.6
	$w/W = 1.1$	31.5	36.4

measured inflow velocity reductions for each of the PIV measured tandem configurations. This implies that an upstream effect cannot be the only cause for the cyclist's drag reductions and that a downstream effect, of weaker influence, must also be considered. The differences between the incoming velocity reduction and drag reduction in this study are slightly larger than that obtained by Barry et al. 2016a, yet in their study they fully allocate all of the drag force decreases to upstream caused effects. It must be considered that the chosen cross section in YZ-plane has a large influence on the average velocity obtained and cannot be suitably compared with results from literature with large confidence, such as that from Barry et al. 2016a. However, as shown in Figure 8.18 (c), the $U/U_\infty = 0.1$ isoline immediately downstream of the cyclist body shows a reasonable reduction in drag forces on the cyclist's trailing edge in tandem configurations, highlighting that there is a downstream effect that cannot be disregarded.

8.4. Group interaction summary and relevance to professional cycling

It has been noted that the drag reductions for two drafting cyclists affects not only the downstream cyclist, but also the upstream one. Since in competition conditions, typically numerous cyclists are found in tandem, this makes observing the fluctuations in group drag useful and relatable. The group drag reduction is calculated by adding the drag coefficients for both the upstream and downstream drafting cyclists and normalising this sum relative to the sum of their respective individual drag coefficients. It should be noted, that as the drag reductions for both the upstream and downstream cyclists are not fully independent of each other, averaging of their standard errors is not advised and instead a simple addition of their respective errors has been performed. In Figure 8.21, the variation of the total drag reduction with spacing is plotted. It can clearly be observed that due to the comparatively low drag reduction effects on the upstream cyclist, the results are largely influenced by the downstream cyclist's drag reduction. This is noted with the fact that that the larger size ratios configurations experience a higher overall group drag reduction for all spacing configurations.

In Figure 8.22, the quadratic best fit curves for each size ratio configurations are plotted alongside with the experimental data. In a similar fashion to the upstream cyclist data, the total group drag reduction for any combination of size ratio and wheel gap spacing can be calculated using Equation 8.3:

$$DR_{total}[\%] = \left(-1.15\left(\frac{w}{W}\right) + 2.52\right)L^2 + \left(2.54\left(\frac{w}{W}\right) - 8.89\right)L - 6.92\left(\frac{w}{W}\right) + 14.63 \tag{8.3}$$

Although the trends in the total drag reduction graphs are expected, this is a noteworthy observation, as it entails that the benefits of having a larger sized cyclist placed upstream are significant for the cyclists

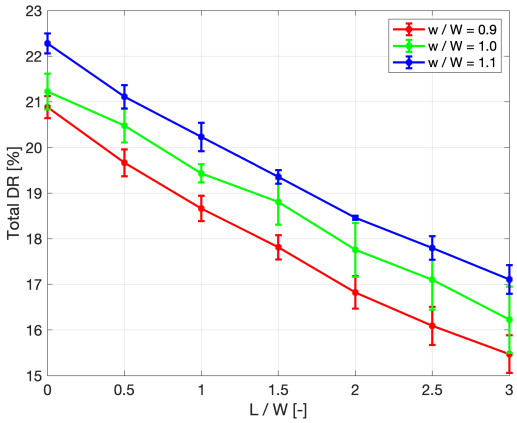

Figure 8.21: Overall drag reduction for the two tandem cyclists variation with spacing and size ratio

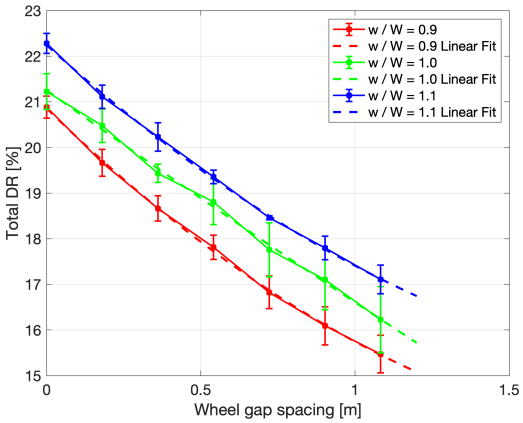

Figure 8.22: Overall drag reduction with wheel gap spacing overlaid with best fit lines

drafting behind and results in only a small potential drag penalty for the upstream cyclist. Furthermore, as a larger cyclist is typically found to have a higher power output (Davies and Sandstrom 1989), it is feasible that they are able to overcome the higher associated drag forces and maintain a set speed, while providing a large drag reduction for the downstream cyclist. Although the group drag reduction between the $w/W = 0.9$ and $w/W = 1.0$ configurations at $L/D = 0$ are relatively similar, this spacing is too close and cannot be feasibly held in competition circumstances. It should noted, however, that placing a larger upstream cyclist does have the potential of increasing the lateral spacing configuration for the downstream cyclists, as their view is increasingly blocked. Nevertheless, for professional cyclists this effect should still be less influential than that noted by Kyle 1979 and Edwards and Byrnes 2007.

Although the models tested are in a time trial position, certain observations can be made for a sprint train scenario. A similar goal is that the drag reduction for the entire tandem group is best minimised to keep the velocity of the sprint train sufficient, while conserving energy for the priority sprinter at the rear of the sprint train. This suggests that at the front of a sprint train should be a larger sized cyclist in order to provide significant drag reductions for numerous downstream cyclists, while maintaining a high velocity for the sprint train. However, a notable difference to the team time trial case, is the presence and role of the lead-out man for the sprinter. Not only does the lead out man need to provide aerodynamic shelter to the trailing sprinter, but must additionally accelerate up to a high enough velocity to provide a fast initial velocity for the sprinter to launch their sprint. This results in the compromise between upstream drag reduction and downstream drag reduction for two tandem cyclists to be increasingly important. Therefore, it is believed that the presence of a similarly sized lead-out man immediately upstream of the sprinter will provide the optimal competitive condition for a team. Although the downstream sprinter will experience a slightly higher drag force, the lower drag reduction for the upstream cyclist will allow the two cyclists to achieve a higher group velocity and allow the sprinter to launch their sprint at higher speed. Furthermore, this effect has the additional benefit of reducing the possibility of another sprinter from an alternative sprint train obtaining the draft behind the main sprinter.

An additional point to note is that if a 10% larger cyclist is placed upstream (Position 1), not only does the immediately downstream cyclist (Position 2) experience a greater relative drag reduction, but the wake behind this cyclist is measured to be roughly 6% greater in size. If, like in a team time trial or

sprint train, an additional cyclist is placed further downstream (Position 3), they will experience an even greater drag reduction, as measured by Blocken et al. 2018. This is significant, as it suggests that the size ratio of the most upstream cyclist not only has an influence on one cyclist, but potentially for the entirety of a sprint train or team time trial train. Furthermore, it can be noted that having a cyclist in Position 3, will also benefit the cyclist in Position 2 due to the upstream drag reduction effect. However, one should still consider that typically in a team time trial, the order of the cyclists in tandem is consistently changing, and hence the overall group drag reduction is also continuously varying.

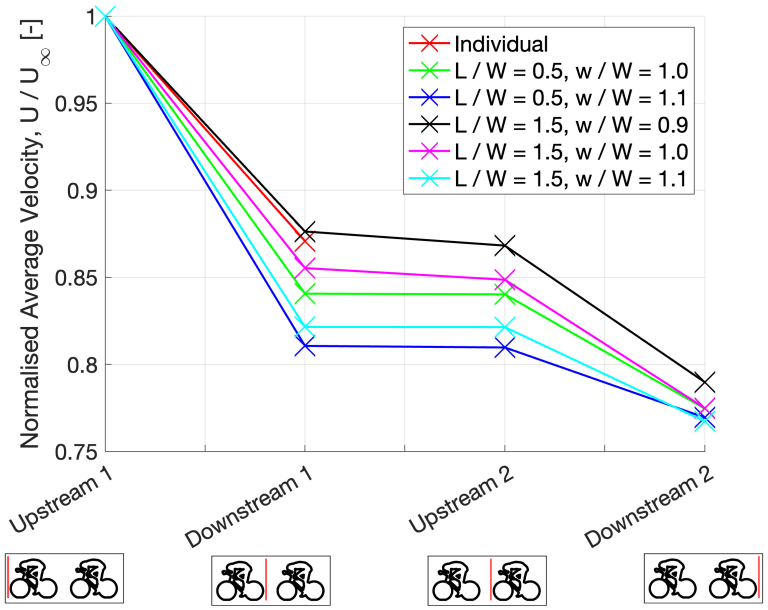

Figure 8.23: The average normalised squared velocity in the YZ-planes at various locations for tandem cyclists

In Figure 8.23, the average of the squared velocity in the YZ-plane immediately upstream and downstream of the cyclist's wheel is plotted for all PIV tested configurations. Observing the values at the "Downstream 1" location, the size and space ratio alters the velocity deficit behind the upstream cyclist, signifying a notable variation in drag force, despite the limited effect on drag reduction. Furthermore, despite freestream re-energising of the wake occurring between the two cyclists, limited variation in velocity deficit occurs between the "Downstream 1" and "Upstream 2" location. As noted earlier with the cylinder case, this is is slightly misleading, as the velocity deficit measurement at the "Upstream 2" location is undervalued due to the trailing cyclist's stagnation point.

The group drag assessment of the average squared velocity is performed at the 'Downstream 2' location. Here, the lowest squared velocity occurs when a large upstream cyclist is placed upstream. This implies the weakest drag force to experienced by a cyclist placed further downstream of the "Downstream 2" location. Additionally, comparing with the $w/W = 1.1$ case, only a 1% increase in average squared velocity (over the entire YZ plane) is observed at 'Downstream 2' when an equally sized cyclist is placed upstream. Meanwhile, for the $w/W = 0.9$, this squared velocity increase is observed to be around 3%. It should be noted, that the squared velocity values shown here incorporated freestream regions and the differences in incoming flow velocity experienced by a cyclist further downstream of the 'Downstream 2' location would be greater. Lastly, this variation in squared velocity implies that a relatively larger drag penalty is endured by cyclists in a drafting train when a smaller sized upstream cyclist is used, due to the relatively higher drag penalties experienced by the immediately downstream

cyclist.

8.4.1. Aerodynamic relationship between cyclists and cylinders

A comprehensive comparison between the flow characteristics and variations in drag reduction for different bluff bodies is now possible, when analysing the observations made for cylinders in Chapter 7 and for cyclists in Chapter 8. It should reminded however, that the comparison of specific drag reduction values between these two bluff bodies are not recommended due to the drag reduction for cyclist being distinctly sensitive to the position and shape of the body. However, both in Table 8.3 and Table 8.4, a generalist view of of the flow features for the tandem body cases is summarised, and how these are affected by changes in either spacing or size ratio configuration is covered.

Table 8.3: Summary of the general downstream effects on the drag reduction for the upstream tandem cylinder and cyclist. The effect the spacing and siding has on the general drag reduction is additionally described

	Drag reduction for upstream model		
	Downstream effect		
Model	**General**	**Increased spacing**	**Increased size ratio**
Upstream cylinder	Positive - moderate	Positive and negative - moderate	Negative - moderate
Upstream cyclist	Positive - weak	Negative - weak	Negative - weak

For the upstream object, both the cylinder and cyclist case receive a drag reduction when a trailing object is placed downstream. However, the effect is far more notable for an upstream cylinder than it is for an upstream cyclist. For the cylinder case, a fluctuation in drag reduction with spacing is observed due to flow regime switching between the two tandem cylinders occurring, which is a phenomena that does not take place for drafting cyclists. Additionally, due to the weaker strength of the downstream stagnation point for the cyclist case, the size ratio is non-significant on the upstream object's drag reduction. It can be noted that the upstream object only experiences a downstream drag reduction effect as the upstream flow conditions are freestream.

Table 8.4: Summary of the general upstream and downstream effects on the drag reduction for the downstream tandem cylinder and cyclist. The effect the spacing and siding has on the general drag reduction is additionally described

	Drag reduction for downstream model					
	Upstream effect			**Downstream effect**		
Model	**General**	**Increased spacing**	**Increased size ratio**	**General**	**Increased spacing**	**Increased size ratio**
Downstream cylinder	Positive - strong	Negative - weak and moderate	Positive - strong	Negative - moderate	Negative - moderate	Positive - moderate
Downstream cyclist	Positive - moderate	Negative - moderate	Positive - moderate	Positive - moderate	Negative - weak	Positive - weak

The downstream object meanwhile, is affected by both an upstream drag reduction effect, from the reduced incoming flow velocity, and a downstream drag reduction effect, from an alteration to the trailing edge wake profile. From the upstream perspective, the downstream cylinder experiences a greater drag reduction than that for cyclist, which still experiences moderate leading edge drag reductions. The effect of spacing on the cylinder drag reduction is also dependent on whether a

flow regime switch occurs or not, where it is weak if a flow regime change is absent and moderate if present. Meanwhile, for the cyclist case, a consistent moderate spacing effect for the leading edge drag reduction is observed. For the size ratio, the cylinder is heavily influenced, and to a lesser extent for the downstream cyclist. Divergences between the cylinder and cyclist cases appear for the downstream drag reduction effects for the trailing object. The downstream cylinder experiences a trailing edge drag increase (negative drag reduction). This cylinder downstream drag reduction effect is moderately effected by both the spacing and size ratio. Meanwhile, the downstream cyclist experiences a positive downstream drag reduction effect when drafting. However, the influence of this effect is less than that for the cylinder case. This is further highlighted with the effect of spacing and size ratio for the trailing cyclist downstream drag reduction being relatively weak.

9

Conclusions and further recommendations

9.1. Conclusions

In this study, an experimental campaign has been undertaken for tandem finite cylinders and cyclists of various spacing and size ratios configurations. The aerodynamic links between the two types of bluff bodies were examined and the possible influences the obtained results can have on drafting in professional cycling has also been considered. The experimental methodology is split into two distinct sections, firstly a force balance campaign in order to obtain accurate drag forces for each model in a tandem configuration. Secondly, a flow visualisation campaign using a Particle Image Velocimetry set up is undertaken to understand and explain the variations in drag forces experienced between the various configurations tested. A multi-planar PIV method with interpolation of velocity data between several XY-planes at differing Z-heights is used to obtain quasi-3D flow around the tandem objects and is found to provide ample accuracy and spatial resolution to capture the dominant flow structures around scaled cylinder and cyclist models. For the tandem cylinder cases, an experimental methodology with a 40% variation in size ratio over a wide range of spacings was conducted. Meanwhile, for the drafting cyclist case, a 20% variation in size ratio was tested for a range of wheel spacings typically observed in competition environments

From the force balance data, a distinct variation in trends for the drag coefficient of the upstream cylinder compared with the downstream cylinder was observed. For the upstream cylinder, in general, a larger spacing between two tandem cylinders or a larger size ratio will reduce the upstream object's drag reduction. This is noted to be due to the downstream object's high pressure stagnation region losing influence on the low pressure region behind the upstream object. The peak drag reduction for the upstream cylinder is observed to be in the magnitude of 18%, while typically ranges between 9% and 16% across the various configurations tested. However, large fluctuations in the upstream cylinder drag reduction are also apparent between the various spacing and size configurations. By means of the

PIV analysis, this is observed to be caused by switches in flow regime occurring on major sections of the truncated cylinder, which vary the incoming velocity for the downstream object, altering the strength of the high pressure stagnation region.

The upstream cyclist observes a similar drag reduction effect to that of the cylinder, whereby the downstream cyclist's stagnation point creates a high pressure region influence on the upstream cyclist's wake. However, the magnitude of the drag reduction for the upstream cyclist case is significantly lower than that for the upstream cylinder, where a maximum drag reduction of only 4.5% is measured. This is suggested to be due to the narrower wake width behind a cyclist and reduced bulbous nature of the cyclist leading edge creating a weaker stagnation point high pressure region which in turn influences the low pressure wake behind the upstream cyclist less. A dissimilarity with the cylinder case is observed whereby no change in flow regime occurs causing no considerable fluctuation in drag reduction across the configurations to be observed. Additionally, the size ratio is found to have a limited effect on the upstream cyclist drag reduction.

Meanwhile, the downstream object's are observed to experience multiple effects which contribute to their drag reduction. For the downstream cylinder, similar to the upstream case, an inverse relationship between spacing and drag reduction is measured, while a positive correlation with the size ratio is observed. Flow visualisation proves this effect to be caused by a closer or larger upstream object, reducing the amount of freestream mixing and velocity of the incoming wake. The leading edge drag reduction effect for the downstream cylinder is therefore found to be significant. However, a notable detrimental downstream effect is also observed which in fact decreases the overall downstream cylinder's drag reduction. It is noticed that the size ratio and spacing slightly changes not only the incoming flow conditions, however also alters the size of the trailing edge low momentum region and explains for the non-uniform variation in downstream drag reductions measured.

The magnitude of the drag reduction for the downstream cyclist is found to be vary to a similar degree with that of the downstream cylinder and a similar trend with spacing a size ratio is measured. Similar to the cylinder case, and alongside observations by Barry et al. 2016a and Mahalingesh 2020, a sizeable leading edge drag reduction effect is observed, where the incoming flow velocity for the downstream cyclist is lower. However, unlike flow around the downstream cylinder or previous observations by literature, a positive drag reduction is also captured on the downstream cyclist's trailing edge, whereby a smaller low momentum region behind the cyclist's bike is observed in the tandem configuration compared with the individual cyclist case. The sizing and spacing is found to have a moderate influence on the upstream effect and limited influence on the downstream effect.

From the experimental campaign, it is found that tandem cylinders and cyclists share many common flow characteristics and drag reduction phenomena, allowing for comparison between the two bluff bodies from a general viewpoint. However, certain considerable differences between the two cases are also observed and as the drag reduction figures for the cyclist case is heavily influenced by the cyclist body shape and position tested, direct comparison of drag reduction figures between cylinder and cyclist tandem configurations is not recommended. However, if cost or complexity of a testing regime is to be minimised, experimental testing of truncated cylinders can still be used to measure and observe certain complex flow interaction between multiple tandem objects at a macroscopic level.

Alongside these observations, a general equation predicting the drag reduction for the upstream, downstream cyclist and overall drafting group for any spacing or size ratio conflagration is produced

from the empirical database captured in this study. Recommendations to the configuration of a team cyclists in a team time trial or sprint train in competitive events have also been suggested from this study. In a team time trial where the drag reduction for the entire group is to be maximised, a larger upstream cyclist is suggested, due to it's inherent ability to decrease the drag forces experienced by multiple downstream cyclists. Furthermore, the measured higher drag force experienced by the larger cyclist should be possible to be compensated by the cyclist's larger power output, to maintain a given velocity. For the sprint train, it is noted that in the final stages of a sprint, the velocity of the lead-out cyclist and sprinter is crucial. It is therefore noted that the drag reduction for the upstream cyclist must be considered an equal priority to that of the downstream cyclist. It is consequently recommended the lead-out cyclist is of a similar size to that of the sprinter.

9.2. Limitations and further research recommendations

It should first be noted that a detailed description of the limitations of the experimental method used in this study is covered in Section 6.3.

Several further limitations are also assosciated with the nature of this study and are discussed. Firstly, and most significantly, from this study, the similarity in drag coefficient between the different models for both the cylinder and cyclist cases, causes the differences in drag reduction to only be attributed to either spacing or size ratio, and not to variations in drag area. As the drag area is likely to vary between different cyclists, particularly when they adopt different positions, and as a constant cycling position was analysed in this study, the results captured cannot be used to conclude the effect of the drag area on drag reduction. Therefore, it is recommended for future research that, similar to the CFD analysis of Defraeye et al. 2014, cyclists models of various positions in tandem is experimentally tested and analysed. Most interestingly, a study of this sort would be able to investigate the potential for a cycling team in a team time trial to use variable body positions as their location in a drafting line varies, to further optimise the group drag reduction.

Furthermore, this potential research can be paired with obtaining a better understanding for the relationship between bluff bodies in tandem. A study could involve tandem cylinders, not only involving a range of size ratios and spacings, but also slight variations in aspect ratios between models. This drag area limitation additionally applies to the cylinder cases, and a recommendation to better understand the effect of the drag area for the drag reduction of truncated cylinders is to remove the zig-zag strips from the cylinder models and repeat the experimental procedure undertaken in this study. This would enable the testing of objects in both the sub-critical and critical Reynolds number regimes, allowing for a diverse ranges of drag areas to be studied.

Another limitation of this study is the usage of only two tandem objects, which increases the difficulty of relating the results collected in this study, with professional cycling events, where more than two cyclists drafting each other are typically observed. Therefore, it is recommended that following studies explore the flow structure interaction between multiple cyclists (of at least four) in tandem and how they vary further downstream for each cyclist.

It has additionally been mentioned that, due to the flow characteristics and drag forces around a cyclist being completely position and shape dependant, this results in the comparison in results from one

study with another to not to be recommended. The recent development of a novel generic cyclist model by both TU Delft and Monash University (Vloemans 2022) has the potential of circumnavigating these issues, whereby various experiments can utilise identical cyclist bodies and minimises the differences between studies. It is therefore recommended for future research that utilisation of the generic cyclist model is conducted.

This study solely collected velocity readings from the PIV flow visualisation data and no pressure determination was performed. This was due to, in the presence of 3D flow cases, two component velocity data being inadequate in solving the Poisson equation to obtain pressure readings, as noted by Oudheusden 2013 and Mahalingesh 2020. Therefore, remarks on variations in drag forces had to be derived from differences in momentum in the incoming flow and wake regions, which does not fully correlate with drag forces. Therefore, it is suggested that future research additionally investigate variations in pressure values for drafting cyclists and cylinders, such that flow characteristics can be attributed to differences in drag forces with more certainty.

References

Adrian, R.J. and J. Westerweel (2010). *Particle image velocimetry*. Cambridge University Press.

Alam, Md Mahbub and Y Zhou (2007). 'Dependence of Strouhal Number, Drag and Lift on the Ratio of Cylinder Diameters in a Two-Tandem Cylinder Wake'. In.

Alam, Md Mahbub and Y. Zhou (May 2008). 'Strouhal numbers, forces and flow structures around two tandem cylinders of different diameters'. In: *Journal of Fluids and Structures* 24 (4), pp. 505–526. ISSN: 08899746. DOI: 10.1016/j.jfluidstructs.2007.10.001.

Alam, Md.Mahbub, M Moriya, K Takai and H Sakamoto (2003a). 'Fluctuating fluid forces acting on two circular cylinders in a tandem arrangement at a subcritical Reynolds number'. In: *Journal of Wind Engineering and Industrial Aerodynamics* 91.1. Fifth Asia-Pacific Conference on Wind Engineering, pp. 139–154. ISSN: 0167-6105. DOI: https://doi.org/10.1016/S0167-6105(02)00341-0. URL: https://www.sciencedirect.com/science/article/pii/S0167610502003410.

Alam, Md.Mahbub, H Sakamoto and M Moriya (2003b). 'Reduction of fluid forces acting on a single circular cylinder and two circular cylinders by using tripping rods'. In: *Journal of Fluids and Structures* 18.3. Bluff-body/Flow interactions, pp. 347–366. ISSN: 0889-9746. DOI: https://doi.org/10.1016/j.jfluidstructs.2003.07.011. URL: https://www.sciencedirect.com/science/article/pii/S0889974603001087.

Allen, Julian H. and Walter G. Vincenti (Dec. 1944). *Wall interference in a two-dimensional-flow wind tunnel, with consideration of the effect of compressibility*. National Advisory Committee for Aeronautics.

Anthoine, Jerome, Domenico Olivari and D. Portugaels (Nov. 2009). 'Wind-tunnel blockage effect on drag coefficient of circular cylinders'. In: *Wind and Structures* 12. DOI: 10.12989/was.2009.12.6.541.

Barlow, Jewel B., William H. Rae and Alan Pope (1999). *Low-Speed Wind Tunnel Testing*. 3rd ed. John Wiley and Sons, Inc.

Barry, Nathan, David Burton, John Sheridan, Mark Thompson and Nicholas Brown (Nov. 2016a). 'Flow field interactions between two tandem cyclists'. In: *Experiments in Fluids* 57. DOI: 10.1007/s00348-016-2273-y.

Barry, Nathan, David Burton, John Sheridan, Mark Thompson and Nicholas A.T. Brown (June 2015). 'Aerodynamic drag interactions between cyclists in a team pursuit'. In: *Sports Engineering* 18 (2), pp. 93–103. ISSN: 14602687. DOI: 10.1007/s12283-015-0172-8.

— (2016b). 'An Analysis of the Wake of Pedalling Cyclists in a Tandem Formation'. In: *Procedia Engineering* 147, pp. 7–12. DOI: 10.1016/j.proeng.2016.06.181. URL: https://doi.org/10.1016/j.proeng.2016.06.181.

Barry, Nathan, John Sheridan, David Burton and Nicholas Brown (Dec. 2014). 'The Effect of Spatial Position on the Aerodynamic Interactions between Cyclists'. In: *Procedia Engineering* 72, pp. 774 –779. DOI: 10.1016/j.proeng.2014.06.131.

Blocken, Bert, Thijs Defraeye, Erwin Koninckx, Jan Carmeliet and Peter Hespel (Jan. 2013). 'CFD simulations of the aerodynamic drag of two drafting cyclists'. In: *Computers and Fluids* 71, pp. 435–445. ISSN: 00457930. DOI: 10.1016/j.compfluid.2012.11.012.

Blocken, Bert, Yasin Toparlar, Thijs van Druenen and Thomas Andrianne (Nov. 2018). 'Aerodynamic drag in cycling team time trials'. In: *Journal of Wind Engineering and Industrial Aerodynamics* 182, pp. 128–145. ISSN: 01676105. DOI: 10.1016/j.jweia.2018.09.015.

Broker, JEFFREY P., CHESTER R. Kyle and EDMUND R. Burke (Nov. 1999). 'Racing cyclist power requirements in the 4000-m individual and team pursuits'. In: *Medicine and Science in Sports and Exercise* 31 (11), p. 1677. ISSN: 0195-9131. DOI: 10.1097/00005768-199911000-00026.

Cramp, Anthony (2010). *The Sky Train*. URL: https://www.flickr.com/photos/7770166@N05/4306538000.

Crouch, Timothy (Sept. 2013). 'Flow Topology and Large-Scale Wake Structures Around Elite Cyclists'. Monash University. DOI: 10.4225/03/58ae201dda731.

Crouch, Timothy N., David Burton, Zach A. LaBry and Kim B. Blair (May 2017). 'Riding against the wind: a review of competition cycling aerodynamics'. In: *Sports Engineering* 20.2, pp. 81–110. DOI: 10.1007/s12283-017-0234-1. URL: https://doi.org/10.1007/s12283-017-0234-1.

Crouch, T.N., D. Burton, N.A.T. Brown, M.C. Thompson and J. Sheridan (2014). 'Flow topology in the wake of a cyclist and its effect on aerodynamic drag'. In: *Journal of Fluid Mechanics* 748, pp. 5–35. ISSN: 14697645. DOI: 10.1017/jfm.2013.678.

Davies, C. T. M. and E. R. Sandstrom (July 1989). 'Maximal mechanical power output and capacity of cyclists and young adults'. In: *European Journal of Applied Physiology and Occupational Physiology* 58.8, pp. 838–844. DOI: 10.1007/bf02332216. URL: https://doi.org/10.1007/bf02332216.

Defraeye, Thijs, Bert Blocken, Erwin Koninckx, Peter Hespel and Jan Carmeliet (2010). 'Aerodynamic study of different cyclist positions: CFD analysis and full-scale wind-tunnel tests'. In: *Journal of Biomechanics* 43.7, pp. 1262–1268. ISSN: 0021-9290. DOI: https://doi.org/10.1016/j.jbiomech.2010.01.025. URL: https://www.sciencedirect.com/science/article/pii/S002192901000059X.

Defraeye, Thijs, Bert Blocken, Erwin Koninckx, Peter Hespel, Pieter Verboven, Bart Nicolai and Jan Carmeliet (Jan. 2014). 'Cyclist Drag in Team Pursuit: Influence of Cyclist Sequence, Stature, and Arm Spacing'. In: *Journal of Biomechanical Engineering* 136 (1). ISSN: 0148-0731. DOI: 10.1115/1.4025792.

Edwards, Andy G. and William C. Byrnes (Jan. 2007). 'Aerodynamic characteristics as determinants of the drafting effect in cycling'. In: *Medicine and Science in Sports and Exercise* 39 (1), pp. 170–176. ISSN: 01959131. DOI: 10.1249/01.mss.0000239400.85955.12.

Essel, Ebenezer E., Mark F. Tachie and Ram Balachandar (2021). 'Time-resolved wake dynamics of finite wall-mounted circular cylinders submerged in a turbulent boundary layer'. In: *Journal of Fluid Mechanics* 917, A8. DOI: 10.1017/jfm.2021.265.

Glauert, H. (Sept. 1933). *Wind Tunnel Interference on Wings, Bodies and Airscrews*. Aeronautical Research Committee.

Hain, Rainer, Christian J. Kähler and Dirk Michaelis (Oct. 2008). 'Tomographic and time resolved PIV measurements on a finite cylinder mounted on a flat plate'. In: *Experiments in Fluids* 45 (4), pp. 715–724. ISSN: 0723-4864. DOI: 10.1007/s00348-008-0553-x.

Igarashi, Tamotsu (1981). 'Characteristics of the Flow around Two Circular Cylinders Arranged in Tandem : 1st Report'. In: *Bulletin of JSME* 24 (188), pp. 323–331. ISSN: 0021-3764. DOI: 10.1299/jsme1958.24.323.

Igarashi, Tamotsu (1982). 'Characteristics of a Flow around Two Circular Cylinders of Different Diameters Arranged in Tandem'. In: *Bulletin of JSME* 25 (201), pp. 349–357. ISSN: 0021-3764. DOI: 10.1299/jsme1958.25.349.

Igbalajobi, A., J.F. McClean, D. Sumner and D.J. Bergstrom (2013). 'The effect of a wake-mounted splitter plate on the flow around a surface-mounted finite-height circular cylinder'. In: *Journal of Fluids and*

Structures 37, pp. 185–200. ISSN: 0889-9746. DOI: https://doi.org/10.1016/j.jfluidstructs.2012.10.001. URL: https://www.sciencedirect.com/science/article/pii/S0889974612001946.

Jeon, Wan-Soo (Aug. 1996). 'Experimental Study of Flow Fields around Cylinder Arrays Using PIV'. In: *Journal of Ocean Engineering and Technology* 3.3.

Jux, Constantin (2022). 'Development of robotic volumetric PIV with applications in sports aerodynamics'. Delft University of Technology. DOI: 10.4233/uuid:643a6936-ce92-4c3e-af0f-5c251a50abbe. URL: https://doi.org/10.4233/uuid:643a6936-ce92-4c3e-af0f-5c251a50abbe.

Kawamura, T. M. (Nov. 1953). *Wind Drag of Bicycles*. Tokyo University.

Keane, R D and R J Adrian (Nov. 1990). 'Optimization of particle image velocimeters. I. Double pulsed systems'. In: *Measurement Science and Technology* 1.11, pp. 1202–1215. DOI: 10.1088/0957-0233/1/11/013. URL: https://doi.org/10.1088/0957-0233/1/11/013.

Kim, T. and K. T. Christensen (Apr. 2018). 'Flow Interactions Between Streamwise-Aligned Tandem Cylinders in Turbulent Channel Flow'. In: *AIAA Journal* 56 (4), pp. 1421–1433. ISSN: 0001-1452. DOI: 10.2514/1.J056186.

Kyle, C. R. and E Burke (1984). 'Improving the racing bicycle'. In: *Mechanical engineering* 9 (106), pp. 34–35.

Kyle, Chester R. (1979). 'Reduction of wind resistance and power output of racing cyclists and runners travelling in groups'. In: *Ergonomics* 22 (4), pp. 387–397. ISSN: 13665847. DOI: 10.1080/00140137908924623.

LaVision, GmbH (Aug. 2020). *Imager sCMOS CLHS*.

Ljungkrona, L., Ch. Norberg and B. Sundén (Nov. 1991). 'Free-stream turbulence and tube spacing effects on surface pressure fluctuations for two tubes in an in-line arrangement'. In: *Journal of Fluids and Structures* 5 (6), pp. 701–727. ISSN: 08899746. DOI: 10.1016/0889-9746(91)90364-U. URL: https://linkinghub.elsevier.com/retrieve/pii/088997469190364U.

Luo, S.C., T.L. Gan and Y.T. Chew (Jan. 1996). 'Uniform flow past one (or two in tandem) finite length circular cylinder(s)'. In: *Journal of Wind Engineering and Industrial Aerodynamics* 59 (1), pp. 69–93. ISSN: 01676105. DOI: 10.1016/0167-6105(95)00036-4.

Mahalingesh, Nikhil (Feb. 2020). 'On-Site Drafting Aerodynamics of Cyclists using the Ring of Fire'. Delft University of Technology. URL: http://repository.tudelft.nl/..

Malizia, Fabio, T. van Druenen and B. Blocken (Dec. 2021). 'Impact of wheel rotation on the aerodynamic drag of a time trial cyclist'. In: *Sports Engineering* 24 (1). ISSN: 14602687. DOI: 10.1007/s12283-021-00341-6.

Maskell, E. C. (Nov. 1963). *A Theory of the Blockage Effects on Bluff Bodies and Stalled Wings in a Closed Wind Tunnel*. Aeronautical Research Committee.

Modi, V.J. and S.E. El-Sherbiny (1973). 'On the wall confinement effects in the industrial aero- dynamics studies'. In: p. 116.

Nobach, Holger and Eberhard Bodenschatz (Feb. 2009). 'Limitations of accuracy in PIV due to individual variations of particle image intensities'. In: *Experiments in Fluids* 47.1, pp. 27–38. DOI: 10.1007/s00348-009-0627-4. URL: https://doi.org/10.1007/s00348-009-0627-4.

Novák, Josef (1975). 'Strouhal Number of two cylinders of different diameter arranged in tandem'. In: *Acta Technica ČSAV* 3, pp. 366–374.

Nørstrud, Helge, Giuseppe Gibertini and Donato Grassi (2008). 'Cycling aerodynamics'. In: *Sport aerodynamics*. Vol. 506. Springer, 23–47.

Okamoto, Tetsushi and Miki Yagita (1973). 'The Experimental Investigation on the Flow Past a Circular Cylinder of Finite Length Placed Normal to the Plane Surface in a Uniform Stream'. In: *Bulletin of JSME* 16.95, pp. 805–814. DOI: 10.1299/jsme1958.16.805.

Oudheusden, B W van (Mar. 2013). 'PIV-based pressure measurement'. In: *Measurement Science and Technology* 24 (3), p. 032001. ISSN: 0957-0233. DOI: 10.1088/0957-0233/24/3/032001.

Padilla, Sabino, Iñigo Mujika, Francisco Angulo and Juan Jose Goiriena (Oct. 2000). 'Scientific approach to the 1-h cycling world record: a case study'. In: *Journal of Applied Physiology* 89.4, pp. 1522–1527. DOI: 10.1152/jappl.2000.89.4.1522. URL: https://doi.org/10.1152/jappl.2000.89.4.1522.

Pattenden, R. J., S. R. Turnock and X. Zhang (July 2005). 'Measurements of the flow over a low-aspect-ratio cylinder mounted on a ground plane'. In: *Experiments in Fluids* 39 (1), pp. 10–21. ISSN: 0723-4864. DOI: 10.1007/s00348-005-0949-9.

Prasad, A. K. (Aug. 2000). 'Stereoscopic particle image velocimetry'. In: *Experiments in Fluids* 29.2, pp. 103–116. DOI: 10.1007/s003480000143. URL: https://doi.org/10.1007/s003480000143.

Raffel, Markus, Christian E. Willert, Fulvio Scarano, Christian J. Kähler, Steve T. Wereley and Jürgen Kompenhans (2018). *Particle Image Velocimetry*. Springer International Publishing. ISBN: 978-3-319-68851-0. DOI: 10.1007/978-3-319-68852-7.

Roshko, A. (1993). 'Perspectives on bluff body aerodynamics'. In: *Journal of Wind Engineering and Industrial Aerodynamics* 49.1, pp. 79–100. ISSN: 0167-6105. DOI: https://doi.org/10.1016/0167-6105(93)90007-B. URL: https://www.sciencedirect.com/science/article/pii/016761059390007B.

Schewe, Günter (Dec. 2001). 'Reynolds-number effects in flow around more-or-less bluff bodies'. In: vol. 89. DOI: 10.1016/S0167-6105(01)00158-1.

Schewe, Günter and Markus Jacobs (2019). 'Experiments on the Flow around two tandem circular cylinders from sub- up to transcritical Reynolds numbers'. In: *Journal of Fluids and Structures* 88, pp. 148–166. ISSN: 0889-9746. DOI: https://doi.org/10.1016/j.jfluidstructs.2019.05.001. URL: https://www.sciencedirect.com/science/article/pii/S0889974618308818.

Schneiders, Jan F. G., Giuseppe C. A. Caridi, Andrea Sciacchitano and Fulvio Scarano (Oct. 2016). 'Large-scale volumetric pressure from tomographic PTV with HFSB tracers'. In: *Experiments in Fluids* 57.11, p. 164. ISSN: 1432-1114. DOI: 10.1007/s00348-016-2258-x. URL: https://doi.org/10.1007/s00348-016-2258-x.

Sciacchitano, A. and F. Scarano (Apr. 2022). *Flow Measurement Techniques: Student Manual for the Laboratory Exercise*. Delft University of Technology.

Shah, Yash Hemant (2017). *Drag analysis of full scale cyclist model using large-scale 4D-PTV An accuracy assessment*. URL: http://repository.tudelft.nl/..

Shao, Nan, Guobin Xu, Fang Liu, Xiang Yan, Xiaoqun Wang, Heng Deng and Zheng Zheng (Feb. 2020). 'Experimental study on the flow-induced motion and hydrokinetic energy of two t-section prisms in tandem arrangement'. In: *Applied Sciences* 10 (3). ISSN: 20763417. DOI: 10.3390/app10031136.

Shirasaki, Keita, Kaoru Yamanobe, Keita Akashi and Wataru Takashima (Nov. 2017). 'Variation of the drafting effect on the trailing rider for different numbers of riders in a cycling group'. In: *Proceedings of the Institution of Mechanical Engineers, Part P: Journal of Sports Engineering and Technology*, p. 175433711773661. ISSN: 1754-3371. DOI: 10.1177/1754337117736617.

— (Dec. 2019). 'Aerodynamic variation with differences in the number of riders in a cycling group'. In: *Taiikugaku kenkyu (Japan Journal of Physical Education, Health and Sport Sciences)* 64. DOI: 10.5432/jjpehss.18086.

Spoelstra, A., A. Sciacchitano, F. Scarano and N. Mahalingesh (Dec. 2021). 'On-site drag analysis of drafting cyclists'. In: *Journal of Wind Engineering and Industrial Aerodynamics* 219. ISSN: 01676105. DOI: 10.1016/j.jweia.2021.104797.

Sumner, D. (Aug. 2010). 'Two circular cylinders in cross-flow: A review'. In: *Journal of Fluids and Structures* 26 (6), pp. 849–899. ISSN: 08899746. DOI: 10.1016/j.jfluidstructs.2010.07.001.

Sumner, D., J. L. Heseltine and O. J. P. Dansereau (Nov. 2004). 'Wake structure of a finite circular cylinder of small aspect ratio'. In: *Experiments in Fluids* 37 (5), pp. 720–730. ISSN: 0723-4864. DOI: 10.1007/s00348-004-0862-7.

Sumner, D. and H.K. Reitenbach (Aug. 2019). 'Wake interference effects for two finite cylinders: A brief review and some new measurements'. In: *Journal of Fluids and Structures* 89, pp. 25–38. ISSN: 08899746. DOI: 10.1016/j.jfluidstructs.2019.02.004.

Terra, W., A. Sciacchitano and F. Scarano (July 2017). 'Aerodynamic drag of a transiting sphere by large-scale tomographic-PIV'. In: *Experiments in Fluids* 58 (7), p. 83. ISSN: 0723-4864. DOI: 10.1007/s00348-017-2331-0.

— (May 2020). 'Cyclist Reynolds number effects and drag crisis distribution'. In: *Journal of Wind Engineering and Industrial Aerodynamics* 200, p. 104143. DOI: 10.1016/j.jweia.2020.104143. URL: https://doi.org/10.1016/j.jweia.2020.104143.

Terra, W., A. Sciacchitano and Y. H. Shah (Jan. 2019). 'Aerodynamic drag determination of a full-scale cyclist mannequin from large-scale PTV measurements'. In: *Experiments in Fluids* 60.2, p. 29. ISSN: 1432-1114. DOI: 10.1007/s00348-019-2677-6. URL: https://doi.org/10.1007/s00348-019-2677-6.

Terra, Wouter, Andrea Sciacchitano and Fulvio Scarano (2016). 'Evaluation of aerodynamic drag of a full-scale cyclist model by large-scale tomographic PIV'. In: *International Workshop on Non-Intrusive Optical Flow Diagnostic*.

Timmer, Nando and Leo Veldhuis (Feb. 2021). 'The impact of skinsuit zigzag tape turbulators on speed skating performance'. In: *Applied Sciences (Switzerland)* 11 (3), pp. 1–18. ISSN: 20763417. DOI: 10.3390/app11030988.

Torre, A Íñiguez-de-la and J Íñiguez (Oct. 2009). 'Aerodynamics of a cycling team in a time trial: does the cyclist at the front benefit?' In: *European Journal of Physics* 30.6, p. 1365. DOI: 10.1088/0143-0807/30/6/014. URL: https://dx.doi.org/10.1088/0143-0807/30/6/014.

TU-Delft (n.d.). URL: https://www.tudelft.nl/lr/organisatie/afdelingen/flow-physics-and-technology/facilities/low-speed-wind-tunnels/w-tunnel.

Underwood, L., J. Schumacher, J. Burette-Pommay and M. Jermy (Nov. 2011). 'Aerodynamic drag and biomechanical power of a track cyclist as a function of shoulder and torso angles'. In: *Sports Engineering* 14.2-4, pp. 147–154. DOI: 10.1007/s12283-011-0078-z. URL: https://doi.org/10.1007/s12283-011-0078-z.

Vereecken, Nico (2023). *Paris-Nice 2023 stage 3 TTT*. Cor Vos Fotopersburo-Video. URL: https://www.corvospro.com/preview.aspx?VIEW_OFFSET=14&CATEG=15019000.

Vloemans, Siward (2022). *Cyclist Mannequin For Aerodynamics Research: Develop a cyclist mannequin from 3D scans for aerodynamics tests*. URL: http://repository.tudelft.nl/..

Wang, J. J., P. F. Zhang, S. F. Lu and K. Wu (Jan. 2006). 'Drag reduction of a circular cylinder using an upstream rod'. In: *Flow, Turbulence and Combustion* 76 (1), pp. 83–101. ISSN: 13866184. DOI: 10.1007/s10494-005-9008-0.

Wang, Longjun, M. Mahbub Alam and Yu Zhou (Feb. 2018). 'Two tandem cylinders of different diameters in cross-flow: Effect of an upstream cylinder on wake dynamics'. In: *Journal of Fluid Mechanics* 836, pp. 5–42. ISSN: 14697645. DOI: 10.1017/jfm.2017.735.

West, G.S. and C.J. Apelt (1993). 'Measurements of Fluctuating Pressures and Forces on a Circular Cylinder in the Reynolds Number Range 104 to 2·5 × 105'. In: *Journal of Fluids and Structures* 7.3, pp. 227–244. ISSN: 0889-9746. DOI: https://doi.org/10.1006/jfls.1993.1014. URL: https://www.sciencedirect.com/science/article/pii/S0889974683710145.

Westerweel, Jerry and Fulvio Scarano (Dec. 2005). 'Universal outlier detection for PIV data'. In: *Experiments in Fluids* 39 (6), pp. 1096–1100. ISSN: 0723-4864. DOI: 10.1007/s00348-005-0016-6.

Wieselsberger, C. (1921). 'Neuere Festellungen üeber die Gesetze des Flussigkeits- und Luftwiderstands'. In: *Physikalische Zeitschrift* 22, pp. 321–328.

Willert, C. E. and M. Gharib (Jan. 1991). 'Digital particle image velocimetry'. In: *Experiments in Fluids* 10.4, pp. 181–193. DOI: 10.1007/bf00190388. URL: https://doi.org/10.1007/bf00190388.

Zdravkovich, M. M. (Dec. 1977). 'REVIEW—Review of Flow Interference Between Two Circular Cylinders in Various Arrangements'. In: *Journal of Fluids Engineering* 99 (4), pp. 618–633. ISSN: 0098-2202. DOI: 10.1115/1.3448871. URL: https://asmedigitalcollection.asme.org/fluidsengineering/article/99/4/618/413061/REVIEW-Review-of-Flow-Interference-Between-Two.

Zdravkovich, M. M., M. W. Ashcroft, S.J. Chishohn and N. Hicks (July 1996). 'Effect of cyclist's posture and vicinity of another cyclist on aerodynamic drag'. In: *The Engineering of Sport*, pp. 21–28. DOI: 10.1201/9781003078098-4.

Zhou, Y. and M. W. Yiu (Feb. 2006). 'Flow structure, momentum and heat transport in a two-tandem-cylinder wake'. In: *Journal of Fluid Mechanics* 548 (-1), p. 17. ISSN: 0022-1120. DOI: 10.1017/S002211200500738X.

Zhou, Yu and Md Mahbub Alam (Dec. 2016). 'Wake of two interacting circular cylinders: A review'. In: *International Journal of Heat and Fluid Flow* 62, pp. 510–537. ISSN: 0142727X. DOI: 10.1016/j.ijheatfluidflow.2016.08.008.

A

Cylinders: Additional figures

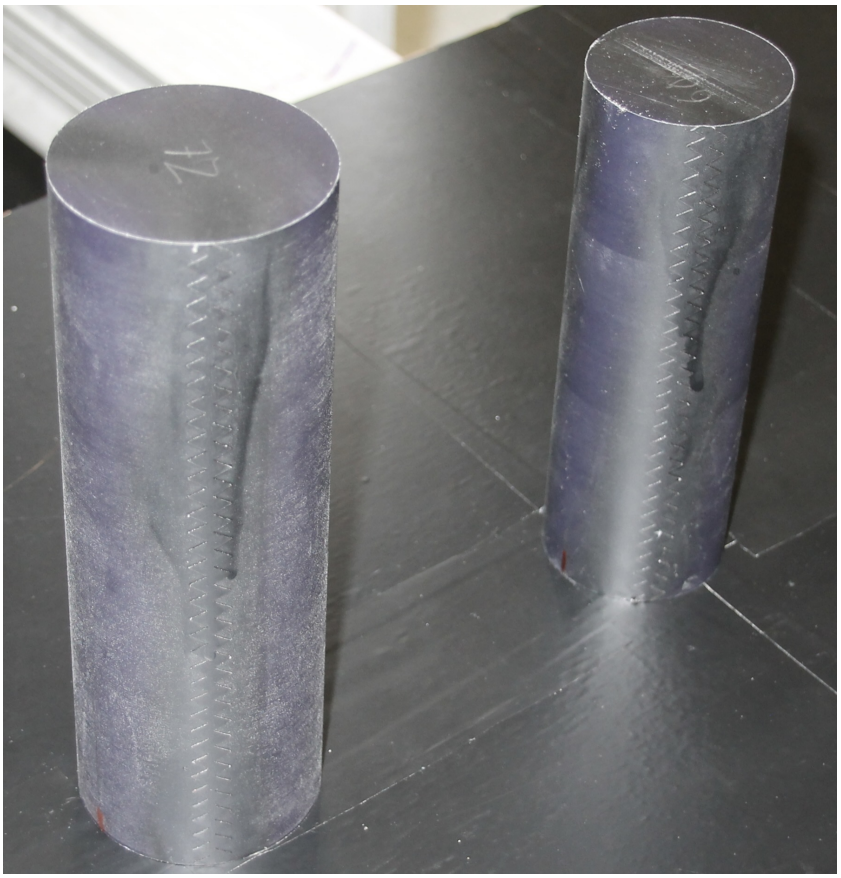

Figure A.1: Zig-zag strips placed on the truncated cylinder models at the left and right leading edge $\theta = 60°$ point. In this figure, the left side strip is visible and coated with black mask paint for the PIV experiment campaign

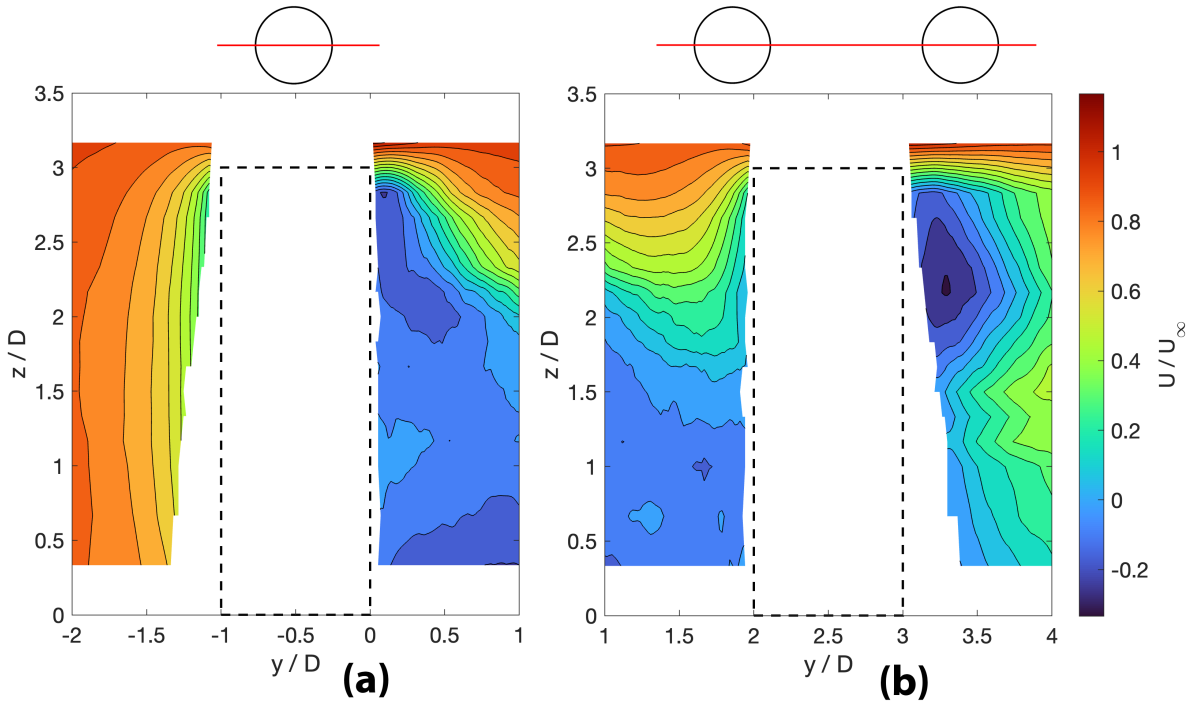

Figure A.2: Velocity contour plots of the streamwise velocity in the XZ mid-plane for the (a) Individual cylinder and (b) Downstream cylinder in the $L/D = 3, d/D = 1$ configuration

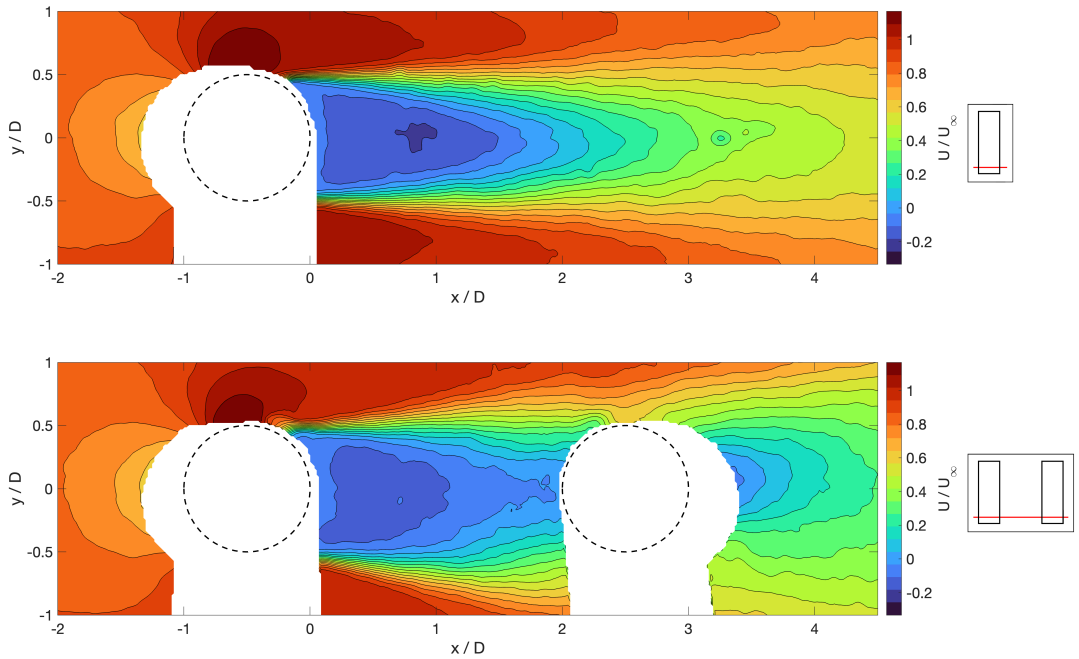

Figure A.3: Velocity contour plots of the streamwise velocity in the XY plane at Z-height $z/H = 0.11$ for the (a) Individual cylinder and (b) $L/D = 3, d/D = 1$ configuration

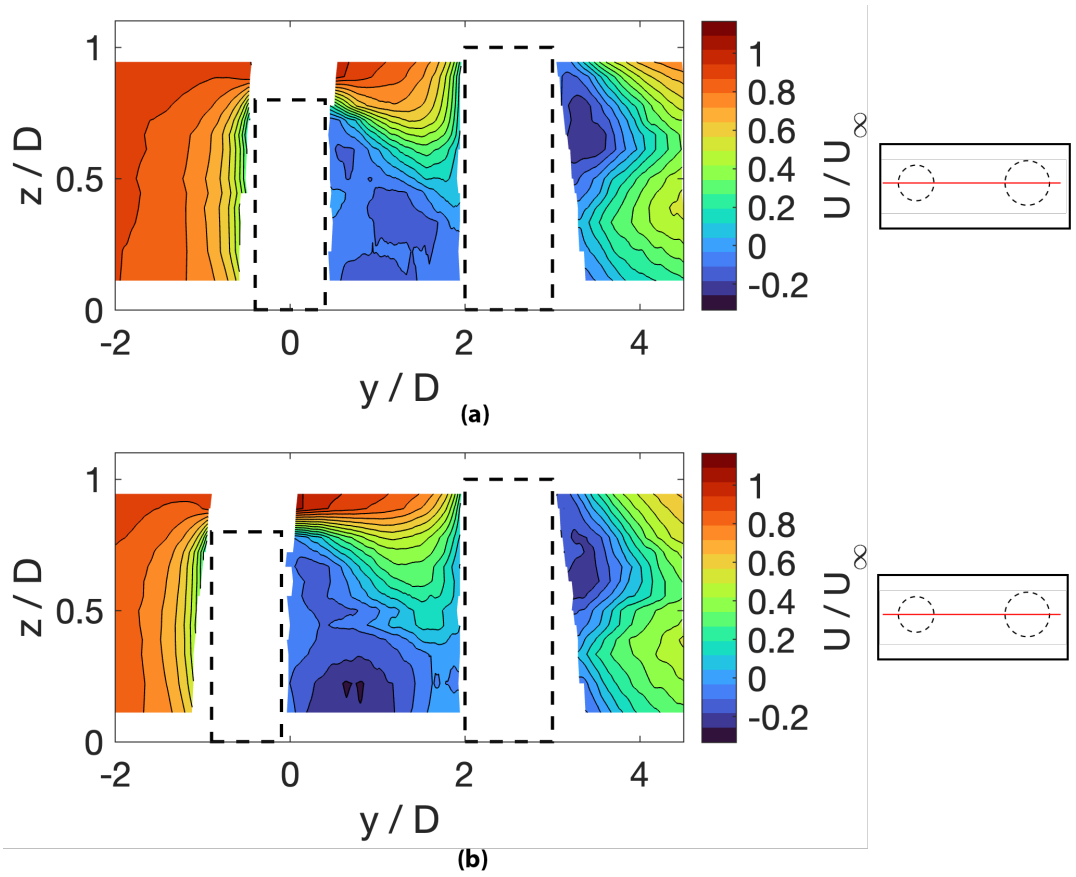

Figure A.4: Velocity contour plots of the streamwise velocity in the XZ mid-plane for the (a) $L/D = 2.5, d/D = 0.8$ and (b) $L/D = 3, d/D = 0.8$ configuration

B

Cyclists: Additional figures

Figure B.1: Surface finish of the 3D printed cyclist model. In this figure, the models have been coated in black mask paint for the PIV campaign

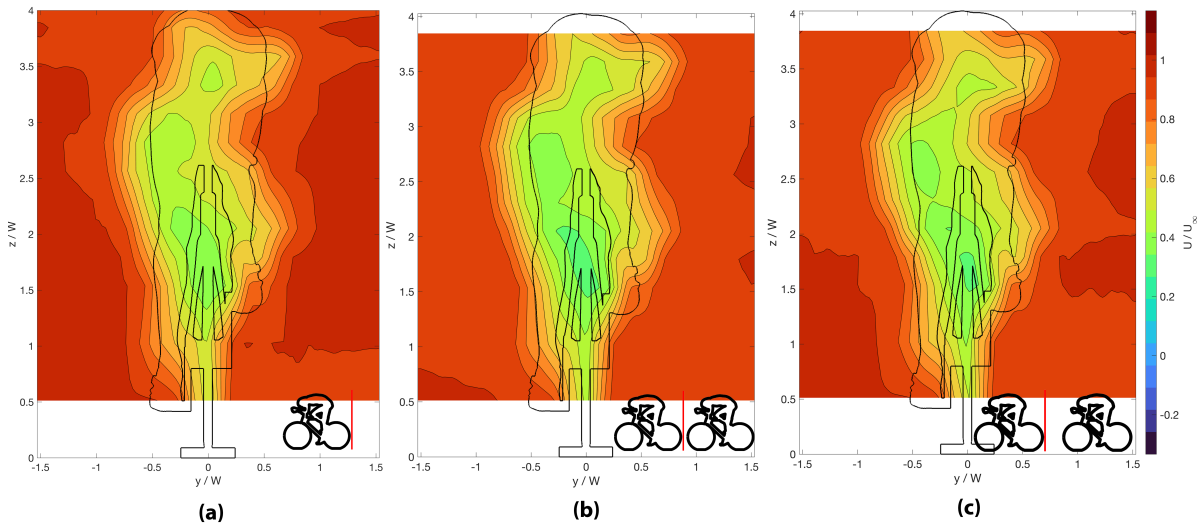

Figure B.2: Streamwise velocity contour plots in the YZ-plane, (a) Immediately downstream of an individual cyclist's rear wheel, (b) Immediately downstream of an upstream tandem cyclist's rear wheel for the $L/W = 0.5, w/W = 1.0$ configuration and (c) Immediately downstream of an upstream tandem cyclist's rear wheel for the $L/W = 1.5, w/W = 1.0$ configuration

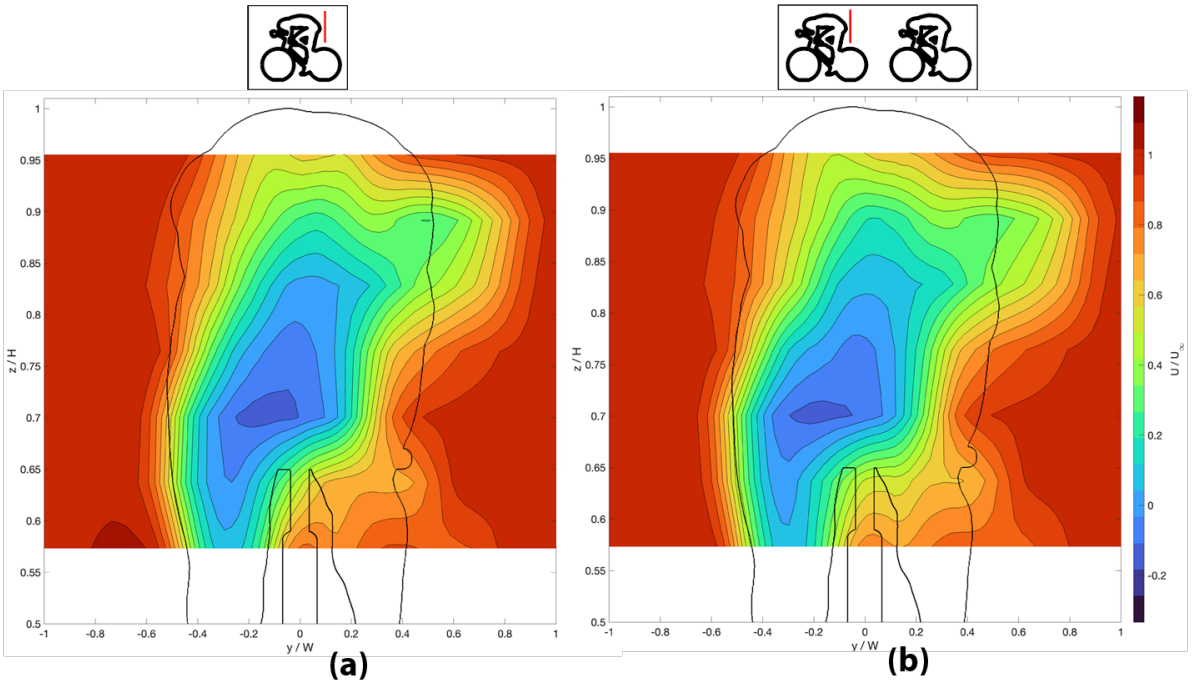

Figure B.3: Streamwise velocity contour plots in the YZ-plane, (a) Behind an individual cyclist's body, (b) Behind an upstream tandem cyclist's body for the $L/W = 1.5, w/W = 1.0$ configuration

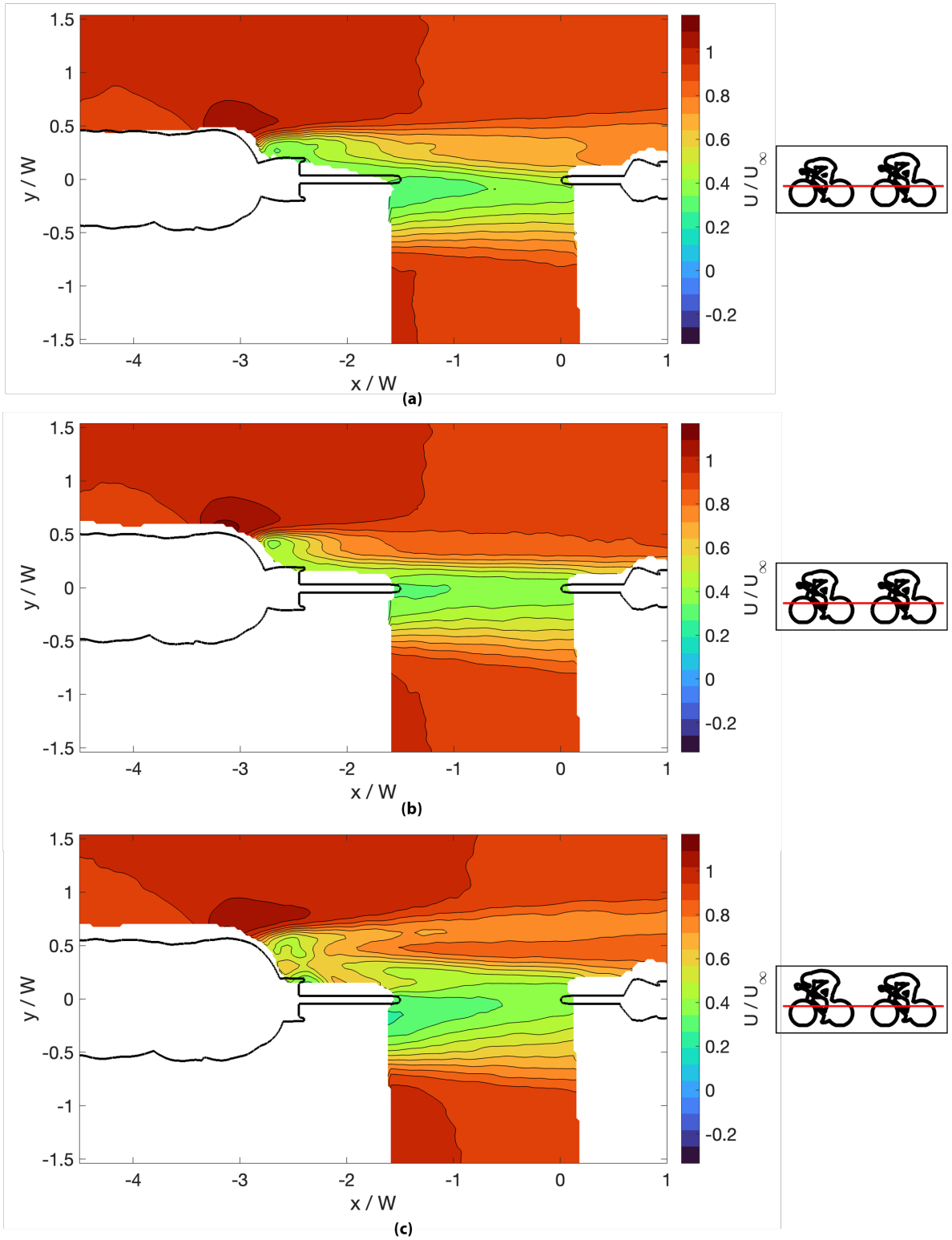

Figure B.4: Streamwise velocity contour plots in the XY-plane at Z-height $z/H = 0.45$ for the (a) Individual cyclist (b) $L/W = 1.5, w/W = 1.0$ and (c) $L/W = 1.5, w/W = 1.1$ configuration

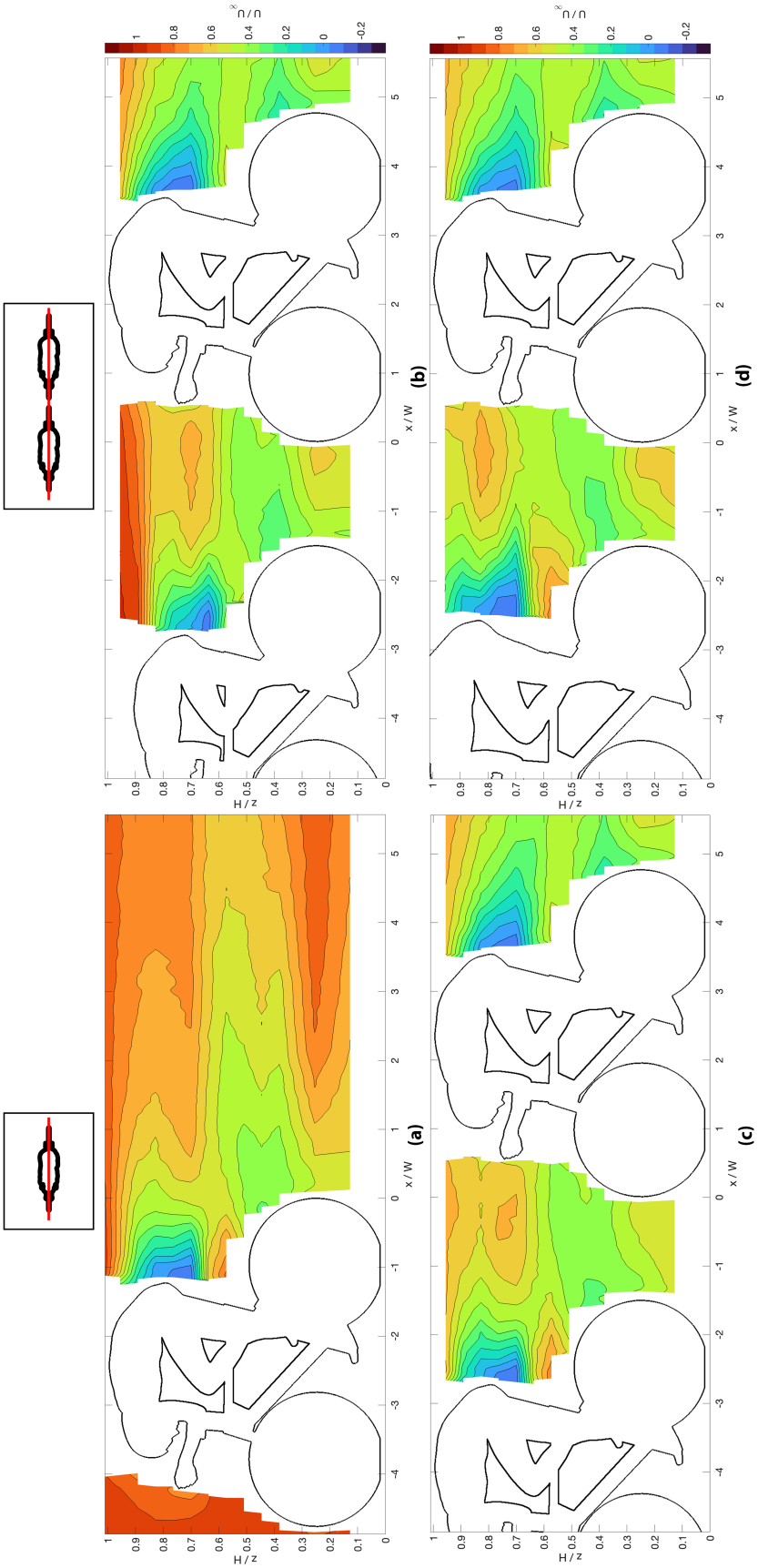

Figure B.5: Streamwise velocity contour plots in the XZ-plane in Y-axis centreline for the (a) Individual cyclist (b) $L/W = 1.5, w/W = 0.9$, (c) $L/W = 1.5, w/W = 1.0$ and (d) $L/W = 1.5, w/W = 1.1$ configuration